Electrospun Carbon Nanofibers for Electrochemical Capacitor Electrodes

A Dissertation
Presented to
The Academic Faculty

by

Tong Wang

In Partial Fulfillment
of the Requirements for the Degree
Doctor of Philosophy in the
School of Polymer, Textile and Fiber Engineering

Georgia Institute of Technology

May 2007

Electrospun Carbon Nanofibers for Electrochemical Capacitor Electrodes

Approved by:

Dr. Satish Kumar, Advisor
School of Polymer, Textile and Fiber Engineering
Georgia Institute of Technology

Dr. Ravi Bellamkonda
Department of Biomedical Engineering
Georgia Institute of Technology

Dr. Anselm Griffin
School of Polymer, Textile and Fiber Engineering
Georgia Institute of Technology

Dr. John D. Muzzy
School of Chemical and Biomolecular Engineering
Georgia Institute of Technology

Dr. Rina Tannenbaum
School of Materials Science and Engineering
Georgia Institute of Technology

Date Approved: 12/05/2006

ACKNOWLEDGEMENTS

I would like to express my gratitude to all those who gave me the possibility to complete this thesis. To begin, I would like to thank deeply my thesis advisor Dr. Satish Kumar, whose guidance, insightful suggestions, and encouragement helped me during my five years' research work at Georgia Tech.

I wish to thank Professors Ravi Bellamkonda, Anselm Griffin, John D. Muzzy, and Rina Tannenbaum for serving on my thesis committee. Also, I would like to express my appreciation to Drs. Tao Liu, Hongming Ma, Xiefei Zhang, and Chongfu Zhou for helpful discussion during their stay at Georgia Tech. Thanks to Drs. Wallace W. Carr and Hongming Dong for help with high speed photography, to Dr. Tetsuya Uchida for high resolution transmission electron microscopy, to Dr. Rosario Gerhardt for assistant with impedance analysis. I am grateful to Huina Guo and Marilyn Lillith Minus for assistance with wide angle X-ray diffraction study. I also appreciate the help of Jing Liu, Sudhakar Jagannathan, and other group members during the course of this study.

Finally, I would like to express my appreciation to my husband and my family for their long-standing support and patience in the completion of this work.

TABLE OF CONTENTS

LIST OF TABLES

LIST OF FIGURES

SUMMARY

The objective of this work is to electrospin poly(acrylonitrile) (PAN) based nanofibers with controlled diameter and to stabilize and carbonize them for developing meso-porous carbon for application as electrochemical capacitor electrodes. A sacrificial polymer, poly(styrene-co-acrylonitrile) (SAN) has been used to control porosity. Carbon nanotubes (CNT) have been used to increase electrode conductivity and hence power density. The study has been divided into two parts.

In part I, electrospinning behavior of PAN and PAN/CNT has been studied. The diameter of electrospun PAN fibers was monitored as a function of polymer molecular weight, solution concentration, solution flow rate, distance between the spinneret and the target, and the applied voltage. Bead free PAN fibers of 60 nm diameter have been electrospun. Various electrospun fibers have been characterized by wide angle X-ray diffraction and by Raman spectroscopy. Electrospinning process has been observed by high speed photography.

In part II, the electrospun PAN, PAN/SAN, and PAN/SAN/CNT fiber mats were stabilized, carbonized, and processed into electrochemical capacitor electrodes. The performance of the electrochemical capacitors was tested by the constant current charge/discharge and cyclic voltammetry in 6 molar potassium hydroxide aqueous solution. The surface area and pore size distribution of the electrodes were measured using N_2 adsorption and desorption. The effect of surface area and pore size distribution on the capacitance performance has been studied. The capacitance performance of various carbonized electrospun fibers mats have been compared to those of the PAN/SAN/CNT film, carbon nanotube bucky paper, and activated carbon pellet. The capacitance of PAN/SAN/CNT fiber mat over 200 F/g (at a current

density of 1 A/g) and the power density approaching 1 kW/kg have been observed. Addition of 1 wt% carbon nanotubes in PAN/SAN, improves the power density by a factor of four. For comparison, the capacitance of single wall carbon nanotube bucky paper at a current density of 1 A/g is about 50 F/g.

CHAPTER 1

INTRODUCTION

Electrospinning is a fiber forming process that utilizes high voltage to generate nanometer diameter fibers. Important characteristics of electrospun fiber mats are high surface area and porosity, which have applications in air filtration, tissue engineering, drug delivery, and energy storage materials. An electrochemical capacitor is an energy storage device with long cycle life and fast charge/discharge capability. To achieve high performance, the materials for electrochemical capacitor electrodes require high surface area, appropriate porosity, good electrical conductivity, and chemical stability. The traditional electrochemical capacitor electrodes are processed in the form of film, activated carbon paste, or carbon fiber fabric. In recent years, electrospun nanofibers have also been used for electrochemical capacitor electrodes due to their high surface area and porosity. In this chapter, background, principles, and the current status of both the electrospinning and electrochemical capacitor fields are reviewed.

1.1 Electrospinning

Electrospinning was first demonstrated in 1902.[1] However, current interest in electrospinning dates back to early 1990s and the number of publications on the subject is rapidly increasing. Electrospinning is being practiced on natural polymers,[2] synthetic polymers, [3] biopolymers, [4] polymer solutions, [5] polymer melts, [6] liquid crystalline polymers,[7] polymer blends,[8] and sol-gel ceramic precursors.[9] To date, electrospinning has been explored to process nanometer to micrometer diameter solid, porous,[10] hollow,[9]

or bi-component continuous fibers, [11] microscopic cups, [12] and nanowires. [13] Electrospinning can also be used to make random as well as highly aligned fibers.[14, 15]

Figure 1.1 shows the schematic sketch of the electrospinning setup, which has three major parts: a high voltage power supply, a syringe pump, and a grounded target. A droplet forms due to surface tension on the needle tip, when the polymer solution or melt is delivered to it. Application of high electrical voltage gives a positive charge to this droplet. All charges in the droplet have the same polarity (positive charge), therefore an electrostatic repulsive force is generated between the adjacent entities in the droplet. On the other hand, an electrostatic attractive force exists between the positively charged droplet and the grounded target. Besides the electrostatic repulsive force and electrostatic attractive force, surface tension exists on the droplet, which holds the droplet on the needle tip (Figure 1.2).[16] When the applied voltage is low, the surface tension is sufficient to counterbalance the electrostatic repulsive force and electrostatic attractive force, and the droplet hangs on the needle tip. With increasing voltage, both electrostatic repulsive and electrostatic attractive forces increase, which are sufficient to overcome the surface tension. An electrified jet is thus pulled out from needle tip. The jet undergoes bending, looping, spiraling, and finally reaches the target. During this travel, the jet is stretched and elongated by the electrostatic repulsive or electrostatic attractive force, resulting in fine fibers.

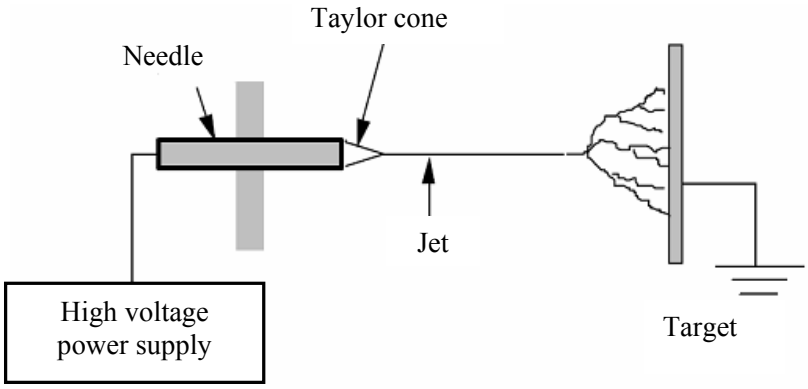

Figure 1.1. Schematic sketch of the electrospinning setup.

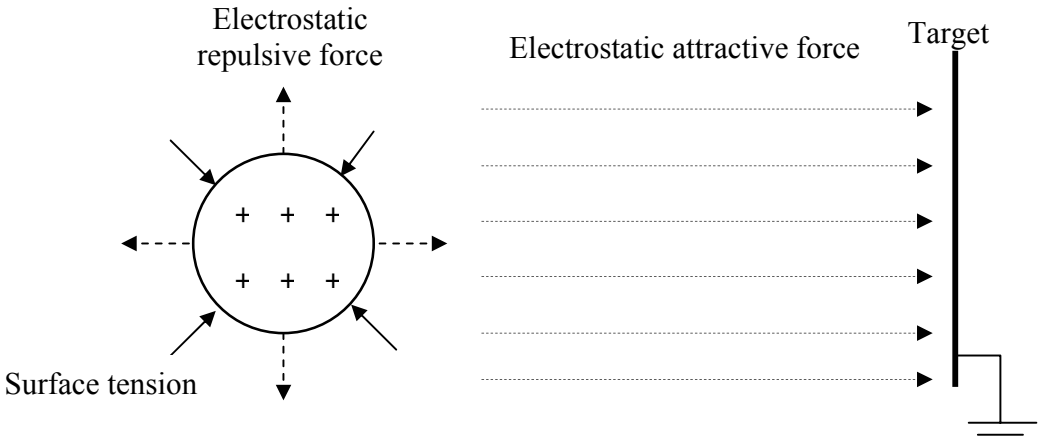

Figure 1.2. Schematic sketch of the forces applied onto a positively charged droplet. (From ref. 16.)

1.1.1 Electrospinning process

The electrospinning process involves two major stages: (1) Taylor cone formation and jet initiation; (2) Bending instability and elongation of the jet.

Taylor cone formation and jet initiation

A conical shape forms when applied electrostatic repulsive force is balanced with or exceeds the surface tension (Figure 1.3). This conical shape was named as "Taylor cone", and was first analyzed by Taylor (1964).[17] Taylor determined the semi-angle of this conical shape to be 49.3° for water droplet by equating the electrical force to the surface tension. Since then, the semi-angle of the Taylor cone has also been studied by other researchers. In other work, the semi-angles of Taylor cone for water and sunflower oil were reported to be 49 ± 2°and 49.5 ± 2°, respectively.[18] When electrospinning aqueous poly(ethylene oxide) (PEO) solution, Taylor cone with semi-angle of 33.5° was observed.[19] Taylor cone of less than 30° semi-angle was reported when electrospinning PEO in ethanol/water (40/60) mixture.[20] Though different values of semi-angle of Taylor cone have been reported in the literature, no explanation for the observation of different Taylor cone semi-angles has been provided. Critical voltage V_c needed for the ejection of the jet from the Taylor cone is given by the following equation:[21]

$$V_c^2 = \frac{4H^2}{L^2}\left(\ln\frac{2L}{R} - \frac{3}{2}\right)0.117\,\pi\gamma R$$

where, H is the distance between the tip of the needle (or capillary) and the grounded target, L is the length of the needle (or capillary), R is the radius of the needle, and γ is the surface tension of the solution.

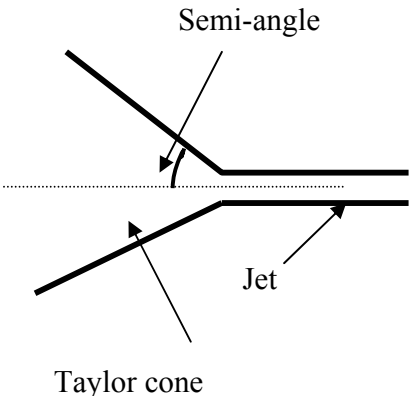

Figure 1.3. Schematic sketch of the Taylor cone.

Based on this equation, the critical voltage for electrospinning poly(acrylonitrile) (PAN)/dimethylformamide (DMF) solution is calculated as a function of the distance between the needle tip and the target or the radius of the needle and are plotted in Figures 1.4 and 1.5, respectively (where, L is 5 cm and γ for PAN/DMF solution is 37 mN/m).

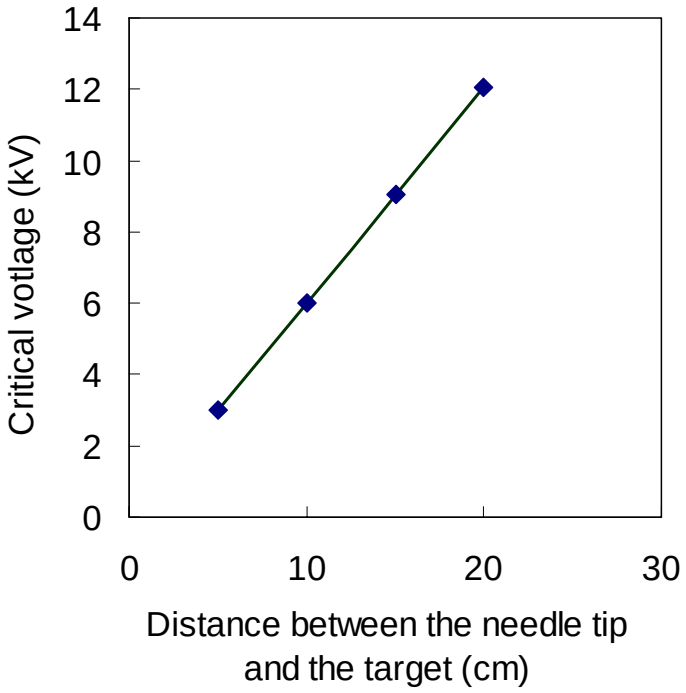

Figure 1.4. Critical voltage as a function of distance between the needle tip and the target (L is 5 cm, R is 0.042 cm, and γ for PAN/DMF solution is 37 mN/m).

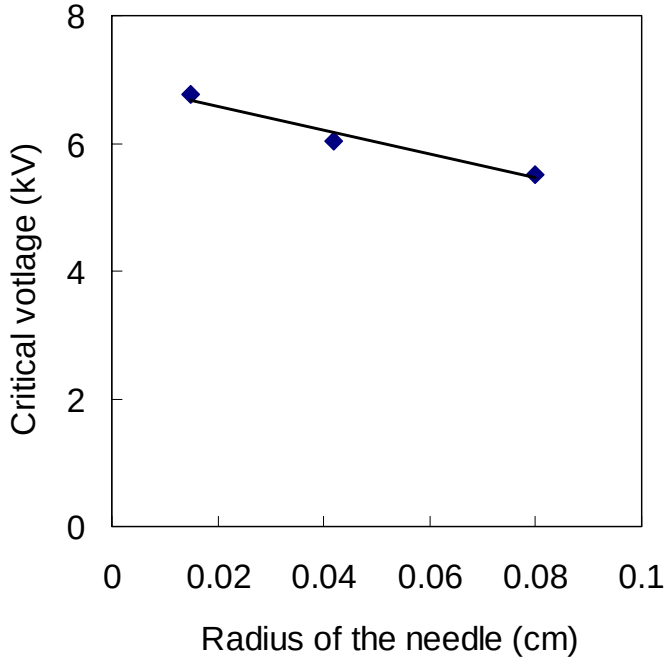

Figure 1.5. Critical voltage as a function of radius of the needle (L is 5 cm, H is 10 cm, and γ for PAN/DMF solution is 37 mN/m).

Bending instability and elongation of the jet

After initiating from the apex of the "Taylor cone", the electrically charged jet first travels in a straight line for a few centimeters then it undergoes bending and looping due to the jet instability. Figure 1.6 gives the high speed photograph of electrospinning process of PEO in ethanol/water (60/40) mixture,[22] showing a rapidly whipping single jet. Theoretical analysis of the jet whipping process in terms of charge density on the jet and its interaction with the external field has also been carried out.[23]

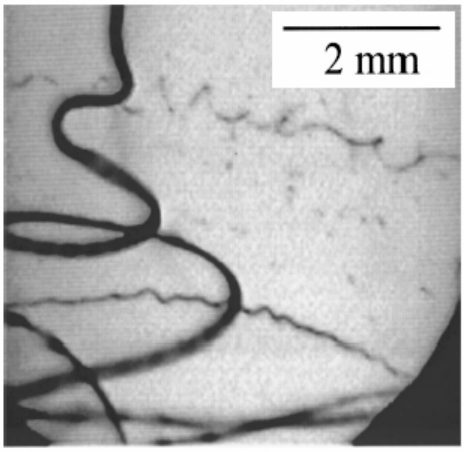

Figure 1.6. High speed photograph of electrospinning process of PEO in ethanol/water (60/40) with camera exposure time of 0.25 ms. (From ref. 22.)

1.1.2 Control of fiber diameter and morphology

Experimental studies show that three major groups of parameters affect fiber diameter and morphology: (1) Solution properties such as viscosity (polymer concentration and/or molecular weight), surface tension, electrical conductivity, dielectric constant, and solvent evaporation rate; (2) Processing factors such as voltage, distance between the needle tip and the target, and solution flow rate; (3) Environmental factors

such as humidity and temperature. In this section, the effects of these factors on electrospun fiber diameter and morphology are discussed.

Solution properties

Solution viscosity, which is affected by concentration, molecular weight, or the solvent characteristics, has the most significant effect on electrospun fiber morphology and diameter. The correlation between solution rheology and electrospun fiber morphology has been widely studied.[24, 25, 26] At low viscosity, "electrospraying" occurs where the jet breaks up into droplets; at high viscosity, electrospinning occurs where continuous fibers form. It has been reported that chain entanglement concentration was the critical concentration for electrospinning continuous fibers.[27] Below entanglement concentration, particles were obtained; above entanglement concentration, continuous fibers were obtained. Fiber diameter increased with concentration.[25, 28, 29, 30] Polymer molecular weight also determines chain entanglements in solution, therefore, it can affect the fiber morphology and diameter. For poly(vinyl alcohol) (PVA) aqueous solution with the same concentration, beaded fibers were obtained when electrospinning low molecular weight (M_w 9000-10,000 g/mol) PVA, while uniform bead free fibers were obtained when electrospinning high molecular weight (M_w 13,000-23,000 g/mol) PVA.[31]

Surface tension tends to minimize the surface area of the jet by forming beads on the fiber. Therefore, bead formation can be minimized by lowering surface tension of the solution. The surface tension can be lowered by using a low surface tension solvent[24] or by the addition of surfactant.[32] For example, the addition of 40 g ethanol into 57 g water lowered the surface tension of PEO/water solution from 76 to 51 mN/m and fibers with

fewer beads were obtained.[24] A high critical voltage was needed for electrospinning PVA/water solution since water had surface tension of 73 mN/m.[32] With the addition of a small amount of surfactant (Triton X-100) into water, the surface tension decreased, which lowered the critical voltage for electrospinning, and PVA fibers were subsequently obtained.

Good solution electrical conductivity increases the electrostatic repulsive force, which can strongly stretch the fiber jet, thus preventing bead formation and resulting in small diameter fibers. The good electrical conductivity of solution can come either from the solvent or by the addition of salt. For example, poly(styrene) (PS) solutions could not be electrospun into fibers when using decalin, 1, 4-dioxane, and ethylbenzene as solvents.[33] These solvents had very low electrical conductivity. However, by using solvents with high electrical conductivity such as DMF, ethylacetate, methylethylketone (MEK), and tetrahydrofuran (THF), PS fibers were obtained. With the addition of 2 wt% organic salt tetrabutylammonium chloride (TBAC) into poly(methyl methacrylate)(PMMA)/DMF solution, the fibers with fewer beads were thus obtained.[34] With the addition of 4 wt% poly(electrolyte), poly(allylamine hydrochloride) (PAH) or poly(acrylic acid sodium salt) (PAA) into the PEO/water solution, the conductivity was improved by a factor of three, and fibers diameter decreased from 0.36 to 0.15 μm.[35]

Solvent evaporation rate plays an important role on fiber morphology. By using volatile solvent, porous fibers can be obtained. For example, the pores with size of 100 nm in width and 250 nm in length were observed on the surface of poly-L-lactide fibers when electrospun from dichloromethane.[10] Porous PS nanofibers with pore size in the range of 20 nm to 1 μm were obtained when electrospun from THF.[36] By using

chloroform as solvent, poly(carbonate) (PC)/multi wall carbon nanotube (MWNT) nanofibers with elliptical shaped surface pores with size of 100 nm in width and 250 nm in length were obtained.[37] Porous cellulose triacetate (CTA) fibers with circular shape pores in the range of 50–100 nm were electrospun from methylene chloride.[38] The mechanism of pore formation during electrospinning is complicated. Phase separation due to fast solvent evaporation may be responsible for the pore formation.[10] During electrospinning, the volatile solvent evaporates fast, which causes original miscible polymer solution to separate into two phases: polymer-rich and solvent-rich phases. Once the fiber solidifies, the polymer-rich phase forms the fiber matrix while solvent-rich phase gives rise to the pores.

Processing factors

The effect of processing parameters such as applied voltage, flow rate, and the distance between the spinneret and the target on fiber diameter and morphology has also been studied.[39, 40] It was observed that fiber diameter of electrospun poly(sulfone) fibers showed a slight decrease from 344 ± 51 nm to 323 ± 22 nm when voltage was changed from 10 to 20 kV at a distance of 10 cm,[41] however, this change in diameter was within experimental error and therefore could be ignored. In other work, it was reported that fiber diameter decreased from about 20 to 10 μm with increasing voltage from 5 to 12 kV keeping other electrospinning conditions constant when electrospinning PS fibers.[36] Voltage also affects the shape and distribution of the defects. In the electrospun polycarbonate fibers, the defects changed from global mushroom to spindle shape due to the stronger stretching force with increasing voltage.[42] The effects of the tip to target

distance and solution flow rate on fiber morphology were also studied.[40] In this study, the morphologies of electrospun PVA did not change significantly when the tip to target distance was changed from 8 to 15 cm. However, solution flow rate slightly changed fiber morphology. With increasing flow rate, more beads were observed on the fibers.

Environmental factors such as temperature and humidity also affect fiber morphology. DMF is a non-volatile solvent and usually generates solid fibers. A novel approach to electrospin porous PAN fibers from DMF was recently reported where,[43] by immersing the collecting target into a bath of liquid nitrogen, porous PAN fibers were obtained through thermally induced phase separation. During this electrospinning process, when the fiber jet hit the liquid nitrogen bath, the solvent was frozen, and phase separation occurred, resulting in polymer-rich and solvent-rich regions. The solvent was subsequently removed in vacuum, and porous PAN fibers with surface area of 9.5 m^2/g were obtained. The effect of humidity on the morphology of electrospun PS/THF fibers was also studied.[44] When humidity was less than 25 %, no pores were visible in the fibers. With increasing humidity level, the number of pores increased significantly and the pore size ranged from 50 to 280 nm. Breath figure theory[45] was used to explain this phenomenon. Breath figures form when evaporative cooling occurs as a result of rapid solvent evaporation during jet travel. The jet surface cools down and the moisture from air condenses on the fiber surface. When the fiber dries, the water droplet regions form pores.

1.1.3 Applications of electrospun fiber mats

Due to the large specific surface area and porous structure, electrospun fibers are used for filtration, wound dressing, tissue engineering and reinforcement. [4, 19, 46, 47] The nanofibers are used for filtration media with high filtration efficiency, which have already been commercialized by eSpin Technologies, Inc.[48] and by Donaldson Company, Inc.[49] The electrospun fiber mat can be used as scaffold for cell growth in tissue engineering by mimicking the physical structure of extracellular matrix (ECM).[50, 51] In recent years, carbon nanofibers obtained by heat treatment of electrospun poly(amic acid) (PAA),[52] PAN,[53] and poly(benzimidazol) (PBI)[54] nanofibers were evaluated for electrochemical capacitor electrodes.

1.2 Electrochemical capacitor

1.2.1 Principles of electrochemical capacitor

Electrochemical capacitor, also known as double layer capacitor, is an energy storage device, which has long cycle life, higher power density than the battery, and higher energy density than the ordinary capacitor (Figure 1.7).[55] It bridges the gap between the capacitor and the battery, and has wide applications as main or backup power supply.

An electrochemical capacitor consists of two electrodes, electrolyte, and an insulating separator (Figure 1.8). When an electrochemical capacitor is charged, one electrode is positively polarized and another is negatively polarized. The electrolyte dissociates into positive and negative ions, which can combine with solvent molecules to form “solvated ions”. The solvated ions move close to the electrodes with opposite polarity, accumulate at the interface between the electrode and the electrolyte, and form a

double layer structure as shown in Figure 1.8. The thickness of the double layer is usually in the range of 5-10 Å. Thus the electrochemical capacitor is also called as "double layer capacitor". When the electrochemical capacitor is discharged, the electrolyte ions leave the electrodes, combine together and neutralize, energy is thus released.

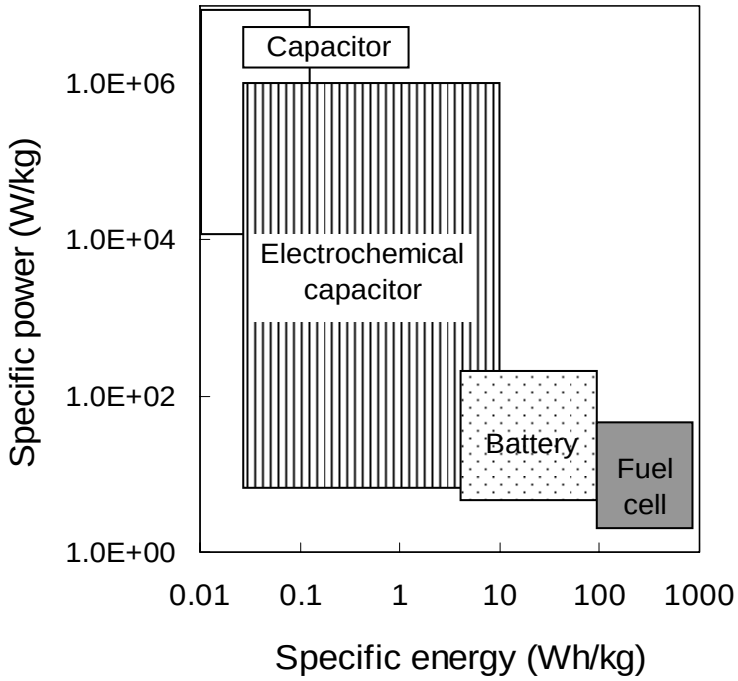

Figure 1.7. Comparison of specific power and energy densities of various energy storage devices. (From ref. 55.)

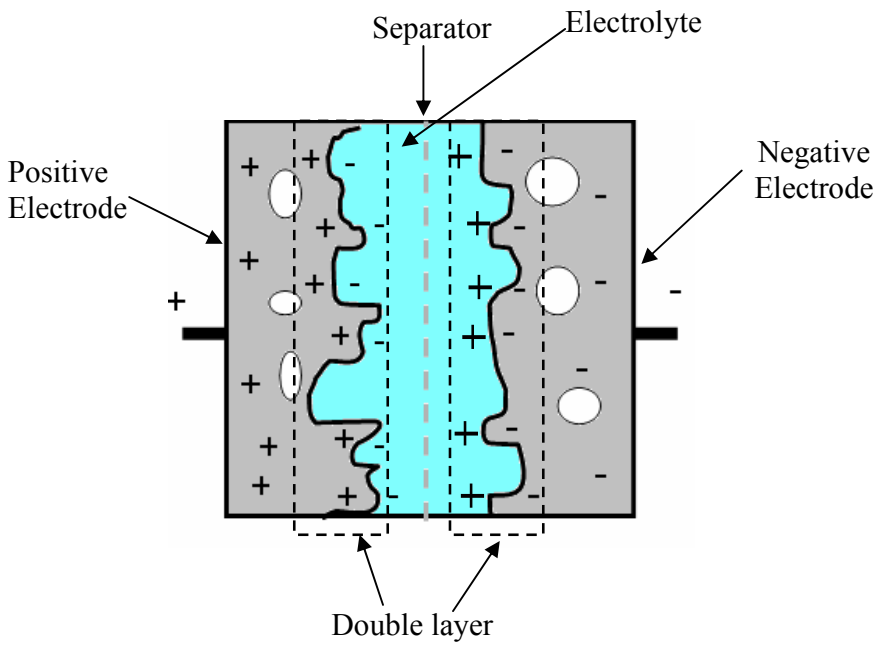

Figure 1.8. Schematic sketch of an activated carbon based double layer capacitor. (From Ref. 56.)

The performance of an electrochemical capacitor can be evaluated by the following parameters: capacitance, power density, and energy density. For a cell consisting of two electrodes, the total capacitance is determined by the capacitance of each electrode as below:

$$1/C = 1/C_1 + 1/C_2$$

where C_1 and C_2 are capacitances of two electrodes.

The maximum power density of an electrochemical capacitor is given by:

$$P_{max} = V^2/4R$$

where P is power density, V is the maximum voltage, which is determined by the decomposition voltage of the electrolyte (for organic electrolyte the decomposition

voltage is in the range of 2~3 V, and for aqueous electrolyte the decomposition voltage is about 1 V), and R is the equivalent series resistance.

The maximum energy density of an electrochemical capacitor is given by:

$$W_{max} = ½ CV^2$$

where W is energy density, C is capacitance, V is the maximum voltage, which is determined by the decomposition voltage of the electrolyte. For an electrochemical capacitor with capacitance of 200 F/g and the decomposition voltage of 1 V, the energy density is calculated to be 100 J/g.

1.2.2 Electrochemical capacitor testing

The performance of an electrochemical capacitor can be characterized by galvanostatic and cyclic voltammetry methods. When using the galvanostatic method (constant current charge/discharge, CC), the electrochemical capacitor is charged and discharged at a constant current within a potential range of 0 to V_{max} (V_{max} is the decomposition voltage of the electrolyte), and the voltage (V) is recorded as a function of time (t). Figure 1.9 shows a typical CC charge/discharge cycle.

When using the cyclic voltammetry (CV) method, the voltage (V) is swept between two voltages (V_1 and V_2) at a constant scan rate (s).[57] The resulting current (I) is recorded as a function of time (t). The current is plotted as a function of voltage in Figure 1.10. For an ideal double layer capacitor, the current is independent of potential and shows a rectangular plot. However, if redox reactions occur, the rectangular shape is distorted, showing a reduction and an oxidation peaks.

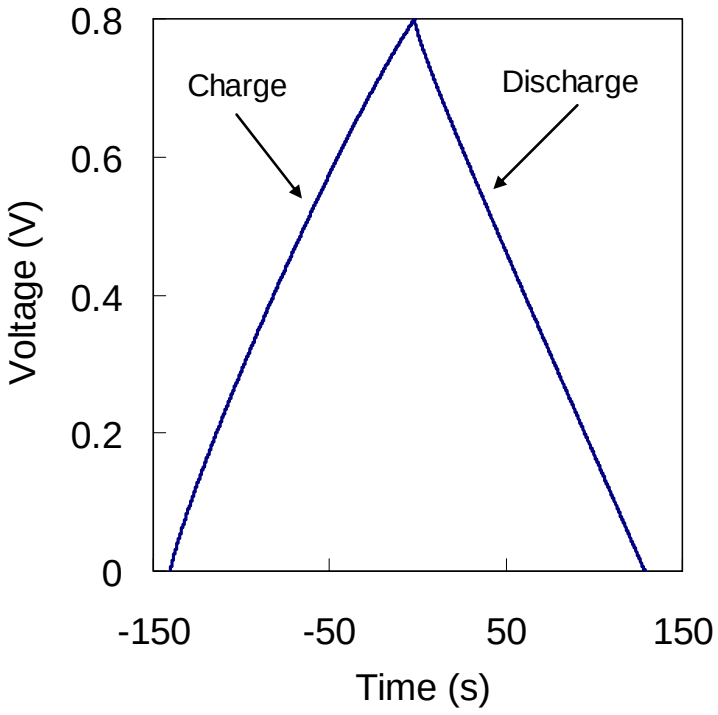

Figure 1.9. Typical charge/discharge cycle in constant current charge/discharge method.

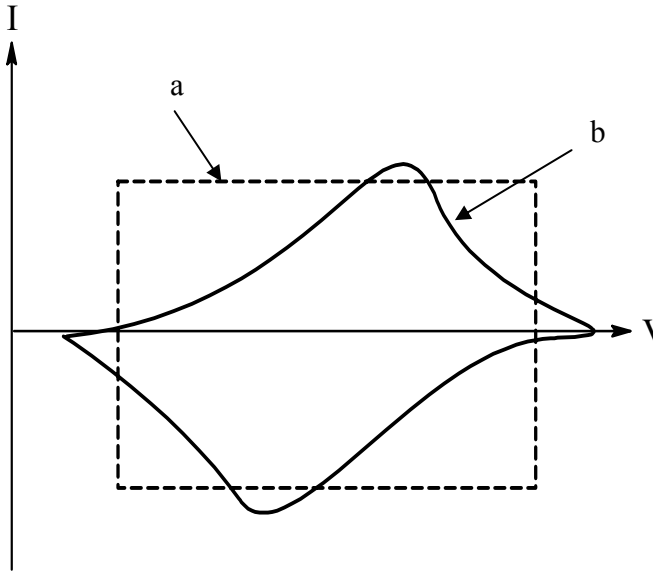

Figure 1.10. Typical I vs. V cyclic voltammetry response of (a) an ideal double layer capacitor and (b) a double layer capacitor with redox reaction.

1.2.3 Electrode materials

Three groups of materials are typically used for electrochemical capacitor electrodes: metal oxides, conducting polymers, and porous carbon. In this section, the literature on these materials based electrochemical capacitor electrodes is briefly reviewed.

1.2.3.1 Metal oxide based electrochemical capacitor electrodes

Metal oxides such as RuO_2 or IrO_2 can be processed into electrochemical capacitor electrodes. The typical cyclic voltammogram exhibits a shape close to rectangular as shown in Figure 1.11.[58] However, this plot does not come from a pure double layer charge/discharge; rather, it comes from a sequence of redox reactions occurring in metal oxide. In metal oxide based electrochemical capacitor, the redox reactions during charge/discharge process are reversible, and anodic and cathodic voltammograms are almost mirror images of each another, resulting in a shape close to rectangular. The high capacitance can be obtained when using metal oxides as electrochemical capacitor electrodes. It was reported that specific capacitance of RuO_2 based electrochemical capacitor reached 720 F/g using H_2SO_4 electrolyte.[59] The NiO based electrochemical capacitor had capacitance about 120 F/g using KOH electrolyte.[60] The specific capacitance of $SrRuO_3$ based electrochemical capacitor was about 360 F/g using KOH electrolyte.[61]

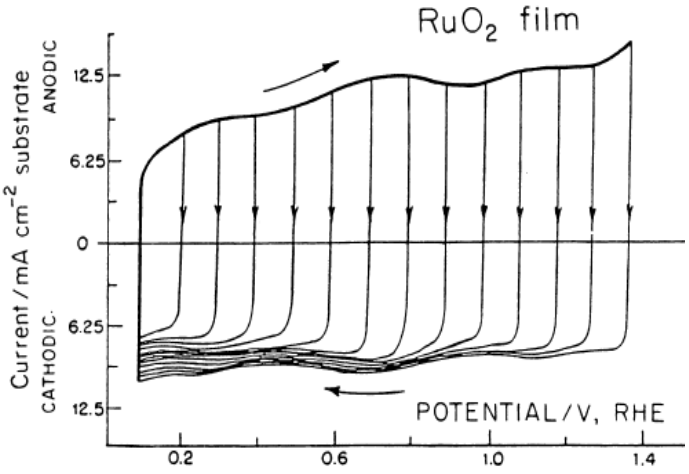

Figure 1.11. Cyclic voltammetry profiles for RuO_2 in 0.1 M H_2SO_4 aqueous solution. (From ref. 56.)

1.2.3.2 Electrically conducting polymer based electrochemical capacitor electrodes

Electrically conducting polymers such as poly(aniline) and poly(pyrrole) have been used for making electrochemical capacitor electrodes. The cyclic voltammogram of conducting polymer based electrochemical capacitor deviates from rectangular shape and shows an oxidation and reduction peak (Figure 1.12).[62] Due to the redox reactions, conducting polymer based electrochemical capacitors have high capacitance. An electrochemical capacitor with specific capacitance value of 775 F/g was obtained by electrochemically depositing poly (aniline) nanowires on stainless steel using H_2SO_4 electrolyte.[63] A high performance poly(pyrrole) based electrochemical capacitor was prepared by electrodepositing on Ti foil using oxalic acid and pyrrole mixture electrolyte, which had specific capacitance as high as 480 F/g.[64] High power density can also be

obtained by using conducting polymers as electrodes due to their low resistance. The power density of poly(3, 4-ethylenedioxythiophene) based electrochemical capacitor reached as high as 2.5 kW/kg at current density of 1 mA/cm^2 using $LiClO_4$ acetonitrile solution electrolyte.[65] However, faradaic reactions occur during charge/discharge processes, which shorten the cycle life.

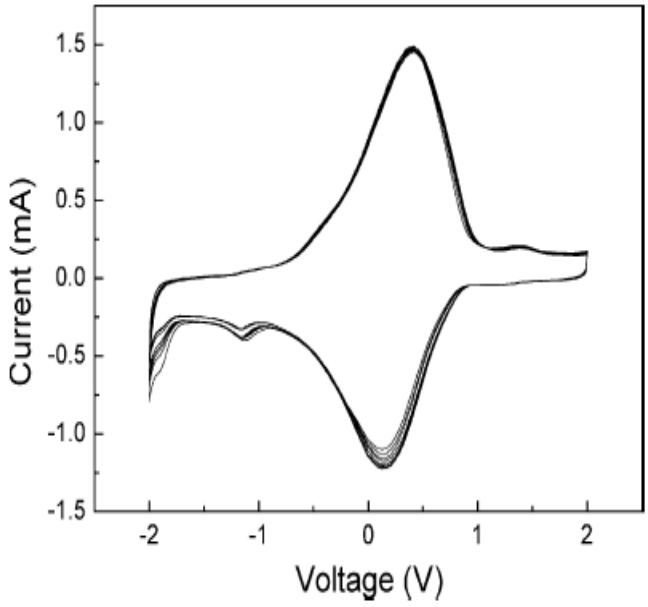

Figure 1.12. The cyclic voltammetry of electrochemical capacitor using poly(aniline). (From ref. 63.)

1.2.3.3 Carbon based electrochemical capacitor electrodes

Carbon materials are good candidates for electrochemical capacitor electrodes. To achieve high electrochemical capacitor performance, carbon needs to meet the following requirements:[56]

- High surface area (1000 ~ 2000 m^2/g) with appropriate pore size that can accommodate electrolyte ions
- Good electrical conductivity
- Minimized ohmic resistance
- Mechanical stability
- Good wettability by the electrolyte

Carbon materials including activated carbon and carbon nanotubes have been processed into electrochemical capacitor electrodes, and the relevant literature is briefly reviewed below.

Activated carbon electrodes

Carbon precursors such as pitch,[66] coal,[67] cotton,[68] and PAN[69] can be converted into activated carbon via heat treatment. For example, PAN is converted into porous carbon using stabilization, carbonization, and activation process. For stabilization, PAN is heat treated in air in the temperature range of 200 to 300 °C. During this step, PAN partially cyclizes and forms ladder structure. The stabilized PAN is then carbonized in an inert atmosphere at temperature ranging from 700 to 3000 °C.

Activation is an important step in creating porosity and modifying surface chemistry of the activated carbon. After activation, porous carbon with surface area as high as 1000~2000 m^2/g can be obtained. Depending on the activation agent used, activation process can be classified into physical or chemical activation. In physical activation, oxidative gases such as steam[70] or CO_2[71] are used; in chemical activation, chemical agents such as $ZnCl_2$,[72] KOH,[73] or K_2CO_3[74] are used.

Effect of surface area and porosity on activated carbon based electrochemical capacitor electrodes has been studied. It was reported that the capacitance is not linearly proportional to surface area.[75, 76, 77, 78] Two major reasons are considered responsible for this observation. First, double layer capacity (capacitance per unit area) varies depending on precursor and processing approaches, and secondly, the accessibility of pores by the electrolyte ions needs to be considered. The performance of activated carbon based electrochemical capacitor electrodes in aqueous and organic electrolytes was also studied.[66] It showed that the activated carbon materials exhibited different electrochemical performance in different electrolytes. The activated carbon with large pore size (> 3 nm) exhibited high capacitance in both aqueous and organic electrolytes. The activated carbon with medium pore size (~ 2 nm) showed high capacitance in aqueous electrolyte, but low capacitance in organic electrolyte. The activated carbon with relatively small pore size (< 1.5 nm) showed low capacitance in both aqueous and organic electrolytes. Based on these studies, it was concluded that the pores with size less than the solvated electrolyte ions are not useful. However, this argument was recently challenged by an observation of an anomalous increase of capacitance with pore size less than 1 nm in carbide derived carbon.[79] The distortion of electrolyte ion shell in small pores decreased the distance between the ion centers to the electrode surface, which decreased the double layer thickness and therefore improved the capacitance.

Carbon nanotube electrodes

Carbon nanotubes are good candidates for electrochemical capacitor electrodes due to their high electrical conductivity, chemical stability, low density, and large surface

area. The performance of carbon nanotube based electrochemical capacitor electrodes depends on carbon nanotube type,[80] morphology,[57] and functional groups[81] etc.

Electrochemical capacitors processed by using MWNT and single wall carbon nanotube (SWNT) were reported.[80] MWNT based electrochemical capacitor had specific capacitance of 80 F/g in KOH, which was more than two times the value for SWNT based electrochemical capacitor. Locally aligned carbon nanotube films were also used to process high power density electrochemical capacitors.[82] The high packing density and ordered structures of carbon nanotubes resulted in specific power density as high as 30 kW/kg. The specific capacitance of SWNT based electrochemical capacitor reached as high as 280 F/g when using acetonitrile electrolyte containing 0.1 M tetra-n-butylammonium hexafluorophosphate as electrolyte.[83] The performance of the electrochemical capacitor processed from oxidized carbon nanotube [84] was reported and showed that the morphologies and structure of individual carbon nanotube were modified by annealing, which improved the specific capacitance from 25 to 50 F/g. MWNT based electrochemical capacitor with specific capacitance as high as 113 F/g was obtained when using H_2SO_4 electrolyte.[85]

Pseudocapacitance

In an ideal double layer capacitor, energy is stored in a double layer and no charge transfer occurs across the interface between the electrode and the electrolyte. However, it is possible that some redox reactions still happen. The capacitance arising from these faradaic reactions is called “pseudocapcitance”. Therefore the double layer capacitance is not only from electrostatic charge but also arises from quick faradaic charge transfer reactions, which is given as below:

$$C_{total} = C_{dl} + C_f$$

where C_{total} is total capacitance, C_{dl} is electrical double layer capacitance, C_f is pseudocapacitance.

By introducing functional groups onto carbon material, depositing conducting polymers or by inserting electroactive particles of transition metals, pseudocapacitance can be enhanced. Poly(pyrrole) coated MWNTs were processed as electrochemical capacitor electrodes, [86] and the specific capacitance reached as high as 192 F/g. Modification of the carbon aerogel by ruthenium oxide particles improved the specific capacitance of electrochemical capacitor from 95 to 200 F/g.[87] The specific capacitance of pyrrole treated-functionalized SWNT bucky paper based electrodes was reported to be 350 F/g.[88]

PAN based electrochemical capacitor electrodes

PAN is a carbon precursor, which can be converted into activated carbon by heat treatment. The electrochemical capacitor electrodes were processed using PAN film or fiber as precursor. PAN/SWNT film based electrochemical capacitor electrodes have been reported by our research group.[89] Carbon nanotubes formed bundled structure in PAN matrix, which could resist the shrinkage of PAN during heating and also improved the electrical conductivity. The PAN/SWNT (60/40) film was stabilized, carbonized, activated, and processed into electrochemical capacitor electrodes, which exhibited specific capacitance as high as 380 F/g using KOH electrolyte. The PAN/SAN (styrene-co-acrylonitrile)/SWNT film based electrochemical capacitors were also processed by stabilization and carbonization.[90] With the addition of sacrificial component, SAN, the

pores with size ranging from 1-200 nm were obtained in the carbonized film, and the double layer capacity reached as high as 205 $\mu F/cm^2$ in KOH. The electrochemical capacitor electrodes were processed by one step pyrolysis of PAN/MWNT film,[91] which exhibited capacitance value of 100 F/g in H_2SO_4. Activated carbon based electrochemical capacitor processed from PAN with a capacitance value of 160 F/g in H_2SO_4 was reported.[92] The carbon nanofibers processed from electrospun PAN fibers were also used for electrochemical capacitor electrodes, which exhibited specific capacitance as high as 170 F/g.[53]

1.3 Objectives of this study

Two key objectives of this study are:

- To study the effect of various factors such as polymer solution concentration, solvents characteristics, polymer molecular weight, voltage, distance between the needle tip and the target, and solution flow rate on the diameter and morphology of electrospun PAN.
- To study the electrochemical performance of the electrospun PAN, PAN/SAN, and PAN/SAN/CNT nanofibers. In this study SAN is used as the sacrificial component to provide porosity control and CNTs are added to enhance conductivity and hence power density.

1.4 References

1. W. J. Morton, U.S. Patent, **1902,** No. 705, 691.

2. J. Xie and Y. L. Hsieh, Journal of Materials Science, **2003**, 38, 2125.

3. R. Jaeger, H. Schönherr, and G. J. Vancso, Macromolecules, **1996**, 29, 7634.

4. J. A. Matthews, G. E. Wnek, D. G. Simpson, and G. L. Bowlin, Biomacromolecules, **2002**, 3, 232.

5. A. Pedicini and R. J. Farris, Polymer, **2003**, 44, 6857.

6. J. Lyons, C. Li, and F. Ko, Polymer, **2004**, 45, 7597.

7. D. Y. Lin and D. C. Martin, Polymer Preprints (American Chemical Society, Division of Polymer Chemistry), **2003**, 44, 70.

8. Y. Dror, W. Salalha, R. L. Khalfin, Y. Cohen, A. L. Yarin, and E. Zussman, Langmuir, **2003**, 19, 7012.

9. D. Li and Y. Xia, Nano Letters, **2004**, 4, 933.

10. M. Bognitzki, M. Czado, T. Frese, A. Schaper, M. Hellwig, M. Steinhart, A. Greiner, and J. H. Wendorff, Advanced Materials, **2001**, 13, 70.

11. J. H. Yu, S. V. Fridrikh, and G. C. Rutledge, Advanced Materials, **2004**, 16, 1562.

12. J. Liu and S. Kumar, Polymer, **2005**, 46, 3211.

13. J. Liu, T. Wang, and S. Kumar, Journal of Applied Polymer Science, **2005**, 96, 1992.

14. D. Li, Y. Wang, and Y. Xia, Advanced Materials, **2004**, 16, 361.

15. J. S. Kim and D. H. Reneker, Polymer Engineering and Science, **1999**, 39, 849.

16. P. Gupta, PhD thesis, Virginia Polytechnic Institute and State University, **2004**.

17. G. Taylor, Proceedings of the Royal Society of London, Series A, **1964**, 280, 383.

18. J. S. Eow and M. Ghadiri, Colloids and Surfaces A: Physicochemical Engineering Aspects, **2003**, 215, 101.

19. A. L. Yarin, S. Koombhongse, and D. H. Reneker, Journal of Applied Physics, **2001**, 90, 4836.

20. S. N. Reznik, A. L. Yarin, A. Theron, and E. Zussman, Journal of Fluid Mechanics, **2004**, 516, 349.

21. G. Taylor, Proceedings of the Royal Society of London, Series A, **1969**, 313, 453

22. D. H. Reneker, A. L. Yarin, H. Fong, and S. Koombhongse, Journal of Applied Physics, **2000**, 87, 4531.

23. M. M. Hohman, M. Shin, G. C. Rutledge, and M. P. Brenner, Physics of Fluids, **2001**, 13, 2221.

24. H. Fong, I. Chun, and D. H. Reneker, Polymer, **1999**, 40, 4585.

25. P. Gupta, C. Elkins, T. E. Long, and G. L. Wilkes, Polymer, **2005**, 46, 4799.

26. C. Huang, S. Chen, C. Lai, D. H. Reneker, H. Qiu, Y. Ye, and H. Hou, Nanotechnology, **2006**, 17, 1558.

27. M. G. Mckee, G. L. Wilkes, R. H. Colby, and T. E. Long, Macromolecules, **2004**, 37, 1760.

28. C. M. Uppatham, M. Nithitanakul, and P. Supaphol, Macromolecular Chemistry and Physics, **2004**, 205, 2327.

29. J. M. Deitzel, J. Kleinmeyer, D. Harris, and N. C. Beck Tan, Polymer, **2001**, 42, 261.

30. M. M. Demir, I. Yilgor, E. Yilgor, and B. Erman, Polymer, **2002**, 43, 3303.

31. A. Koski, K. Yim, and S. Shivkumar, Materials Letters, **2004**, 58, 493.

32. L. Yao, T. W. Haas, A. G. Elie, G. L. Bowlin, D. G. Simpson, and G. E. Wnek, Chemistry of Materials, **2003,** 15, 1860.

33. T. Jarusuwannapoom, W. Hongrojjanawiwat, S. Jitjaicham, L.Wannatong, M. Nithitanakul, C. Pattamaprom, P. Koombhongse, R. Rangkupan, and P. Supaphol, European Polymer Journal, **2005**, 41, 409.

34. H. Dong, V. Nyame, A. G. MacDiarmid, and W. E. Jones Jr., Journal of Polymer Science: Part B: Polymer Physics, **2004**, 42, 3934.

35. W. K. Son, J. H. Youk, T. S. Lee, and W. H. Park, Polymer, **2004**, 45, 2959.

36. S. Megelski, J. S. Stephens, D. B. Chase, and J. F. Rabolt, Macromolecules, **2002**, 35, 8456.

37. G. M. Kim, G. H. Michler, and P. Pötschke, Polymer, **2005**, 46, 7346.

38. S. O. Han, W. K. Son, J. H. Youk, T. S. Lee, and W. H. Park, Materials Letters, **2005**, 59, 2998.

39. C. M. Hsu and S. Shivkumar, Journal of Materials Science, **2004**, 39, 3003.

40. C. Zhang , X. Yuan, L. Wu, Y. Han, and J. Sheng, European Polymer Journal, **2005**, 41, 423.

41. X. Yuan, Y. Zhang, C. Dong, and J. Sheng, Polymer International, **2004**, 53, 1704.

42. J. Shawon and C. Sung, Journal of Material Science, **2004**, 39, 4605.

43. J. T. McCann, M. Marquez, and Y. N. Xia, Journal of the American Chemical Society, **2006**, 128, 1436.

44. C. L. Casper, J. S. Stephens, N. G. Tassi, D. B. Chase, and J. F. Rabolt, Macromolecules, **2004**, 37, 573.

45. M. Srinivasarao, D. Collings, A. Philips, and S. Patel, Science, **2001**, 292, 79.

46. A. Theron, E. Zussman E, and A. L. Yarin, Nanotechnology, **2001**, 12, 384.

47. X. Zong, K. Kim, D. Fang, S. Ran, B. S. Hsiao, and B. Chu, Polymer, **2002**, 43, 4403.

48. www.espintechnologies.com.

49. www.donaldson.com.

50. A. S. Badami, M. R. Kreke, M. S. Thompson, J. S. Riffle, and A. S. Goldstein, Biomaterials, **2006**, 27, 596.

51. F. Yang, R. Murugan, S. Wang, and S. Ramakrishna, Biomaterials, **2005**, 26, 2603.

52. C. Kim, Y. O. Choi, W. J. Lee, and K. S. Yang, Electrochimica Acta, **2004**, 50, 883.

53. C. Kim and K. S. Yang, Applied Physics Letters, **2003**, 83, 1216.

54. C. Kim, S. H. Park, W. J. Lee, and K. S. Yang, Electrochimica Acta, **2004**, 50, 877.

55. R. Kötz and M. Carlen, Electrochimica Acta, **2000**, 45, 2483.

56. B. E. Conway, Electrochemical Capacitors, Scientific Fundamental and Technological Applications, Plenum Publishers, **1999.**

57. E. Frackowiak and F. Béguin, Carbon, **2001**, 39, 937.

58. B. E. Conway and W. G. Pell, Journal of Solid State Electrochemistry, **2003**, 7, 637.

59. J. P. Zheng, P. J. Cygan, and T. R. Jow, Journal of the Electrochemical Society, **1995**, 142, 2699.

60. Y. G. Wang and Y. Y. Xia, Electrochimica Acta, **2006**, 51, 3223.

61. M. W. Mehrens, J. Schenk, P. M. Wilde, E. Abdelmula, P. Axmann, and J. Garche, Journal of Power Sources, **2002**, 105, 182.

62. K. S. Ryu, K. M. Kim, Y. J. Park, N. G. Park, M. G. Kang, and S. H. Chang, Solid State Ionics, **2002**, 152-153, 861.

63. V. Gupta and N. Miura, Materials Letters, **2006**, 60, 1466.

64. L. Z. Fan and J. Maier, Electrochemistry Communications, **2006**, 8, 937.

65. J. C. Carlberg and O. Inganäs, Journal of the Electrochemical Society, 1997, 144, L61.

66. M. Endo, T. Maeda, T. Takeda, Y. J. Kim, K. Koshiba, H. Hara, and M. S. Dresslhaus, Journal of the Electrochemical Society, **2001**, 148, A910.

67. G. Gryglewicz, J. Machnikowski, E. L. Grabowska, G. Lora, and E. Frackowiak, Electrochimica Acta, **2005**, 50, 1197.

68. G. Salitra, A. Soffer, L. Eliad, Y. Cohen, and D. Aurbach, Journal of the Electrochemical Society, **2000**, 147, 2486.

69. F. Ko, Y. Gogotsi, A. Ali, N. Naguib, H. Ye, G. Yang, C. Li, and P. Willis, Advanced Materials, **2003**, 15, 1161.

70. W. Shen, J. Zheng, Z. Qin, and J. Wang, Journal of Colloid and Interface Science, **2003**, 264, 467.

71. M. Turmuzi, W. R. W. Daud, S. M. Tasirin, M. S. Takriff, S. E. Iyuke, Carbon, **2004**, 42, 453.

72. M. O. Marín, C. F. González, A. M. García, and V. G. Serrano, Applied Surface Science, **2006**, 252, 5967.

73. Q. Jiang, Y. Zhao, X. Y. Lu, X. T. Zhu, G. Q. Yang, L. J. Song, Y. D. Cai, X. M. Ren, and L. Qian, Chemical Physics Letters, **2005**, 410, 307.

74. J. Hayashi, T. Horikawa, K. Muroyama, and V. G. Gomes, Microporous and Mesoporous Materials, **2002**, 55, 63

75. E. Raymundo-Pin˜ero, K. Kierzek, J. Machnikowski, and F. Be´guin, Carbon, **2006**, 44, 2498.

76. Ch. Emmenegger, Ph. Mauron, P. Sudan, P. Wenger, V. Hermann, R. Gallay, and A. Züttel, Journal of Power Sources, **2003**, 124, 321.

77. T. C. Weng and H. Teng, Journal of the Electrochemical Society, 2001, **148,** A368.

78. T. Osaka, X. Liu, M. Nojima, and T. Momma, Journal of the Electrochemical Society, **1999**, 146, 1724.

79. J. Chmiola, G. Yushin, Y. Gogotsi, C. Portet, P. Simon, and P. L. Taberna, Science, **2006**, 313, 1760.

80. E. Frackowiak, K. Jurewicz, S. Delpeux, and F. Béguin, Journal of Power Sources, **2001**, 97-98, 822.

81. K. H. An, K. K. Jeon, J. K. Heo, S. C. Lim, D. J. Bae, and Y. H. Lee, Journal of the Electrochemical Society, **2002**, 149, A1058.

82. C. S. Du, J. Yeh, and N. Pan, Nanotechnology, **2005**, 16, 350.

83. C. Y. Liu, A. J. Bard, F. Wudl, I. Weitz, and J. R. Heath, Electrochemical and Solid-State Letters, **1999**, 2, 577.

84. C. Li, D. Wang, T. Liang, X. Wang, J. Wu, X. Hu, and J. Liang, Powder Technology, **2004**, 142, 175.

85. C. Niu, E. K. Sichel, R. Hoch, D. Moy, and H. Tennent, Applied Physics Letters, **1997**, 70, 1480.

86. M. Hughes, G. Z. Chen, M. S. P. Shaffer, D. J. Fray, and A. H. Windle, Chemistry of Materials, **2002**, 14, 1610.

87. J. M. Miller, B. Dunn, T. D. Tran, and R. W. Pekala, Journal of the Electrochemical Society, **1997**, 144, L 309.

88. C. Zhou, S. Kumar, C. D. Doyle, and J. M. Tour, Chemistry of Materials, **2005**, 17, 1997.

89. T. Liu, T. V. Sreekumar, S. Kumar, R. H. Hauge, and R. E. Smalley, Carbon, **2003**, 41, 2440.

90. C. Zhou, T. Liu, T. Wang, and S. Kumar, Polymer, **2006**, 47, 5831.

91. F. Béguin, K. Szostak, G. Lota, and E. Frackowiak, Advanced Materials, **2005**, 17, 2380.

92. E. Frackowiak, G. Lota, J. Machnikowski, C. V. Guterl, and F. Béguin, Electrochimica Acta, **2006**, 51, 2209.

CHAPTER 2

ELECTROSPINNING OF POLY(ACRYLONITRILE) AND POLY (ACRYLONITRILE) / CARBON NANOTUBE NANOFIBERS

2.1 Introduction

Due to the large surface area and porosity, carbon nanofibers are attractive for hydrogen storage,[1, 2] electrochemical capacitor electrodes,[3, 4] catalysis,[5, 6] and polymer reinforcement.[7] Electrospinning can be used to process nanometer diameter fibers. Poly(acrylonitrile) (PAN) is a carbon precursor and is used in this study to process electrochemical capacitor electrodes. The diameter of PAN nanofibers determines the surface area, which ultimately influences the performance of the materials made from the resulting carbon nanofibers. To achieve an effective fiber diameter control, a systematic electrospinning study of PAN as a function of solution concentration, electric field, solution flow rate, and solvent properties is reported in this chapter. Processing conditions have been developed for electrospinning small diameter bead free PAN fibers. Electrospinning behavior of PAN/carbon nanotube (CNT) dispersions was also studied. The electrospun fibers were characterized by wide angle X-ray diffraction (WAXD) and Raman spectroscopy. The electrospinning process was also observed by high speed photography.

2.2 Experimental

2.2.1 Sample preparation

Poly(acrylonitrile-co-methyl acrylate) copolymer (molecular weight 100,000 g/mol, containing about 4 wt% methacrylate copolymer) and poly(acrylonitrile) homopolymer (molecular weight 250,000 and 700,000 g/mol) obtained from Exlan

Corp. of Japan were dried at 95 °C in vacuum for 48 hrs, and dissolved in desired solvent. N, N–dimethylformamide (DMF), dimethyl sulfoxide (DMSO), nitromethane, and $ZnCl_2$ were purchased from Aldrich (Milwaukee, WI).

PAN/single wall carbon nanotube (SWNT) and PAN/multi wall carbon nanotube (MWNT) dispersions were prepared. To make PAN/SWNT (95/5) dispersion, about 0.12 g SWNT (HiPCO^{TM} SWNT, containing 35 wt% catalytic impurities was received from Carbon Nanotechnologies Inc., Houston, TX) was first dispersed in 300 ml DMF and sonicated in a bath sonicator (Cole–Parmer 8891R-DTH, 80 W, 43 kHz, Vernon Hills, IL) for 24 hrs. To this SWNT/DMF dispersion, about 2.28 g PAN copolymer powder was added and dissolved by high speed stirring until homogenous dispersion was obtained. Then the excess DMF was removed by heating and stirring until the total solid content was about 12 wt%. Following the same procedure, 20 ml PAN/SWNT (99.9/0.1) dispersion with 12 wt% solid content was prepared with the addition of 2.39 g PAN copolymer powder and 2.4 mg SWNT. To make PAN/MWNT (70/30) dispersion, 600 mg MWNT (Iljin Nanotech Co. Ltd, Seoul, Korea) was first dispersed in 300 ml DMF in a bath sonicator for 24 hrs and was subsequently sonicated by a horn sonicator (Model 2020, Misonix Inc., Farmingdale, NY) for 30 min. To this MWNT/DMF dispersion, 1.4 g PAN copolymer powder was added and dissolved by high speed stirring until homogenous dispersion was obtained. Then the excess DMF was removed by heating and stirring until the total solid content was about 10 wt%.

To prepare PAN/$ZnCl_2$ (99/1) solution, about 0.50 g PAN copolymer powder and 0.005 g $ZnCl_2$ were first dissolved into 10 ml DMF. The total solid content of PAN and $ZnCl_2$ was about 5.1 wt%. Following the same procedure, the PAN/$ZnCl_2$ (99/1) solutions with solid content of 9.6 wt% and 16.1 wt% and the PAN/$ZnCl_2$ (95/5)

solutions with solid content of 5.1 wt%, 9.6 wt%, and 16.1 wt% were also prepared. The PAN/$ZnCl_2$ solution was subsequently homogenized using a bio-homogenizer (Biospec products Inc., M133/1281-0, ESGE, Switzerland) for 5 min. The homogenized solution was filtered using a poly(tetrafluoroethylene) (PTFE) syringe filter with pore size of 0.2 μm (Cole Parmer Vernon Hills, Illinois).

In a horizontal electrospinning setup, PAN solutions or PAN/CNT dispersions were loaded into a syringe and delivered to the tip of the 18 gauge (0.84 mm diameter) stainless steel needle using a syringe pump (KDS 100, KD Scientific Inc., Holliston, MA). A high voltage research power supply (model GPR-3060D, Gamma High Voltage Research Inc., Ormond Beach, FL) was applied to the solution via the needle. The electrospun fiber mats were collected on the aluminum foil wrapped on the grounded steel sheet target.

A PAN/SWNT (99.9/0.1) composite film for Raman spectroscopy study was prepared from PAN/SWNT (99.9/0.1) dispersion in DMF with solids content of 12 wt%. The dispersion was poured in a petri dish and the solvent was evaporated in air at room temperature for one week. Three films were prepared for WAXD study, which were designated as Film-A, Film-B, and Film-C. Film-A was made by dissolving PAN powder in DMF, Film-B was made by re-dissolving electrospun PAN fiber in DMF, and Film-C was processed from PAN /$ZnCl_2$ (weight ratio 95/5) solution in DMF. In all cases DMF was removed by evaporation in air at room temperature for one week.

2.2.2 Characterization

Viscosity of PAN/DMF solutions was measured on the Hakke RS150 rheometer (Karlsruhe, Germany) using a bob and cup arrangement at room

temperature (the inner diameter of the cup is 5.5 cm, the gap between the bob and cup is 0.5 cm). Surface tension was measured by the surface tensiomat (Fisher Scientific, Model 21, Pittsburg, PA) at room temperature.

Scanning Electron Microscopy (SEM) was done on gold sputter coated mats using LEO 1530 (Osaka, Japan) thermally assisted FEG scanning electron microscope. The SEM images were used for the fiber diameter determination. A JEM 2000EX (200 kV) (Tokyo, Japan) instrument was used for high resolution transmission electron microscopy (TEM). A Leica DMRX Optical Microscope (Leica Microsystems) equipped with a Sony Digital Photo Camera DKC-5000 was used for polarizing optical microscopy. The Raman spectra were collected on Holoprobe Research Raman microscope (Kaiser Optical Systems, Inc., Ann Arbor, MI) using 785 nm excitation wave length. Fourier transform infrared (FTIR) analysis of electrospun PAN and PAN/$ZnCl_2$ fiber mats was conducted on a Spectrum One FTIR spectrometer (PerkinElmer, Shelton, CT).

Wide angle X-Ray diffraction (WAXD) studies were conducted on a Rigaku 2D SAXS/WAXS diffraction system using a Rigaku R-AXIS IV^{++} detection system (Rigaku Micromax-007, 45 kV, 66 mA, The Woodlands, TX). The diffraction patterns were analyzed using Areamax V1.00 and MDI Jade 6.1 software. The crystal size of various samples was calculated using Scherrer equation:[8]

$$D_{hkl} = k\lambda / (B\cos\theta)$$

Where D_{hkl} is crystal size perpendicular to the hkl plane, k = 0.9, λ is wavelength of the radiation ($\lambda_{CuK\alpha}$ = 1.5418 Å), B is FWHM (full width at half maximum of the hkl diffraction), and θ is the position of diffraction peak.

High speed photographs were taken using a Photron CCD camera (Model: FASTCAM-X 1280 PSI) with a speed of 1000 frames per second (FPS). In order to obtain a sharp image on the micron-scale field of view, a pulsed Cu-vapor laser (Oxford Lasers, Shirley, MA), which emits green-yellow (510/578 nm) flash pulses with pulse duration of about 25 ns, was used. The schematic sketch of the setup for high speed photography is given in Figure 2.1. The photography region was a small region near the needle. For each electrospinning process, three regions as indicated by A, B, and C in Figure 2.1 were photographed by manually moving the camera along the fiber jet. The semi-angle of the Taylor cone for each electrospinning process was measured and the average value was reported based on five measurements.

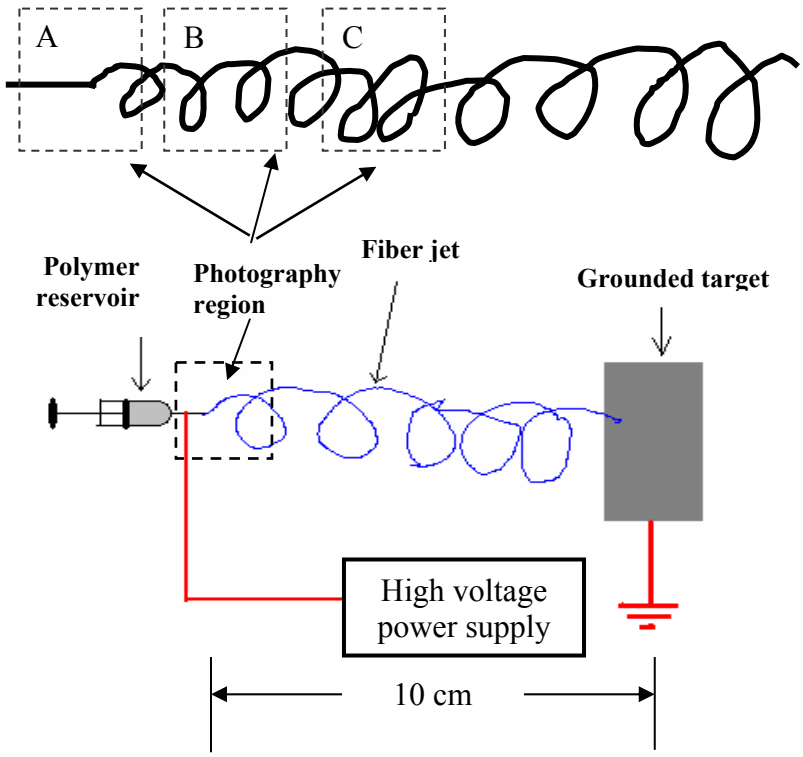

Figure 2.1. Schematic sketch of the electrospinning setup showing the high speed photography regions of (A) starting point of the jet, near the needle tip, (B) second electrospinning region along the jet, and (C) third electrospinning region along the jet (the regions of A, B, and C were obtained by manually moving the camera away from the needle tip).

2.3 Results and Discussion

2.3.1 Rheology

The viscosity data for PAN copolymer solutions (MW 100,000 g/mol) as a function of shear rate is plotted in Figure 2.2. Zero shear viscosity was determined at each concentration, and the specific viscosity η_{sp} was calculated using the following equation:

$$\eta_{sp} = (\eta_s - \eta_0)/\eta_0$$

where η_s and η_0 are the zero shear viscosities of solution and solvent, respectively. The specific viscosities for various molecular weight PANs are plotted as a function of concentration in Figure 2.3. η_{sp} scales as $C^{1.3}$ and $C^{4.4}$ for PAN of 100,000 g/mol molecular weight, as $C^{0.45}$, $C^{1.7}$, and $C^{3.6}$ for PAN of 250,000 g/mol molecular weight, and as $C^{0.68}$, $C^{2.1}$, and $C^{3.9}$ for PAN of 700,000 g/mol molecular weight. According to de Gennes's scaling concept, the polymer in a good solvent can be classified into four regimes with the following exponents: dilute ($\eta \sim C^1$), semidilute unentangled ($\eta \sim C^{1.25}$), semidilute entangled ($\eta \sim C^{4.8}$), and concentrated regime ($\eta \sim C^{3.6}$).[9] The entanglement concentration is the critical concentration between the semidilute unentangled and the semidilute entangled regime. The scaling relationship has also been experimentally studied. It has been reported that $\eta \sim C^{1.1\sim1.4}$ for semidilute unentangled [10] and $\eta \sim C^{4.25\sim4.5}$ for semidiluted entangled regimes.[11] In general, the scaling exponents vary depending on the polymer, polymer conformation, and the interaction between the polymer and the solvent. Factors such as branching[10] or solubility[12, 13] result in different exponents. In the present study, the PAN copolymer solutions of 100,000 g/mol molecular weight with $\eta_{sp} \sim C^{1.3}$ and $\eta_{sp} \sim C^{4.4}$ are in the semidilute unentangled and semidilute entangled regimes, respectively, and the PAN homopolymer solutions of 250,000 g/mol molecular weight with $\eta_{sp} \sim C^{0.45}$, $C^{1.7}$ and $C^{3.6}$ and of 700,000 g/mol

molecular weight with $\eta_{sp} \sim C^{0.68}$, $C^{2.1}$, and $C^{3.9}$ are in the dilute, semidilute unentangled, and semidilute entangled regimes, respectively. The entanglement concentrations for PAN of 100,000, 250,000, and 700,000 g/mol molecular weights are determined to be about 5.1, 3.1, and 1.5 wt%, respectively.

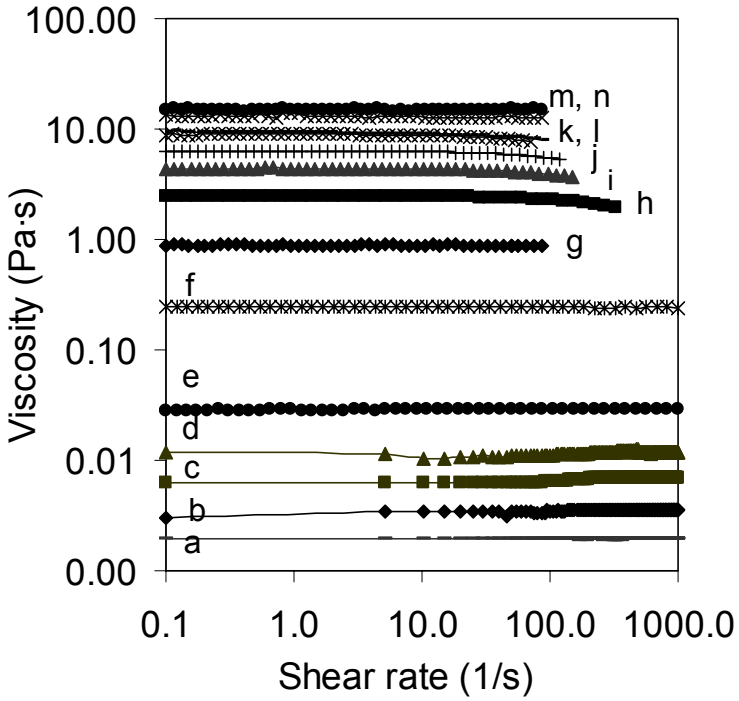

Figure 2.2. The viscosity of PAN copolymer solutions (MW 100,000 g/mol) as a function of shear rate at various concentrations of (a) 0.5 wt%, (b) 1.1 wt%, (c) 2.1 wt%, (d) 3.1 wt%, (e) 5.1 wt%, (f) 9.6 wt%, (g) 13.8 wt%, (h) 16.1 wt%, (i) 17.5 wt%, (j) 19.0 wt%, (k) 19.7 wt%, (l) 20.3 wt%, (m) 21.2 wt%, and (n) 22.1 wt%.

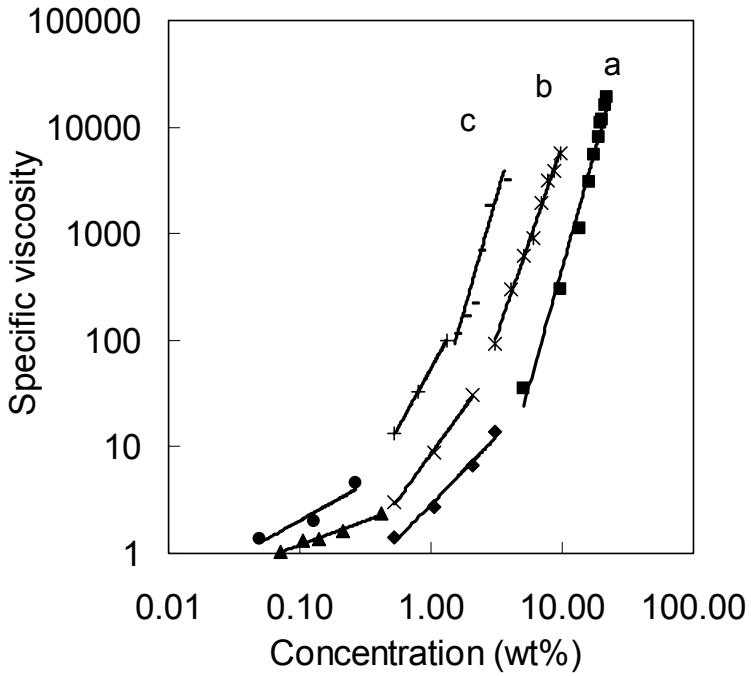

Figure 2.3. The specific viscosity as a function of concentration for (a) PAN copolymer of 100,000 g/mol molecular weight, (b) PAN homopolymer of 250,000 g/mol molecular weight, and (c) PAN homopolymer of 700,000 g/mol molecular weight.

2.3.2 Systematic study of electrospinning of PAN as a function of solution properties and processing factors

Average value of fiber diameter based on 40 measurements for each spinning condition for 100,000 g/mol molecular weight PAN are reported in Tables 2.1 to 2.3. The SEM images of electrospun PAN (100,000 g/mol) copolymer solutions in the concentration range of 0.5 to 21 wt% are given in Figure 2.4. At low concentration (0.5~3.1 wt%), nanoscopic to microscopic particles were obtained (typical size of 400 to 800 nm). Above the entanglement concentration (5.1 wt%), the beaded (30 to ~300 nm diameter) and bead-free fibers (~350 nm to 2.0 μm) were obtained (Tables 2.1 to 2.3, Figure 2.4). For all the three PANs, the continuous fibers were obtained above their entanglement concentrations. This is consistent with Long et al's work on the

electrospun poly(ethylene terephthalate-co-ethylene isophthalate) copolymer (PET-co-PEI).[10]

Table 2.1. Diameter of electrospun PAN copolymer (MW 100,000 g/mol) fiber at various polymer concentrations and voltages (the distance between the needle tip and the target is 10 cm and flow rate is 1 ml/hr).

C (wt%)	**Fiber diameter (nm)**				
	13 kV	16 kV	22 kV	25 kV	27 kV
5.1	50 ± 10	50 ± 10	50 ± 10	60 ± 10	80 ± 20
9.6	100 ± 10	80 ± 20	70 ± 10	100 ± 20	100 ± 20
13.8	160 ± 10	120 ± 20	150 ± 20	130 ± 30	130 ± 40
16.1	190 ± 20	230 ± 30	170 ± 40	240 ± 40	240 ± 40
17.5	**350 ± 20**	**400 ± 90**	**370 ± 40**	**380 ± 20**	**450 ± 80**
19.0	**450 ± 80**	**500 ± 120**	**590 ± 100**	**400 ± 60**	**600 ± 90**
19.7	**770 ± 60**	**800 ± 150**	**660 ± 40**	**760 ± 80**	**800 ± 130**
20.3	**900 ± 130**	**1200 ± 60**	**1100 ± 150**	**1000 ± 120**	**1200 ± 110**

* bead-free fibers are in bold

Table 2.2. Diameter of electrospun PAN copolymer (MW 100,000 g/mol) fiber at various flow rates and solution concentrations (voltage is 22 kV and the distance between the needle tip and the target is 10 cm).

Flow rate (ml/h)	**Fiber diameter (nm)**							
	5.1 wt%	9.6 wt%	13.8 wt%	16.1 wt%	**17.5 wt%**	**19.0 wt%**	**19.7 wt%**	**20.3 wt%**
0.5	30 ± 20	50 ± 20	80 ± 20	150 ± 30	200 ± 40	**350 ± 70**	**400 ± 60**	**600 ± 90**
1	50 ± 10	70 ± 10	150 ± 20	170 ± 40	**370 ± 40**	**590 ± 100**	**660 ± 40**	**1100 ± 150**
4	150 ± 40	**400 ± 49**	**460 ± 60**	**500 ± 80**	**700 ± 60**	**800 ± 90**	**900 ± 70**	**1350 ± 110**
6	300 ± 60	**900 ± 70**	**1000 ± 80**	**1200 ± 150**	**1500 ± 100**	**1650 ± 110**	**1800 ± 110**	**2000 ± 110**

* bead-free fibers are in bold

Table 2.3. Diameter of electrospun PAN copolymer (MW 100,000 g/mol) fiber at various electric field (E_d) (electric field varied by changing distance) and solution concentrations (flow rate 1 ml/hr).

Electric field(E_d) (V/cm)	**Fiber diameter (nm)**							
	5.1 wt%	9.6 wt%	13.8 wt%	16.1 wt%	**17.5 wt%**	**19.0 wt%**	**19.7 wt%**	**20.3 wt%**
4400	30 ± 10	60 ± 20	90 ± 20	120 ± 20	300 ± 60	**400 ± 90**	**490 ± 80**	**700 ± 100**
2200	50 ± 10	70 ± 10	150 ± 20	170 ± 40	**370 ± 40**	**590 ± 100**	**660 ± 40**	**1100 ± 150**
1467	60 ± 20	80 ± 20	120 ± 30	280 ± 50	**570 ± 70**	**650 ± 80**	**800 ± 90**	**1100 ± 100**
1100	70 ± 20	100 ± 20	200 ± 20	**380 ± 60**	**700 ± 100**	**800 ± 100**	**940 ± 80**	**1200 ± 130**

* bead-free fibers are in bold

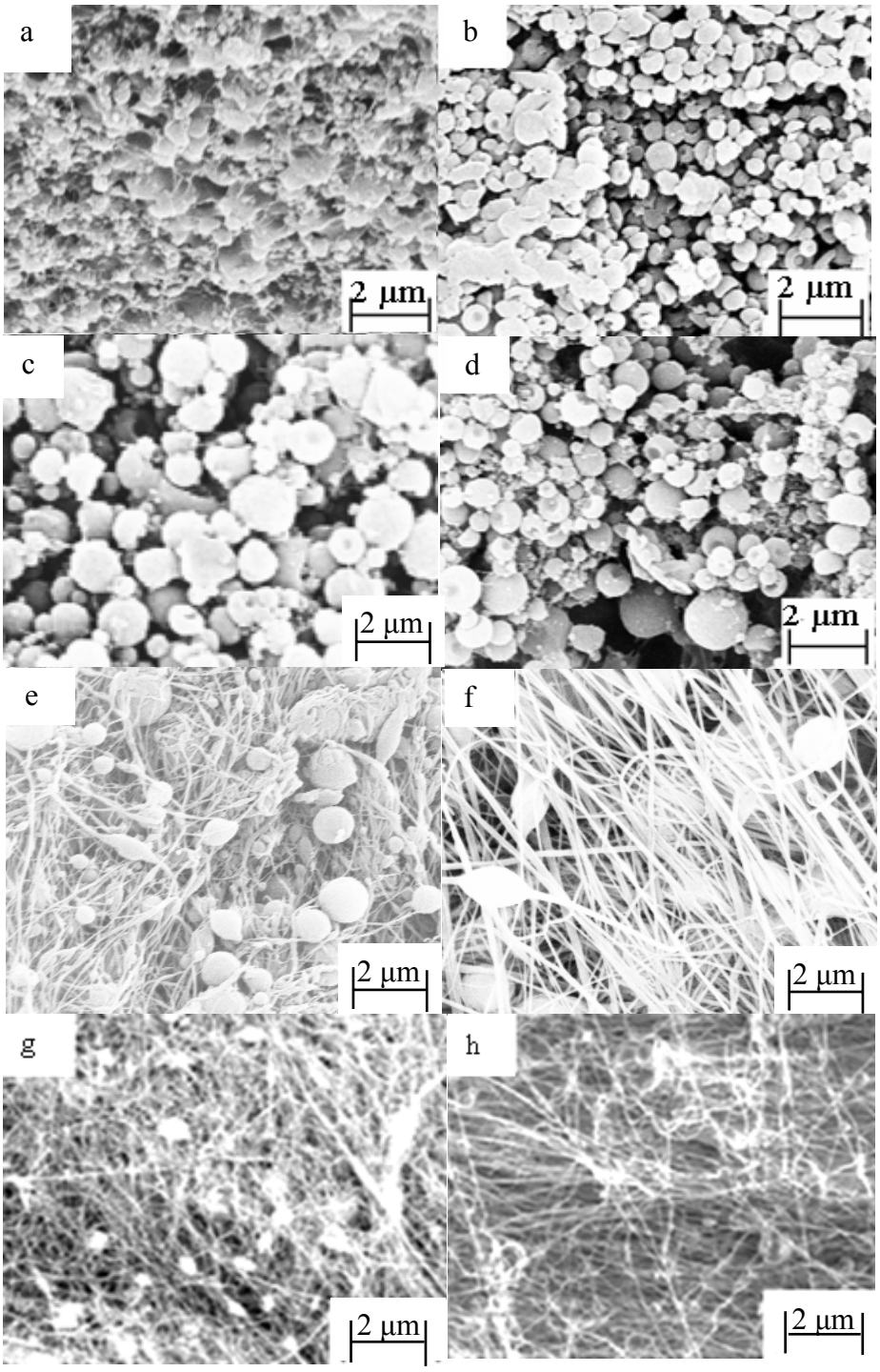

Figure 2.4. Scanning electron micrographs of electrospun PAN copolymer fibers (MW 100,000 g/mol) at various concentrations of (a) 0.5 wt%, (b) 1.1 wt%, (c) 2.1 wt%, (d) 3.1 wt%, (e) 5.1 wt%, (f) 9.6 wt%, (g) 13.8 wt%, (h) 16.1 wt%, (i) 17.5 wt%, (j) 19.0 wt%, (k) 19.7 wt%, and (l) 20.3 wt % (voltage is 22 kV, flow rate is 1ml/hr, the distance between the needle tip and the target is 10 cm).

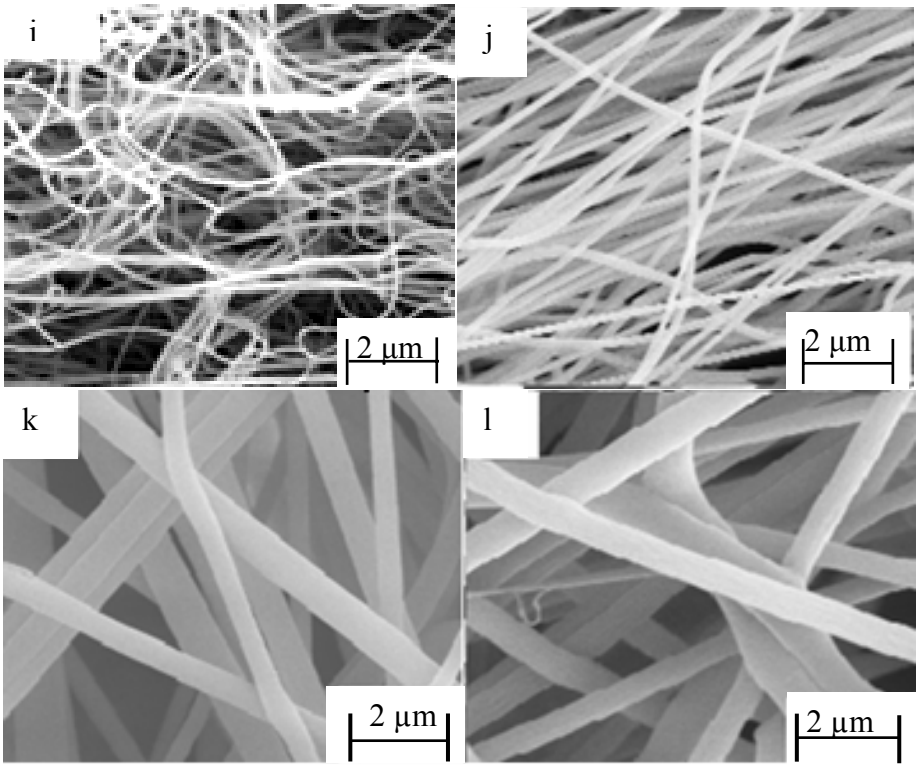

Figure 2.4. Continued.

In current work, the fiber diameter exhibits two distinct power law dependences on the polymer concentration (C) in the semidilute entangled regime (Figure 2.5). The fiber diameter scales with concentration as $C^{1.2}$ and $C^{7.5}$ for PAN of 100,000 g/mol molecular weight, as $C^{0.88}$ and $C^{3.5}$ for PAN of 250,000 g/mol molecular weight, and as $C^{0.99}$ and $C^{2.5}$ for PAN of 700,000 g/mol molecular weight. However for a given polymer system, only one power law has been reported in the literature. The diameter scaled as $C^{0.5}$ for poly(ethylene oxide) (PEO),[14] as $C^{3.0}$ for PET-co-PEI[10] and poly(urethane) (PU),[15] as $C^{3.3}$ for fibrinogen,[16] as $C^{2.6}$ for polyamide 6 (PA-6),[17] as $C^{3.1}$ for poly(methyl methacrylate)(PMMA)[11] (Table 2.4). However for poly(vinyl pyrrolidone) (PVP) diameter scaled as $C^{1.8}$ and with further increase in the concentration an upturn in the diameter was observed,[18] suggesting a second power law with the significantly higher exponent of $C^{7.0}$.

During electrospinning process, a single jet ejecting from the Taylor cone can possibly split or break up into subjets or droplets if the polymer chain entanglement is not strong enough. The subjets most likely result in beaded fibers. During electrospinning of higher concentration solutions, the jet would not split due to the sufficient chain entanglement, and this single jet gets to target to form larger diameter fibers. Therefore, the different chain entanglement densities ultimately determine whether the fiber forms from a subjet or a single jet, resulting in different fiber diameter dependence on the solution concentration.

The two PAN homopolymers (molecular weight 250,000 and 700,000 g/mol), have very comparable fiber diameter dependence on the concentration, while the PAN copolymer (molecular weight 100,000 g/mole) exhibits a much stronger diameter dependence on concentration in the high concentration range. This study does not answer the question, whether the differences in the diameter dependence are a result of the use of copolymer in the low molecular weight PAN, or these differences are simply a result of differences in molecular weight.

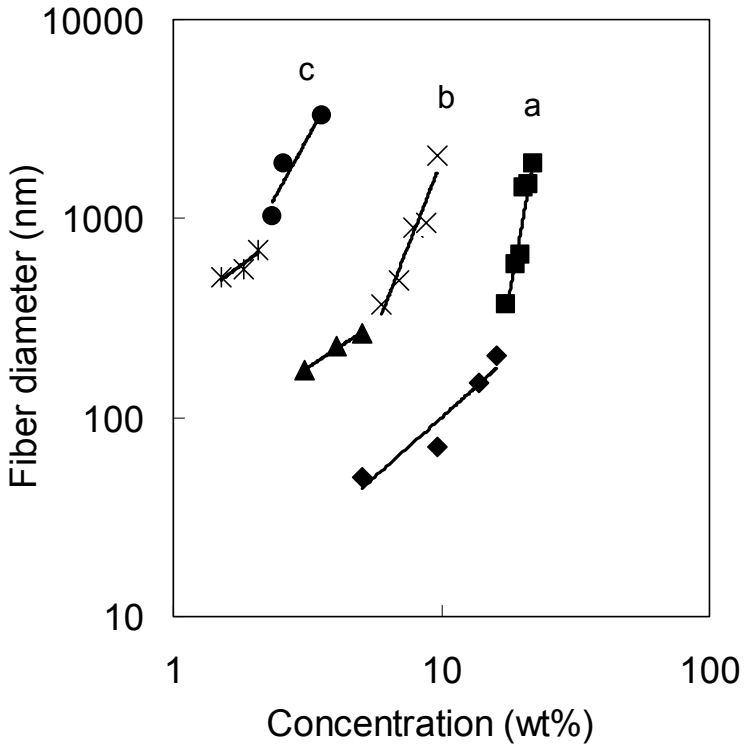

Figure 2.5. The fiber diameter as a function of the concentration for (a) PAN copolymer of 100,000 g/mol molecular weight, (b) PAN homopolymer of 250,000 g/mol molecular weight, and (c) PAN homopolymer of 700,000 g/mol molecular weight (the distance between the needle tip and the target is 10 cm, flow rate 1 ml/hr, and voltage is 22 kV).

Table 2.4. Summary of the power law relationship between the fiber diameter and the concentration reported in the literature and in this work.

Polymer	Exponent a ($d \sim C^a$)
PEO[14]	0.5
PET-co-PEI[10]	3.0
PU[15]	3.0
Fibrinogen[16]	3.3
PA-6[17]	2.6
PMMA (M_w 365,700 g/mol)[11]	3.1
PVP[18]	1.8, 7.0
PAN (100,000 g/mol)*	1.2, 7.5
PAN (250,000 g/mol)*	0.88, 3.5
PAN (700,000 g/mol)*	0.99, 2.5

* Data from this work.

The electric field (E_d) was varied by changing the distance (5 to 20 cm) between the needle tip and the target, while keeping the voltage constant at 22 kV. The fiber diameter (PAN MW 100,000 g/mol) as a function of E_d is given in Figure 2.6. For low concentrations and at high electric field, the diameter is as low as 30 nm, while at high concentration and at low electric field, the diameters above 1 μm have been observed. For all the concentrations at a given flow rate, the diameter decreased with increasing the electric field. The electric field (E_v) was also varied by increasing voltage from 13 kV to 27 kV, while keeping the distance constant at 10 cm. The fiber diameter is plotted as a function of E_V in Figure 2.7. Contrary to Figure 2.6, the fiber diameter doesn't exhibit significant dependence on E_V. This observation is consistent with the electrospinning of polysulfone [19] and nylon.[20] It was observed that the fiber diameter of polysulfone showed a slight decrease from 344 ± 51 nm to 323 ± 22nm when voltage was changed from 10 kV to 20 kV at a distance of 10 cm.[19] However,

this change in diameter was within experimental error and therefore can be ignored. The fiber diameter of electrospun nylon also did not show monotonic decrease with increasing voltage.[20] Increase in voltage does not have a significant effect on the diameter, while change in the distance at constant voltage affects the fiber diameter even though the electric field values (E_d and E_V) are the same. Under the same electric field (E_d and E_V), the electric field distribution may be different. Current was also observed to be different in the electrospinning of poly (ethylene oxide) (PEO) even though the electric fields, E_d and E_V, were equal.[21] The difference in electric field distribution and current may be responsible for different diameter dependence on E_d and E_V.

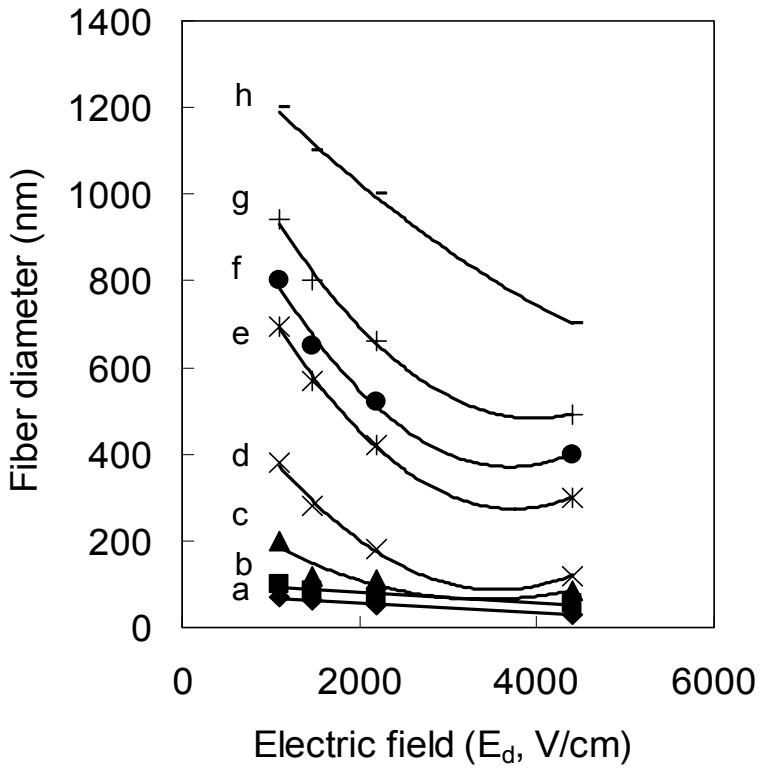

Figure 2.6. The fiber diameter as a function of electric field (E_d) for PAN copolymer solutions at various concentrations of (a) 5.1 wt%, (b) 9.6 wt%, (c) 13.8 wt%, (d) 16.1 wt%, (e) 17.5 wt%, (f) 19.0 wt%, (g) 19.7 wt%, and (h) 20.3 wt% (PAN copolymer, MW 100,000 g/mol, voltage is 22 kV, and flow rate is 1 ml/hr).

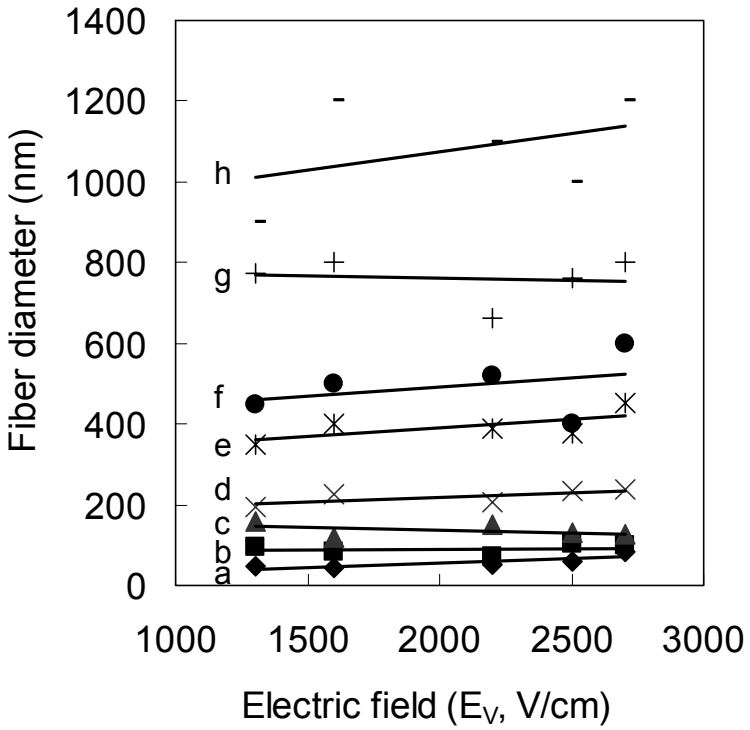

Figure 2.7. The fiber diameter as a function of electric field (E_V) for PAN copolymer solutions at various concentrations of (a) 5.1 wt%, (b) 9.6 wt%, (c) 13.8 wt%, (d) 16.1 wt%, (e) 17.5 wt%, (f) 19.0 wt%, (g) 19.7 wt%, and (h) 20.3 wt% (PAN MW 100,000 g/mol, the distance between the needle tip and the target is 10 cm, flow rate is 1 ml/hr).

The fiber diameter (d) as a function of flow rate (Q) for various concentrations is plotted in Figure 2.8. Fiber diameter increases with flow rate. At low concentrations, diameter scales with $Q^{1.2}$. Diameter dependence on concentration decreases with increasing concentration and at the highest concentration, diameter scales as $Q^{0.4}$ (Figure 2.9).

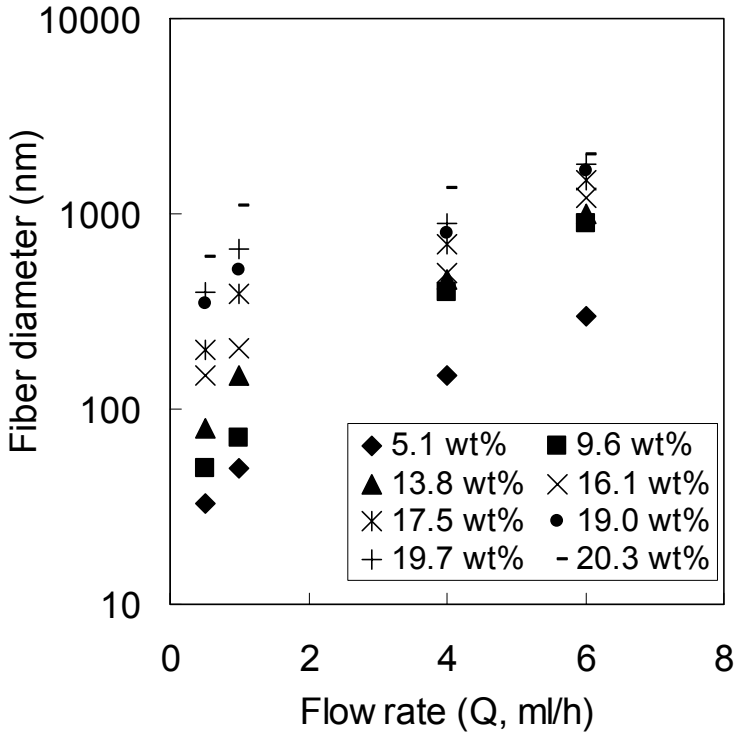

Figure 2.8. The fiber diameter as a function of flow rate for PAN copolymer solutions with various concentrations (PAN MW 100,000 g/mol, the distance between the needle tip and the target is 10 cm, and voltage is 22 kV).

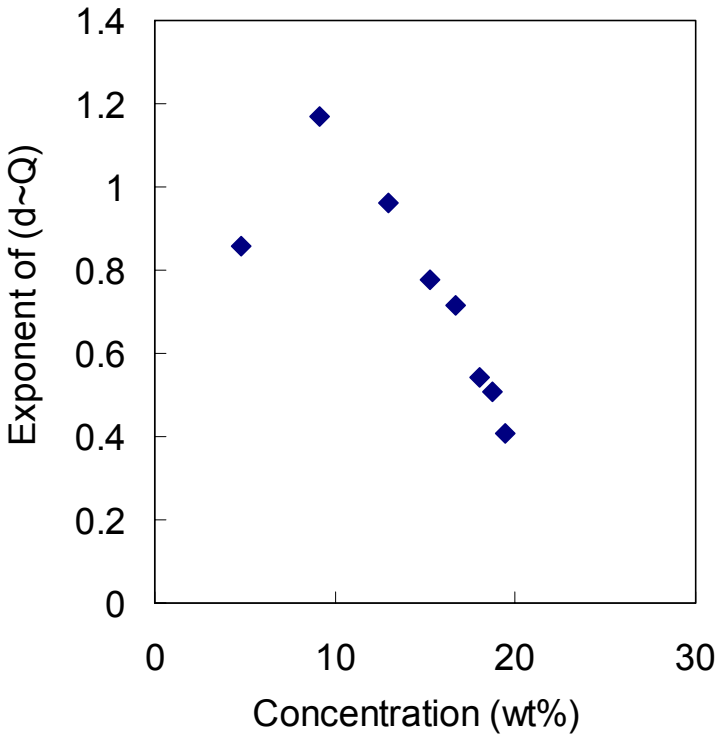

Figure 2.9. The exponent of the fiber diameter vs. flow rate as a function of concentration (PAN copolymer, MW 100,000 g/mol, the distance between the needle tip and the target is 10 cm, and voltage is 22 kV).

2.3.3 Electrospun PAN fibers processed from different solvents

The effects of solvent properties on fiber diameter and morphology were studied by electrospinning PAN in three different solvents, DMF, DMSO, and nitromethane/water (volume ratio of 94/6) [22] mixture. Both DMF and DMSO are good solvents for PAN and result in transparent solutions. PAN can also be dissolved in nitromethane/water (94/6) mixture but the solution appeared cloudy. It should be noted that both nitromethane and water are non solvents for PAN, however, their mixture (94/6) can dissolve PAN. To explain this phenomenon, the distance between the solvent and the solute (R_{ij}) is calculated, which can be used to characterize the solubility of polymer in solvent. The lower R_{ij}^2 value indicates better solubility of polymer in solvent. Based on the three dimensional solubility parameters of polymer and solvents, R_{ij}^2 can be calculated by using the following equation:[23]

$$R_{ij}^2 = 4(\delta_{d1} - \delta_{d2})^2 + (\delta_{p1} - \delta_{p2})^2 + (\delta_{h1} - \delta_{h2})^2$$

where δ_{d1}, δ_{p1}, and δ_{h1} are three dimensional solubility parameters for solvent and δ_{d2}, δ_{p2}, and δ_{h2} for polymer. When using solvent mixture, the three dimensional solubility parameters can be calculated by using the following equation:[23]

$$\delta_{mixture} = \sum_i \delta_i \varphi_i$$

where δ_i and Φ_i are the solubility parameter and volume ratio for each component respectively.

The δ_d, $\delta_{p,}$ and δ_h values for PAN and solvents are listed in Table 2.5. The low R_{ij}^2 value for PAN/DMF is consistent with good solubility of PAN in DMF. The R_{ij}^2 value of PAN/water is very high, indicating the poor solubility of PAN in water. Though R_{ij}^2 value of PAN/nitroemthane/water is comparable to that of PAN/DMF, nitromethane still cannot dissolve PAN. The R_{ij}^2 value of PAN/(nitromethane/water) solution was plotted as a function of nitromethane volume ratio in Figure 2.10. It shows that with increasing volume ratio of nitromethane, the R_{ij}^2 value first decreases rapidly, then reaches the lowest point when nitromethane volume ratio is between 94 and 96, with further increasing nitromethane ratio, R_{ij}^2 increases. The low R_{ij}^2 value in this region indicates the relatively better solubility of PAN in nitromethane/water mixture.

Table 2.5. Solubility parameters and R_{ij}^2 values of PAN and solvents

	$\delta_d(MPa)^{1/2}$	$\delta_P(MPa)^{1/2}$	$\delta_h(MPa)^{1/2}$	R_{ij}^2 (MPa)
PAN[23]	18.2	16.2	6.8	
DMF[24]	17.4	13.7	11.3	29.4
Nitromethane[24]	15.8	18.8	5.1	32.9
Water[24]	15.6	16.0	42.3	1291.1

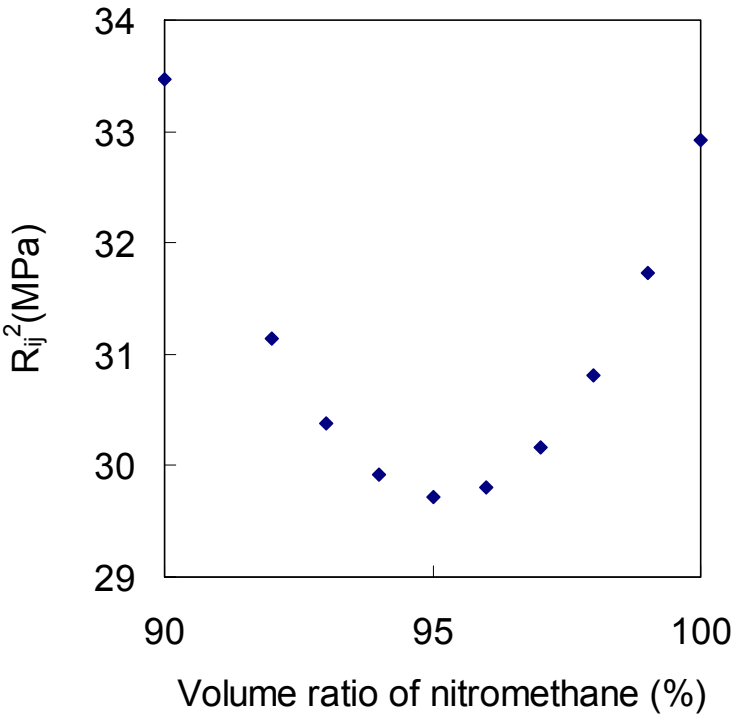

Figure 2.10. R_{ij}^2 of PAN in nitromethane/water as a function of volume ratio of nitromethane.

Figure 2.11 gives SEM images of the particles and fibers electrospun from PAN/(nitromethane/water) solution. At low solution concentration, the irregular cup structures with typical dimensions of 800 nm were obtained. Compared to PMMA cups with wall thickness of about 200 nm,[25] PAN cups have much thinner walls with thickness of about 20 nm (Figure 2.12). With increasing solution concentration, porous fibers were obtained with pore size ranging from 30 to 60 nm. The pores appear to be mostly on the surface and through the cross section (Figure 2.13). The long dimension of these pores was aligned along the fiber axis, which may be caused by the jet stretching during electrospinning.

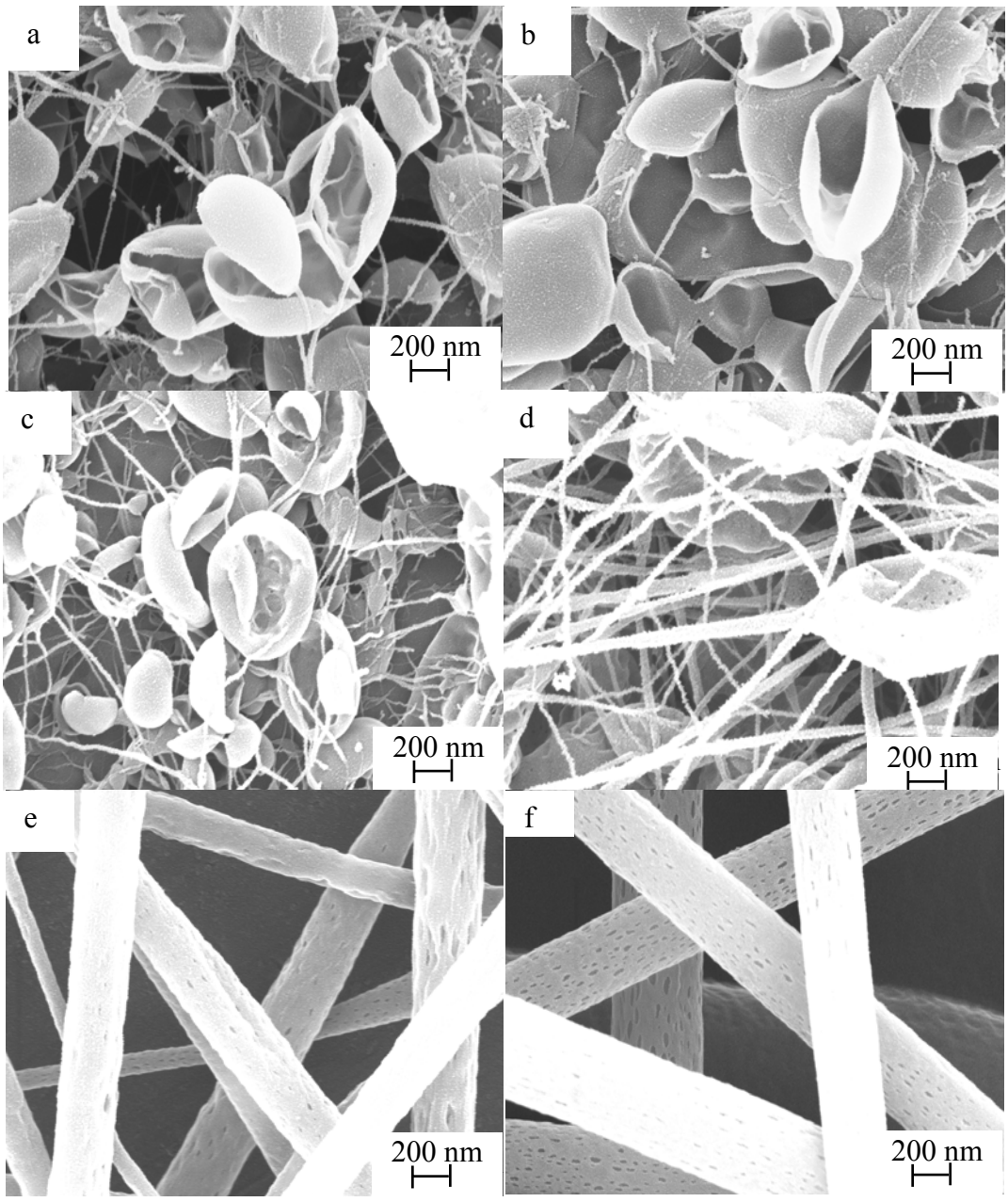

Figure 2.11. Scanning electron micrographs of PAN cups and fibers electrospun from PAN/(nitromethane/ water)(94/6) solutions at following polymer concentrations of (a) 0.19 wt% PAN, (b) 0.38 wt% PAN, (c) 0.75 wt% PAN, (d) 1.5 wt% PAN, (e) 3 wt% PAN, and (f) 6 wt% PAN (PAN copolymer, MW 100,000 g/mol, flow rate is 1 ml/hr, the distance between the needle tip and the target is 10 cm, and voltage is 22 kV).

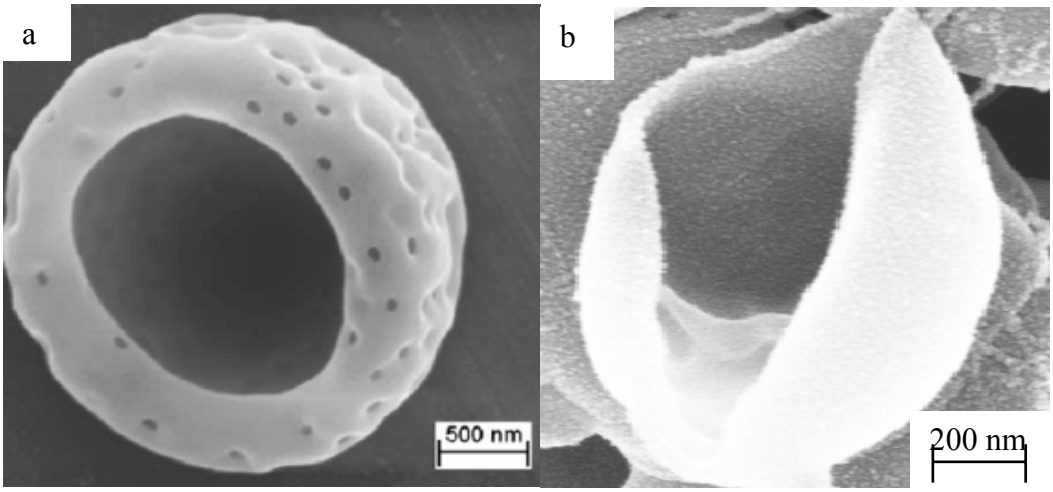

Figure 2.12. Scanning electron micrographs of (a) PMMA cup (From ref. 25.) and (b) PAN cup (PAN copolymer with MW 100,000 g/mol, 0.38 wt% PAN/(nitromethane/water) solution, flow rate is 1 ml/hr, the distance between the needle tip and the target is 10 cm, and voltage is 22 kV).

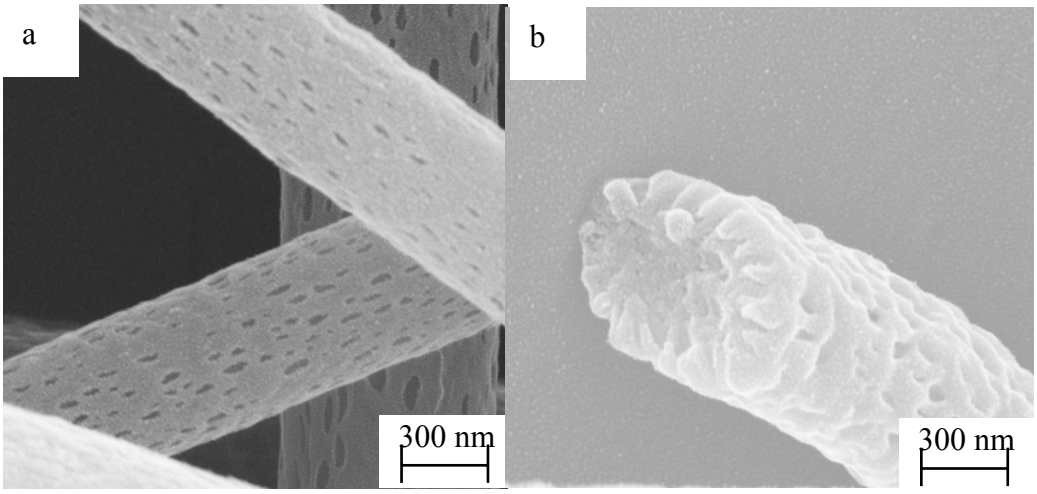

Figure 2.13. Scanning electron micrographs of (a) surface and (b) cross section of porous PAN fibers (PAN copolymer with MW 100,000 g/mol, 6 wt% PAN in (nitromethane/water) solution, flow rate is 1 ml/hr, the distance between the needle tip and the target is 10 cm, and voltage is 22 kV).

With same concentration solutions (6 wt%), the porous fibers electrospun from PAN/(nitromethane/water) have a diameter of about 600 nm, while the solid fibers electrospun from PAN/DMF solution have a diameter of about 60 nm. It has been widely reported that the solution viscosity[10] or dielectric constant of solvent[26] play an important role on fiber diameter, however, these factors are not responsible for the diameter difference in this study. The viscosity of PAN/(nitromethane/water) solution could not be measured due to the fast evaporation rate of nitromethane. However, considering the poor solubility of PAN in nitromethane/water, it is expected that PAN/(nitromethane/water) should have lower viscosity than PAN/DMF solution, which is expected to result in smaller diameter when electrospun from PAN/(nitromethane/water) solution. Secondly, both nitromethane and water have higher dielectric constants than DMF (the dielectric constants of DMF,[25] nitromethane,[25] and water,[27] are 38, 39, and 78, respectively). High dielectric constant increases the charge density carried by the jet. Therefore smaller diameter fibers are expected when nitromethane/water was used for electrospinning.

Apart from the effects of viscosity and dielectric constant on the fiber diameter, solvent evaporation rate was also considered for the diameter difference. When electrospinning PAN/(nitromethane/water) solution, nitromethane evaporates fast (the evaporation rate of nitromethane is 1.4 (butyl acetate = 1)),[25] and the jet solidifies at the early stage during its travel from the needle tip to the target. Once the jet solidifies, its elongation is restricted, resulting in relatively larger diameter fibers. However, when electrospinning PAN/DMF solution, the slow evaporation of DMF (the evaporation rate of DMF is 0.2 (butyl acetate = 1))[25] allows the stretching of the fiber jet through the whole travel process, resulting in small fiber diameter. Large diameter porous fibers were also reported in the literature when using volatile solvent

for electrospinning. The porous poly-L-lactide (PLLA) fibers [28] with diameter of 1 μm were observed when electrospun from dichloromethane. The porous poly (styrene) (PS) fibers[29] with diameter of 10 μm were also reported when electrospun from THF solvent.

2.3.4 Electrospinning of small diameter bead free PAN nanofibers

When electrospinning polymer solution at low concentration, beads or beads-on-string generally occur.[30, 31] Bead formation is due to jet instability driven by the surface tension. [32 , 33] When electrospinning high concentration solution, the viscoelastic force is sufficient to resist electrostatic repulsive force and prevents jet breakup, resulting in bead free fibers. It was reported that fluid elasticity plays an important role in fiber formation.[34] The high elasticity can suppress jet instability, resulting in bead free fibers. The bead formation can also be prevented by increasing net charge density (charge/volume) [35] carried by the jet, which is achieved by using high dielectric constant solvent[36] or by the addition of salt.[35]

The drawability of the polymer solutions and melts is governed by the viscosity (η) to the surface tension (γ) ratio.[37] The values of η, γ, and η/γ for PAN/DMF (MW 100,000 g/mol) solutions with various concentrations are listed in Table 2.6. It shows that with increasing concentration, viscosity increases while surface tension does not change significantly, resulting in high η/γ values. The high η/γ value is associated with bead free fiber formation. Use of low surface tension solvents resulting in comparable viscosity provides better drawability and hence bead free smaller diameter fibers are expected at low concentration. High polymer concentration results in high viscosity producing bead free fibers. Therefore, the

elimination of beads with increasing concentration is commonly reported in electrospinning.[10, 17, 35]

Table 2.6. Drawability of PAN copolymer (MW 100,000 g/mol) at various concentrations

Concentration C (wt%)	**Zero shear viscosity η_0 (Pa· s)**	**Surface tension γ (N/m)**	**Drawability η_0/γ (s/m)**
0.5	0.002	0.037	0.05
3.1	0.012	0.037	0.32
13.8	0.88	0.039	23
19.0	6.34	0.039	163

Increase in bead frequency was reported with increasing electrospinning voltage in poly (carbonate),[38] in poly(ethylene oxide) (PEO),[14] and in hydroxypropyl cellulose (HPC).[39] On the other hand, a decrease in bead frequency was reported with increasing electrospinning voltage in poly(hydroxybutyrate-co-valerate) (PHBV)[40] and in poly(ε-caprolactone).[41] In the current study, no significant effect of electrospinning voltage was observed on bead frequency (Figure 2.14).

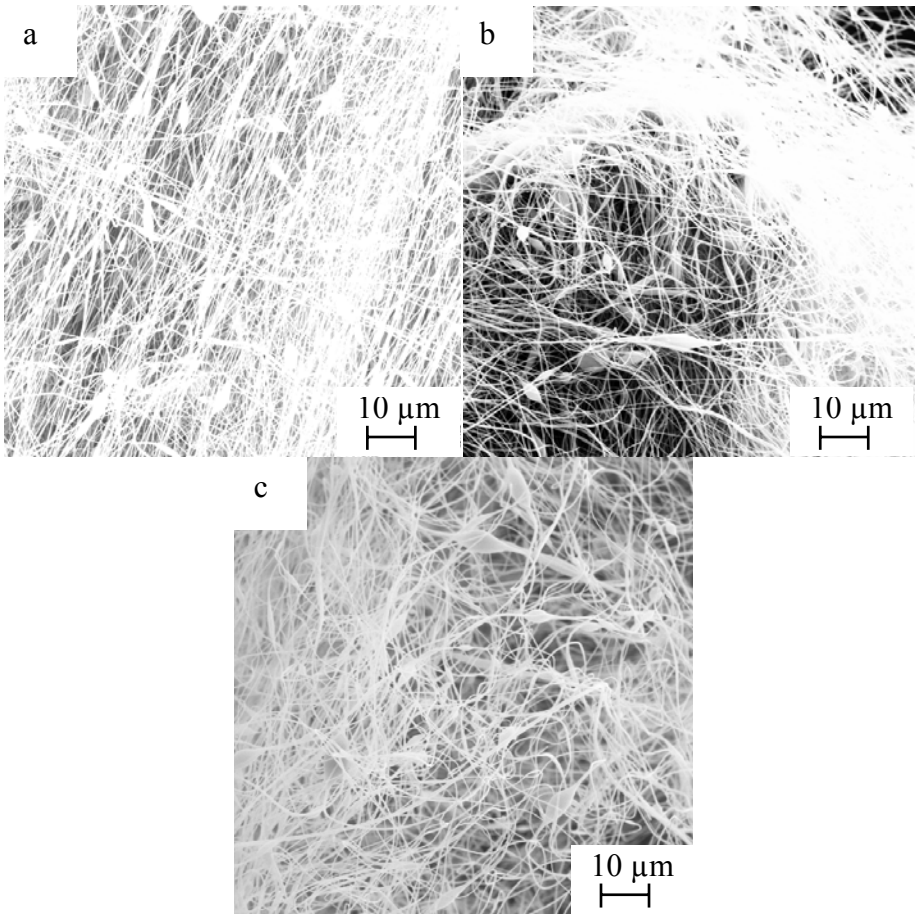

Figure 2.14. Scanning electron micrographs of PAN fibers electrospun at voltage of (a) 10 kV, (b) 22 kV, and (c) 27 kV (PAN copolymer, MW 100,000 g/mol, 9.6 wt% PAN/DMF solution, flow rate is 1 ml/hr, the distance between the needle tip and the target is 10 cm).

The solvent with high dielectric constant can increase the net charge density carried by the fiber jet and thus prevent bead formation. It was reported that the beads in the electrospun poly (ε-caprolactone) (PCL) fibers greatly decreased when DMF (dielectric constant is 37) was added into the methylene choloride (dielectric constant is 9).[42] Poly (styrene) (PS) solution had better spinnability when high dielectric constant solvents such as DMF or THF were used.[43] In this study, DMSO was used to dissolve PAN for electrospinning fibers as it has higher dielectric constant than DMF (The dielectric constants for DMSO and DMF are 47 and 37, respectively).[44]

Figure 2.15 gives the SEM images of the fiber mats electrospun from PAN/DMF and PAN/DMSO solutions keeping other electrospinning conditions constant. It shows that PAN fibers electrospun from DMSO have fewer beads with larger diameter than the fibers electrospun from DMF. The decrease in bead concentration may be attributed to the high dielectric constant of DMSO. During the electrospinning process, the slow evaporation of DMSO causes the wet fibers to fuse together effectively resulting in larger diameter fiber. The fusion of fibers was also observed when high boiling point solvent-m-cresol, was used to electrospin polyamide-6.[17]

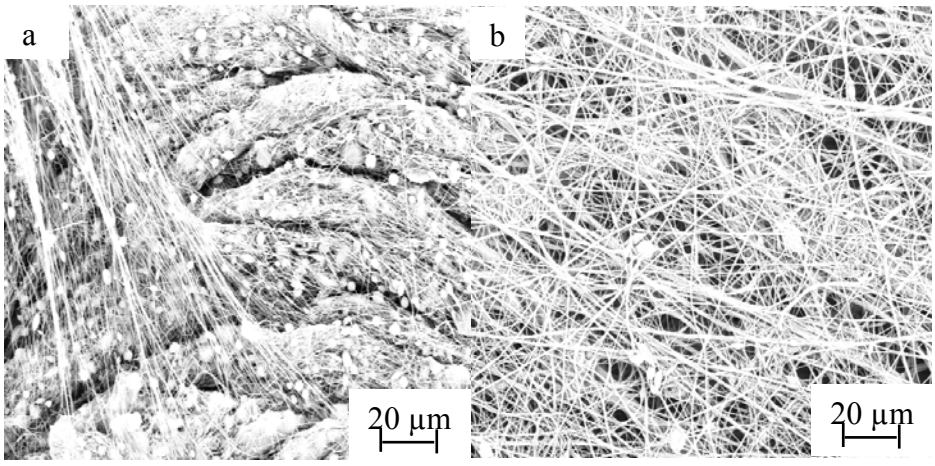

Figure 2.15. Scanning electron micrographs of PAN fibers electrospun with solvent of (a) DMF and (b) DMSO (PAN copolymer, MW 100,000 g/mol, concentration is 9.6 wt%, flow rate is 1 ml/hr, the distance between the needle tip and the target is 10 cm, and voltage is 22 kV).

The addition of salt in polymer solution can greatly decrease the beads in the fibers.[45, 46] In this study, $ZnCl_2$ was added into PAN solutions. 1 and 5 wt% $ZnCl_2$ with respect to PAN can be completely dissolved in PAN/DMF solution, but became insoluble at higher $ZnCl_2$ concentrations. Therefore PAN/DMF solutions with 1 and 5 wt% $ZnCl_2$ were used for electrospinning while keeping other electrospinning conditions constant. Figure 2.16 gives the SEM images of PAN fiber mats

electrospun from salt containing PAN/DMF solutions. With the addition of $ZnCl_2$, the beads decreased significantly without any influence on fiber diameter. The addition of salt increases the net charge density carried by the jet,[3535] thus enhancing the electrical repulsive force and electrostatic attractive force. This results in fiber stretching, preventing the bead formation.

When electrospinning PAN/$ZnCl_2$ solution at low concentration, ordered clustered structures were observed as shown in Figure 2.17. At high concentration, ordered structures disappeared and the fibers were found to have random orientation (Figure 2.16 (e), (f), (g), (h)). The possible mechanism of ordered structure formation is sketched in Figure 2.18.[47] With addition of salt, the charge density carried by the jet increases, resulting in stronger electrostatic repulsive force between the adjacent fibers. This repulsive force can move the small diameter fibers, resulting in arrangement of these fibers into ordered structure. However, this repulsive force is not strong enough to move the large diameter fibers, resulting in random structure.

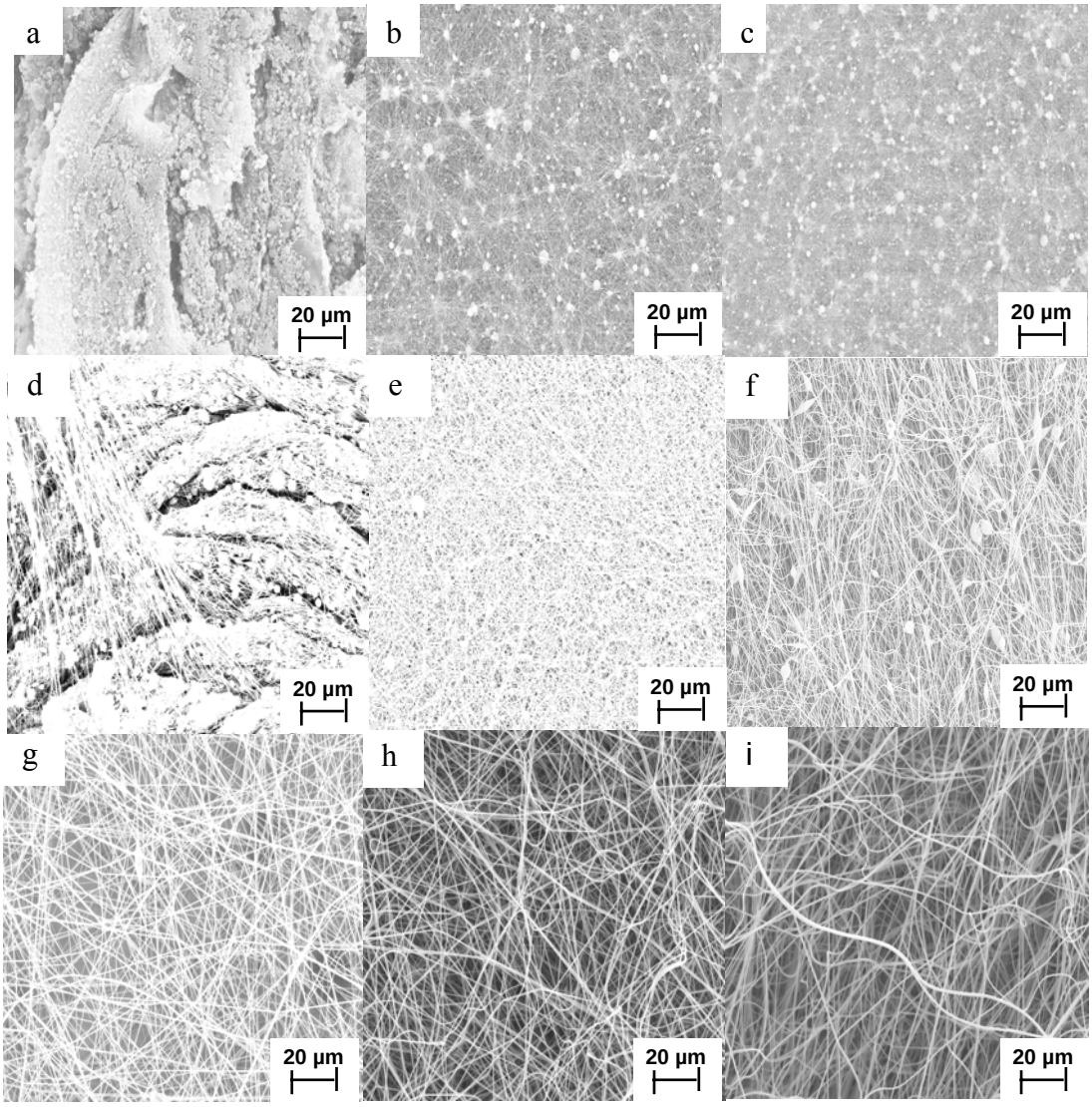

Figure 2.16. Scanning electron micrographs of fiber mats electrospun from salt containing PAN/DMF solutions with concentration of (a) 5.1 wt PAN, (b) 5.1 wt% PAN/$ZnCl_2$ (99/1), (c) 5.1 wt% PAN/$ZnCl_2$ (99/5), (d) 9.6 wt% PAN, (e) 9.6 wt% PAN $ZnCl_2$ (99/1), (f) 9.6 wt% PAN $ZnCl_2$ (99/5), (g) 16.1 wt% PAN, (h) 16.1 wt% PAN $ZnCl_2$ (99/1), and (i) 16.1 wt% PAN $ZnCl_2$ (99/5) (PAN copolymer, MW 100,000 g/mol, flow rate is 1 ml/hr, the distance between the needle tip and the target is 10 cm, and voltage is 22 kV).

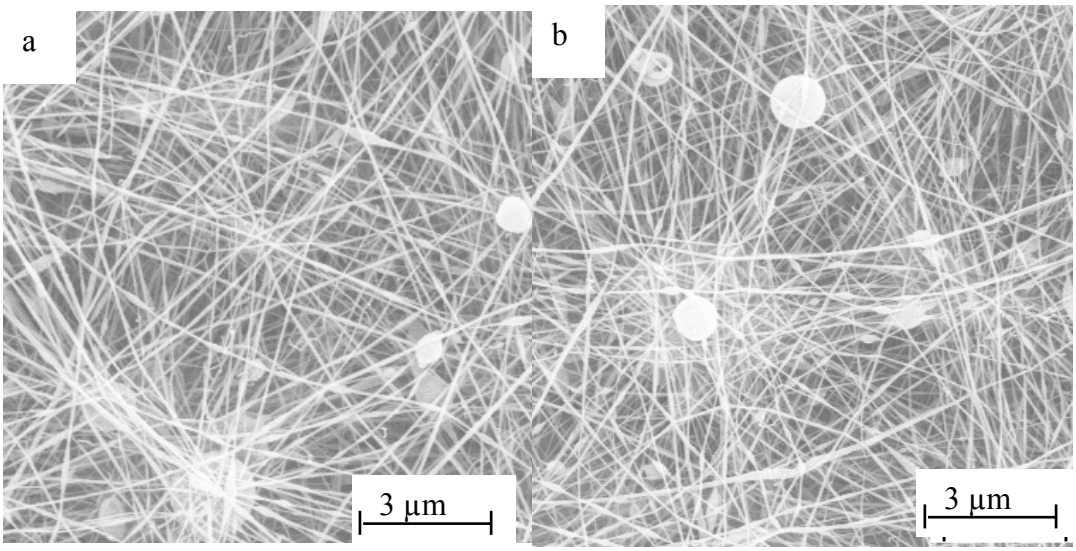

Figure 2.17. Scanning electron micrographs of ordered structure of (a) 5.1 wt% PAN/$ZnCl_2$ (99/1) and (b) 5.1 wt% PAN/$ZnCl_2$ (95/5)(PAN copolymer, MW 100,000 g/mol, DMF is solvent, flow rate is 1 ml/hr, the distance between the needle tip and the target is 10 cm, and voltage is 22 kV).

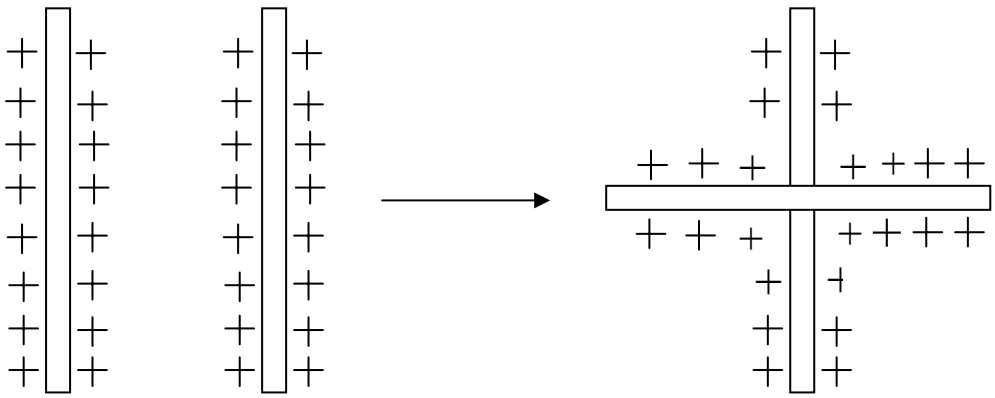

Figure 2.18. Schematic sketch of the formation of ordered structure. (From ref. 47.)

The inhomogenity and impurity in the polymer solution cause the flow instability during electrospinning, resulting in beaded fibers. Even though this issue has not been directly addressed in the literature, it has been reported that more beads and irregular structures were observed in electrospun poly(vinyl alcohol) PVA/silica fibers than in pure PVA fibers,[48] indicating that the inhomogenity in the solution may cause bead formation. The impurities in the solution would act as defect sites in the jet during electrospinning. The jet can easily break up at these defect sites while stretching, resulting in beaded fibers. In order to remove impurities and make homogeneous solution, PAN/$ZnCl_2$/DMF solutions were homogenized and filtered before electrospinning. Meanwhile, use of large diameter needle can make solution flow smoothly, which also prevents bead formation. Figure 2.19 shows SEM images of PAN fiber mats processed through addition of salt, homogenization, filtration, and use of large diameter needle.

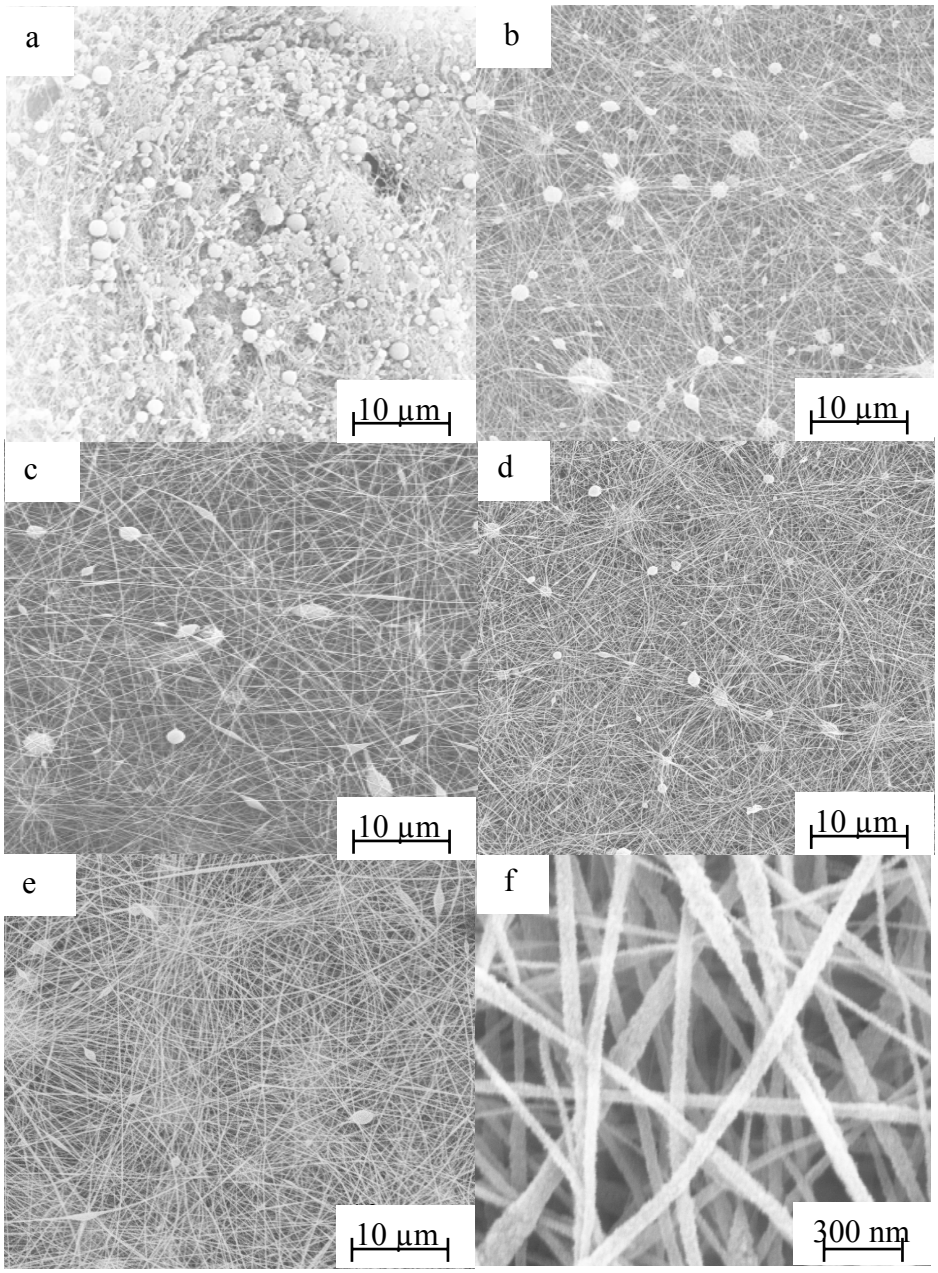

Figure 2.19. Scanning electron micrographs of PAN fibers (a) PAN(18 gauge needle), (b) PAN/$ZnCl_2$ (99/1) (18 gauge needle), (c) Homogenized PAN/$ZnCl_2$ (99/1) (18 gauge needle) (d) Filtered & homogenized PAN/$ZnCl_2$ (99/1) (18 gauge needle); (e) Filtered, homogenized, and processed by 14 gauge needle; (f) High magnification of (e) (PAN copolymer, MW 100,000 g/mol, 5.1 wt% PAN/DMF solution, flow rate is 1 ml/hr, the distance between the needle tip and the target is 10 cm, and voltage is 22 kV).

2.3.5 FTIR of electrospun PAN and PAN/$ZnCl_2$ fiber mats

2.3.5.1 FTIR of PAN powder and electrospun PAN fiber mat

Figure 2.20 shows FTIR spectra of PAN copolymer powder and electrospun fiber mat. The characteristic peaks of PAN are labeled in the spectra. Compared to PAN powder, no peak shift is observed in the electrospun fiber mat, indicating that electrospinning does not change PAN polymer chain conformation.

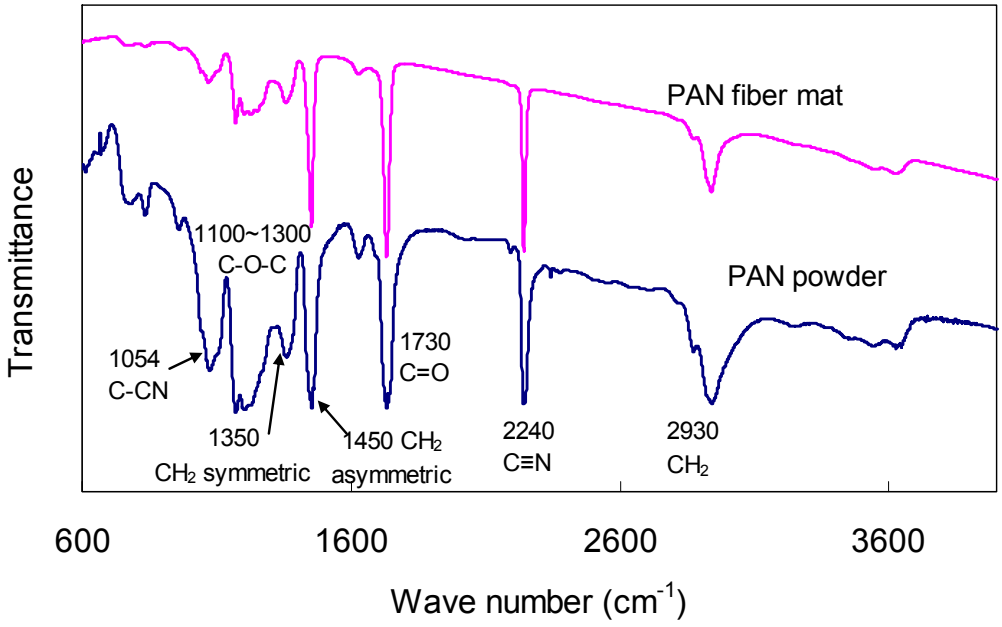

Figure 2.20. FTIR spectra of PAN powder and PAN fiber mat (PAN copolymer with MW 100,000 g/mol, 16.1 wt% PAN in DMF, flow rate is 1 ml/hr, the distance between the needle tip and the target is 10 cm, and voltage is 22 kV)

2.3.5.2 PAN-$ZnCl_2$ interaction and characterization

When electrospinning bead free small diameter PAN fibers, $ZnCl_2$ was added into the PAN solution to increase the charge density of the solution. The added salt interacts with the polymer and forms a zinc ion-nitrile complex.[49] Work by Hoskins et al[49] showed FTIR evidence of complex formation between the zinc ions and the nitrile groups of the polymer in aqueous solution by splitting of nitrile peak. However, the concentration of $ZnCl_2$ used to prepare solution was quite high (40-60 wt %). In a later study, Edwards and co workers[50] used Raman spectroscopy to quantify the amount of nitrile groups engaged in the complex formation with zinc ions in aqueous solutions. At 60 wt % $ZnCl_2$ (in aqueous solution), only 25% of total nitrile were found to be complexed with zinc ions, while the remaining stayed as free nitrile. The mole ratio of salt to polymer in this solution was 0.084 mols $ZnCl_2$ to 0.019 mols acrylonitrile units, hence moles of salt are in significant excess compared to polymer.

In this study, the FTIR spectra of electrospun PAN/$ZnCl_2$ fiber mats do not show any change in the nitrile peak (~2240 cm^{-1}) (Figure 2.21). Two possible reasons are (1) $ZnCl_2$ concentration is not high enough for complex formation (the mole ratio of salt to polymer was 0.0058 mols $ZnCl_2$ to 0.302 mols acrylonitrile units) and (2) a complex between nitrile and $ZnCl_2$ may have formed, however, the degree of complexation is so small that it can not be detected by FTIR. Cho et al[51] studied the properties of PAN fiber processed from DMF/$ZnCl_2$. Any shift in the nitrile peak which could indicate complex formation was not observed, however, $ZnCl_2$ concentration used in this study was very low (0.00068 wt %).

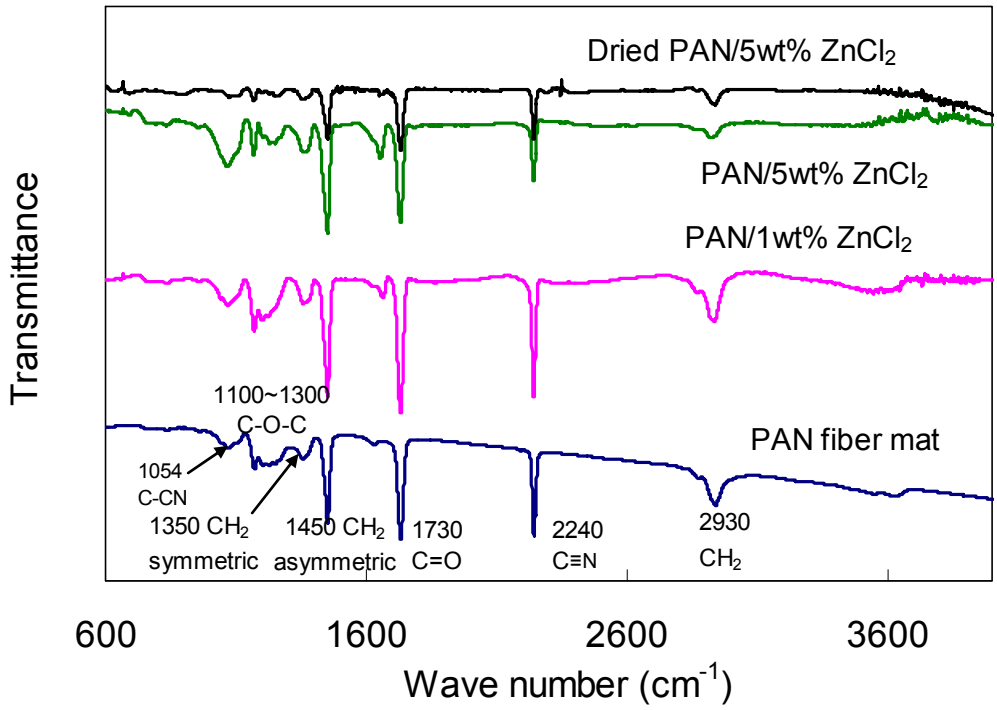

Figure 2.21. FTIR spectra of electrospun PAN and PAN/$ZnCl_2$ fiber mats (PAN copolymer with MW 100,000 g/mol, 16.1 wt% PAN in DMF, flow rate is 1 ml/hr, the distance between the needle tip and the target is 10 cm, and voltage is 22 kV)

.

Instead of shift of nitrile peak, an additional peak (~ 1644 cm^{-1}) was observed in FTIR spectra with addition of $ZnCl_2$ (Figure 2.22). With increasing $ZnCl_2$ concentration, the peak intensity increases. In this work, the solutions for electrospinning were prepared using DMF as solvent. Phadke et al[52] studied the interaction between PAN, salt and solvent using DMF as solvent and a variety of salts including LiCl, $ZnCl_2$ and $AlCl_3$. All three salts formed complex with both DMF and PAN, however, results indicate that the strength of interaction of zinc ion is higher for carbonyl of DMF than nitrile of PAN. Hence in our case, strong interaction between zinc ions and carbonyl of DMF impeding complex formation between zinc ion and nitrile of PAN is also expected. The additional peak observed at 1644 cm^{-1} may come from the complexation between zinc ions and carbonyl of DMF. In fact, this peak

disappears after vacuum drying electrospun PAN/$ZnCl_2$ fiber mat at 90°C for 24 hrs, further confirming the interaction between zinc ions and residual DMF.

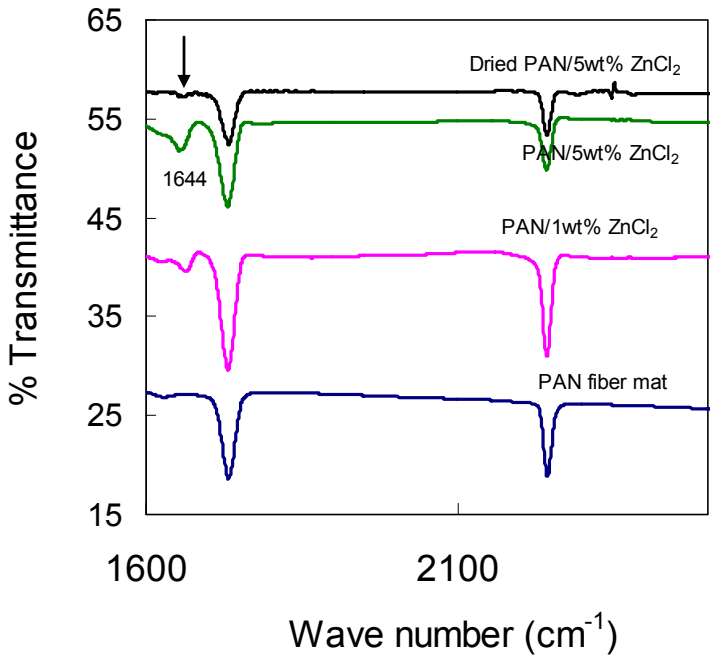

Figure 2.22. FTIR spectra of PAN/$ZnCl_2$ fiber mats(1600~2600 cm^{-1}) (PAN copolymer with MW 100,000 g/mol, 16.1 wt% PAN in DMF, flow rate is 1 ml/hr, the distance between the needle tip and the target is 10 cm, and voltage is 22 kV).

2.3.6 WAXD study of electrospun PAN fiber mats

Wide angle X-ray diffraction (WAXD) was conducted on various PAN fiber mats electrospun under different conditions to study the crystal size and crystallinity. In this section, the crystal size and crystallinity of electrospun PAN fiber mat is compared to those of solution cast PAN films. The effect of the addition of $ZnCl_2$ in the electrospinning solution on crystal size and crystallinity of PAN fiber mat and film is also studied. WAXD data of PAN fiber mats processed under varying electrospinning parameters are given in Appendix A.

2.3.6.1 WAXD study of electrospun PAN fiber mat and films

WAXD was conducted on electrospun PAN fiber with 200 nm diameter, solution cast film (Film-A, PAN polymer film), and solution cast Film-B (redissolved electrospun PAN fiber mat). The integrated intensity is plotted as a function of 2θ in Figure 2.23 and the results are given in Table 2.7. It shows that the diffraction peak of electrospun fiber mat at 16.9° is much broader than that of the films. Compared to the solution cast films, the crystal size of electrospun PAN fiber mat is much smaller. The small crystal size for the electrospun PAN fiber mats indicate that the crystal structures are poorly developed during electrospinning. The rapid solvent evaporation hinders the growth of crystals during electrospinning. For solution cast films, relatively slow solvent evaporation allows sufficient time for crystal growth, resulting in larger crystal size. Other studies on electrospun PAN fibers [53] have also shown a broad peak at 2θ of 17.2° and the absence of diffraction peak at 2θ of 29.8°. A broad diffraction peak and a lack of higher order diffraction peaks have also been observed in electrospun poly(ethylene oxide) fibers when compared to the powder.[14]

Table 2.7. WAXD results of electropun PAN fiber mat and films.

Sample	**2 θ (°)**	**d spacing (Å)**	**Crystal size (Å)**	**Crystallnity (%)**
PAN fiber mat*	16.9	5.2	29	57
Film-A	16.9	5.2	58	62
Film-B	16.9	5.2	64	54

* PAN copolymer, MW 100,000 g/mol, concentration is 16.1 wt%, solvent is DMF, flow rate is 1ml/hr, the distance between the needle tip and the target is 10 cm, and voltage is 22 kV.

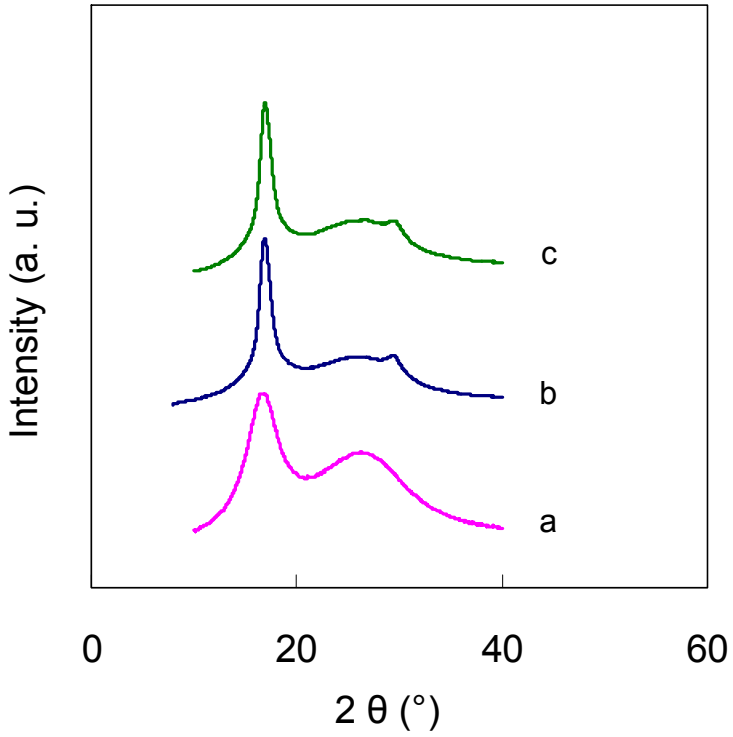

Figure 2.23. Plots of integrated intensity as a function of 2θ for (a) electrospun fiber mat (PAN copolymer, MW 100,000 g/mol, concentration is 16.1 wt%, solvent is DMF, flow rate is 1ml/hr, the distance between the needle tip and the target is 10 cm, and voltage is 22 kV), (b) Film-A, and (c) Film-B.

2.3.6.2 WAXD study of PAN/$ZnCl_2$ fiber mats and films

The PAN nanofibers with diameter of 200 nm were electrospun from PAN/DMF solutions containing 1 and 5 wt% $ZnCl_2$. WAXD was conducted on $ZnCl_2$ powder, $ZnCl_2$/DMF solution, electrospun PAN and PAN/$ZnCl_2$ (99/1 and 95/5) fiber mats, as well as PAN and PAN/$ZnCl_2$ (95/5) cast films (Film-A and Film-C). The integrated intensity is plotted as a function of 2θ in Figure 2.24 and the results are summarized in Table 2.8. For $ZnCl_2$ powder, peaks characteristics of zinc chloride crystals are present. After dissolving in DMF, $ZnCl_2$ crystal peaks have disappeared, and only an amorphous halo was observed. When $ZnCl_2$ is dissolved in DMF, it dissociates into Zn^{2+} and Cl^- ions, and no longer exists as crystals, which are otherwise

present in the solid state. For both PAN/$ZnCl_2$ fiber mats and film, no $ZnCl_2$ peaks are present. For electrospun PAN fiber mats, with addition of $ZnCl_2$, crystallinity decreases from 57 % to 36 %. It is possible that either Zn^{2+} or Cl^- ions associate with PAN polymer chains in solution state, which may hinder the crystallization of PAN upon solvent evaporation. However, since the concentration of $ZnCl_2$ is very low, the complex structure between PAN and Zn^{2+} could not be detected from FTIR spectra.

Table 2.8. WAXD results of PAN and PAN/$ZnCl_2$ fiber mats and films.

Sample	**2 θ (°)**	**d spacing (Å)**	**Crystal size (Å)**	**Crystallinity (%)**
PAN fiber mat*	16.9	5.2	29	57
PAN/$ZnCl_2$ (99/1) fiber mat*	16.7	5.3	26	38
PAN/$ZnCl_2$ (95/5) fiber mat*	16.7	5.3	28	36
Film-A	16.9	5.2	58	62
Film-C	16.9	5.2	56	50

* Electrospinning conditions: PAN copolymer, MW 100,000 g/mol, solvent is DMF, solid content is 16.1 wt%, flow rate is 1 ml/hr, the distance between the needle tip and the target is 10 cm, and voltage is 22 kV.

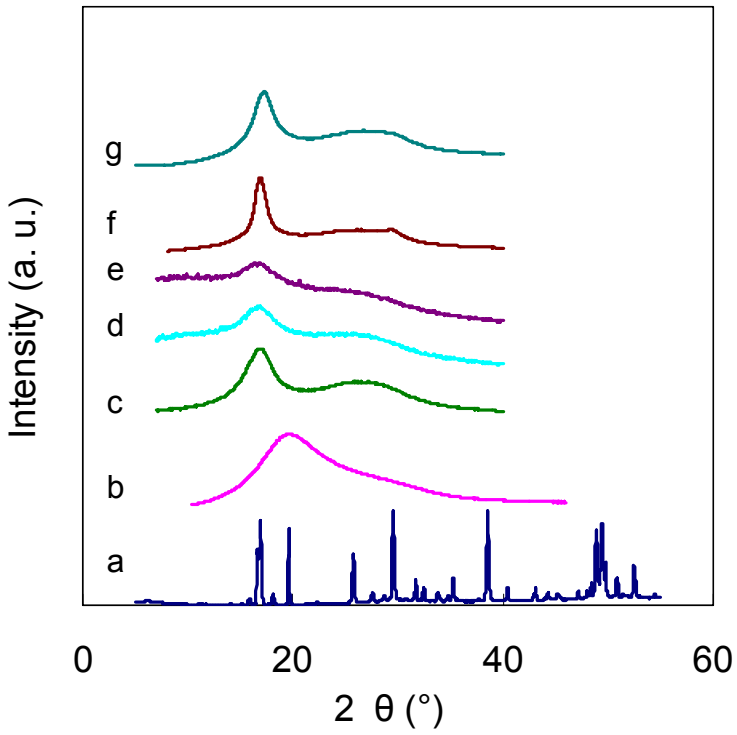

Figure 2.24. Plots of integrated intensity as a function of 2θ for (a) $ZnCl_2$ powder, (b) 1 wt% $ZnCl_2$/DMF solution in a glass capillary, (c) PAN fiber mat, (d) PAN/$ZnCl_2$ (99/1) fiber mat, (e) PAN/$ZnCl_2$ (95/5) fiber mat, (f) PAN film, and (g) PAN/$ZnCl_2$ (95/5) film (PAN copolymer, MW 100,000 g/mol, concentration is 16.1 wt%, solvent is DMF, flow rate is 1ml/hr, the distance between the needle tip and the target is 10 cm, and voltage is 22 kV).

2.3.7 Electrospinning of PAN/CNT nanofibers

2.3.7.1 Morphology of PAN/CNT nanofibers

PAN/SWNT and PAN/MWNT dispersions were electrospun into the fiber mats. Figure 2.25 shows the SEM images of electropun PAN/CNT fiber mats. At low CNT concentration, the fiber surface is smooth. At high CNT concentration, fiber surface appears rather corrugated.

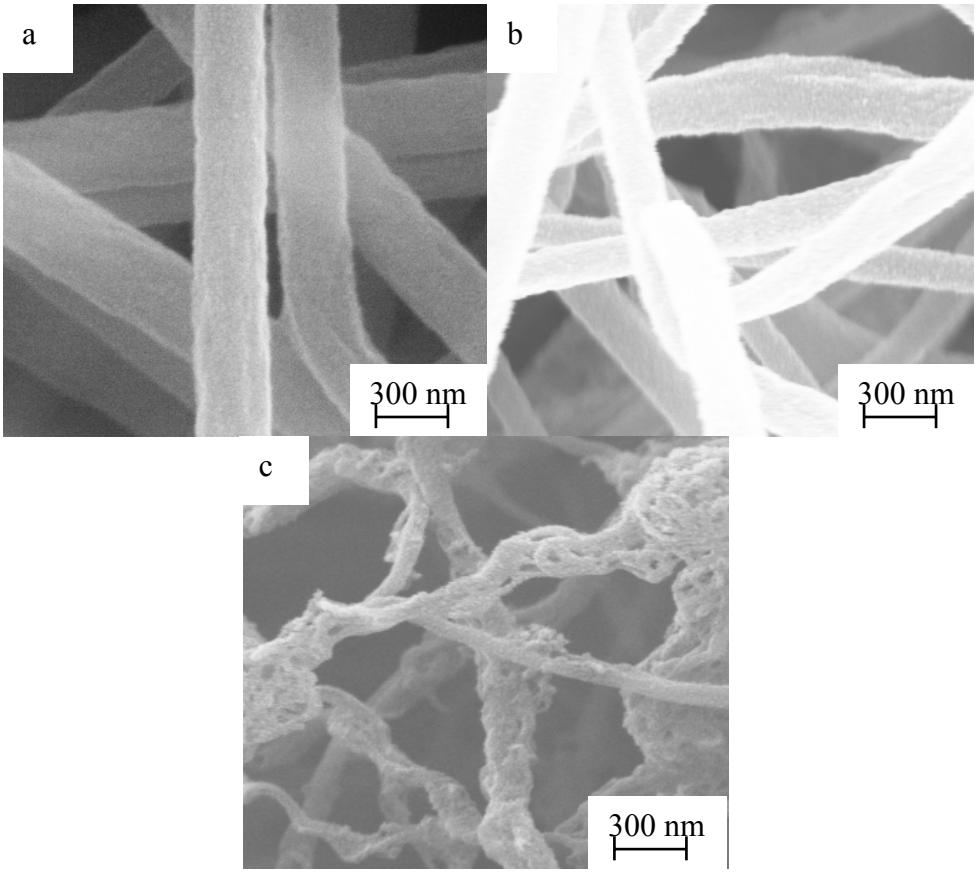

Figure 2.25. Scanning electron micrographs of (a) PAN/SWNT (99.9/0.1) fiber mat, (b) PAN/SWNT (95/5) fiber mat, and (c) PAN/MWNT (70/30) fiber mat (PAN copolymer with MW of 100,000 g/mol, the solid contents for PAN/SWNT and PAN/MWNT dispersions are 12 wt% and 10 wt%, respectively. Flow rate is 1 ml/hr, the distance between the needle tip and the target is 10 cm, and voltage is 22 kV).

SWNT or MWNT can be incorporated into PAN matrix where a nanotube core and polymer shell structure forms. The electrospun PAN/SWNT (99.9/0.1) fiber mat was observed by high resolution transmission electron microscopy (TEM). The TEM image shows that SWNT bundle with diameter of 20~30 nm wrapped by PAN is aligned along the fiber axis (Figure 2.26).

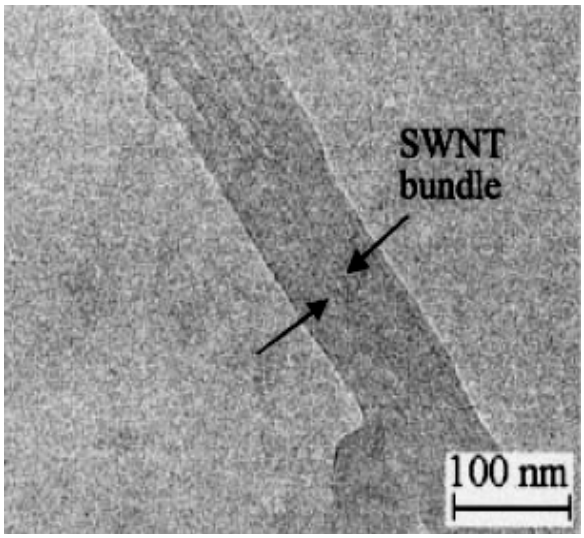

Figure 2.26. Transmission electron micrograph of electrospun PAN/SWNT (99.9/0.1) nanofiber (The solid content of dispersion is 12 wt%, flow rate is 1 ml/hr, the distance between the needle tip and the target is 10 cm, and voltage is 22 kV) (Micrograph courtesy of Dr. Tetsuya Uchida)

2.3.7.2 Raman spectra of electrospun PAN/SWNT nanofibers

Raman spectroscopy was conducted on electrospun PAN/SWNT fiber mats to study the interaction between SWNT and PAN. Raman spectroscopy is a nondestructive technique that can be used to characterize SWNT and its interaction with other molecules. Four characteristic peaks show up in Raman spectrum when SWNT is present (Figure 2.27): low frequency Radial Breathing Modes (100~300 cm^{-1}, RBM band), the tangential G band (~1600 cm^{-1} and derived from the graphite like in plane mode), the disorder induced D band (~1300 cm^{-1}), and the G' band (~2600 cm^{-1}, also considered as overtone of D band).[54] Under the effect of pressure[55] and temperature,[56] the G and G' band position shift, and this can be used to monitor the deformation of carbon nanotubes. Under a tensile strain, both G and G' bands shift to a lower wave number; upon compression or pressure, they shift to a higher wave number.[57]

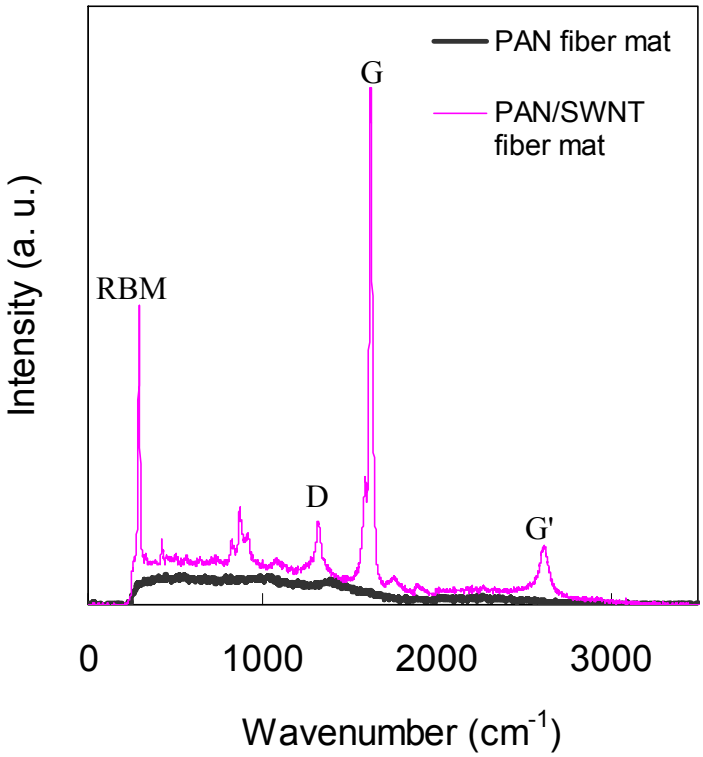

Figure 2.27. Raman spectra of electrospun PAN/SWNT(99.9/0.1) and PAN fiber mat (PAN copolymer, the solid content of dispersion is 12 wt%, MW 100,000 g/mol, flow rate is 1 ml/hr, the distance between the needle tip and the target is 10 cm, and voltage is 22 kV).

When SWNTs are embedded in a polymer matrix, they are compressed. The compressive force can be indicated by the up shift of G and G' band positions. In this work, Raman spectroscopy was conducted on SWNT powder (HiPCO), PAN/SWNT (99.9/0.1) composite film, and electrospun fiber mats. Their spectra are given in Figure 2.28. Four characteristic peaks of SWNT were observed in all the samples. Compared to SWNT powder, the G and G' band of electrospun PAN/SWNT fiber mat and film shift to higher wave numbers, suggesting compressive strain on SWNT bundles during electrospinning or film casting (Figure 2.29 and Figure 2.30, Table 2.9). Electrospun composite fiber mat shows a higher G or G' band up shift as compared to the composite film. During electrospinning, the rapid solvent

evaporation causes the fast solidification and shrinkage of polymer, which can apply a strong compressive force onto the SWNT bundle, resulting in up shift of the G or G' bands. The up shift of G and G' bands was also reported in electrospun poly (methyl methacrylate)/SWNT nanofibers.[58] Raman spectroscopy was also conducted on PAN/SWNT fiber mats electropun at different votlages. Figure 2.31 gives their spectra and the results are summarized in Table 2.9. Compared to SWNT powder and PAN/SWNT film, the G band and G' band in all fiber mats show up shift regardless of voltage (Figure 2.32 and Figure 2.33). However, the up shift wave number of the G and G' bands does not show a trend with increasing of voltage.

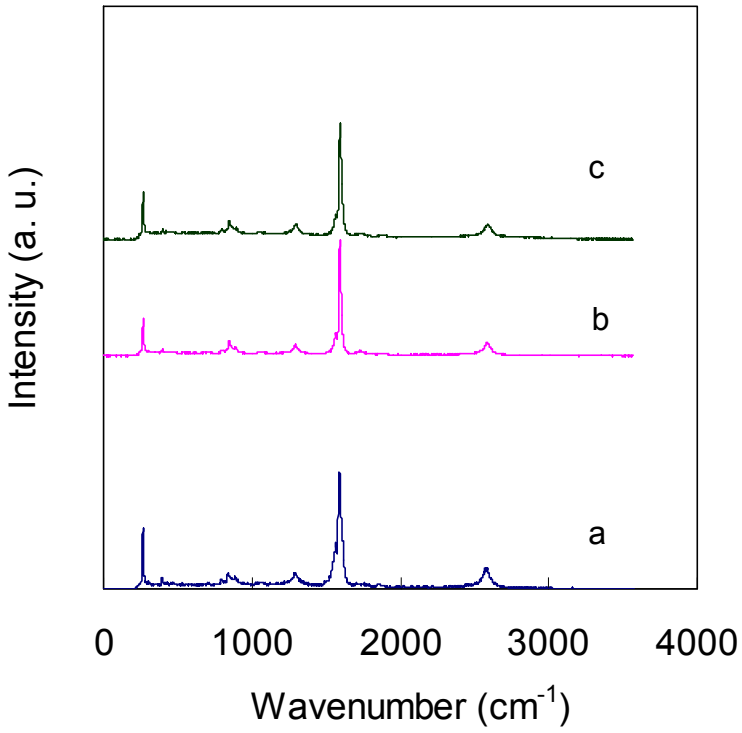

Figure 2.28. Raman spectra of (a) SWNT powder, (b) PAN/SWNT (99.9/0.1) film, and (c) electrospun PAN/SWNT fiber mat (99.9/0.1) (PAN copolymer, MW 100,000 g/mol, the solid content of dispersion is 12 wt%, flow rate is 1 ml/hr, the distance between the needle tip and the target is 10 cm, and voltage is 19 kV).

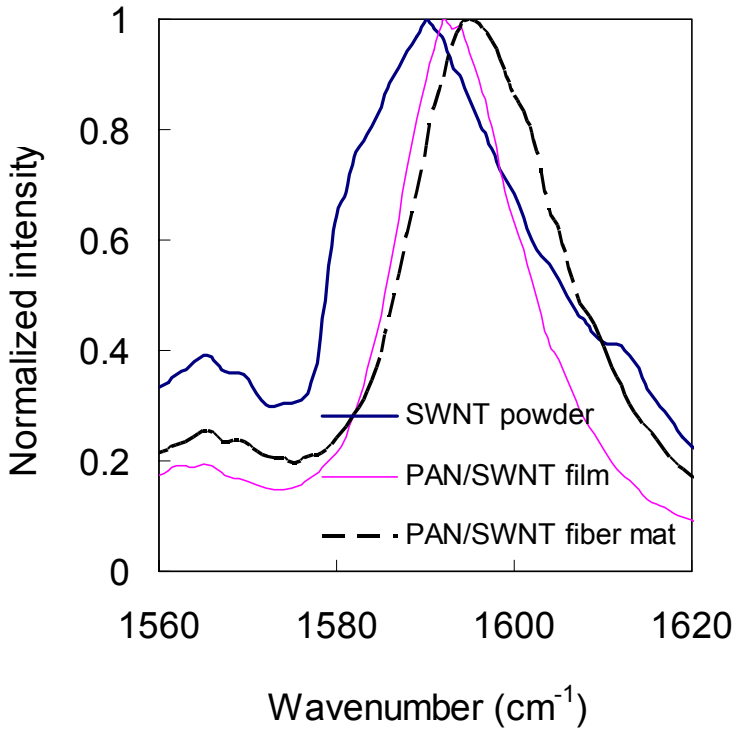

Figure 2.29. G band position of SWNT powder, PAN/SWNT (99.9/0.1) composite film and nanofibers (PAN copolymer, MW 100,000 g/mol, the solid content of dispersion is 12 wt%, flow rate is 1 ml/hr, the distance between the needle tip and the target is 10 cm, and voltage is 19 kV).

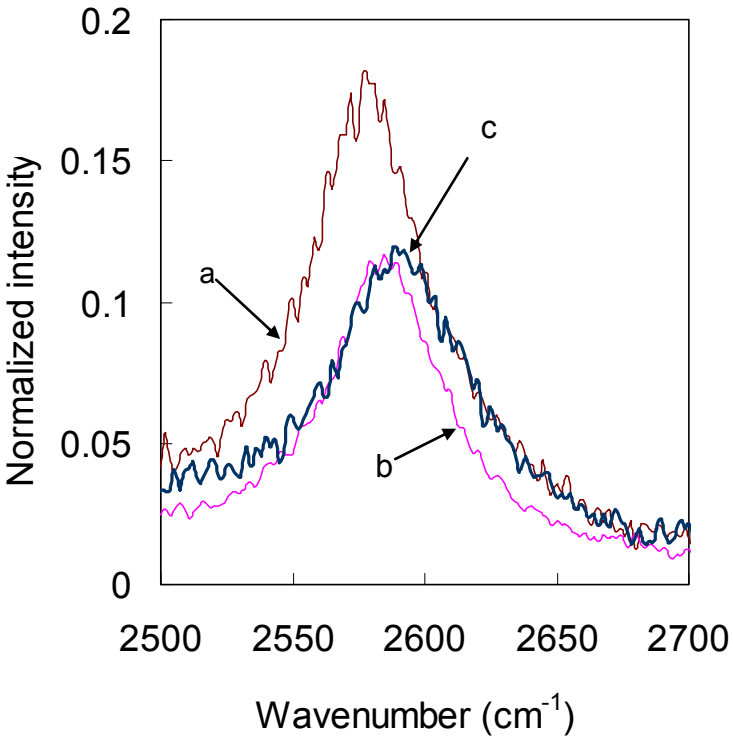

Figure 2.30. G' band position of (a) SWNT powder, (b) PAN/SWNT (99.9/0.1) film, and (c) electrospun PAN/SWNT (99.9/0.1) fiber mat (PAN copolymer, MW 100,000 g/mol, the solid content of dispersion is 12 wt%, flow rate is 1 ml/hr, the distance between the needle tip and the target is 10 cm, and voltage is 19 kV).

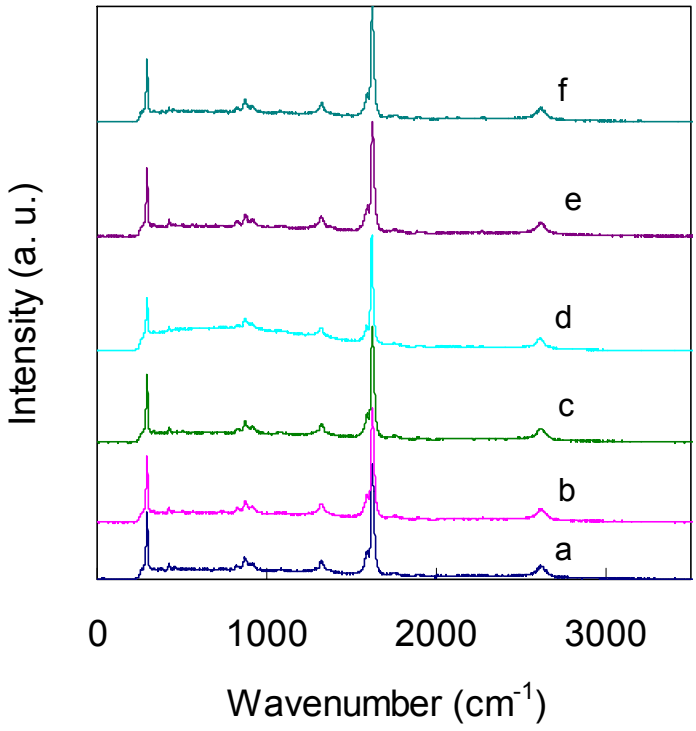

Figure 2.31. Raman spectra of electrospun PAN/SWNT (99.9/0.1) fiber mats at different voltage of (a) 13 kV, (b) 16 kV, (c) 19 kV, (d) 22 kV, (e) 25 kV, and (f) 27 kV (PAN copolymer, MW 100,000 g/mol, the solid content of dispersion is 12 wt%, flow rate is 1 ml/hr, the distance between the needle tip and the target is 10 cm).

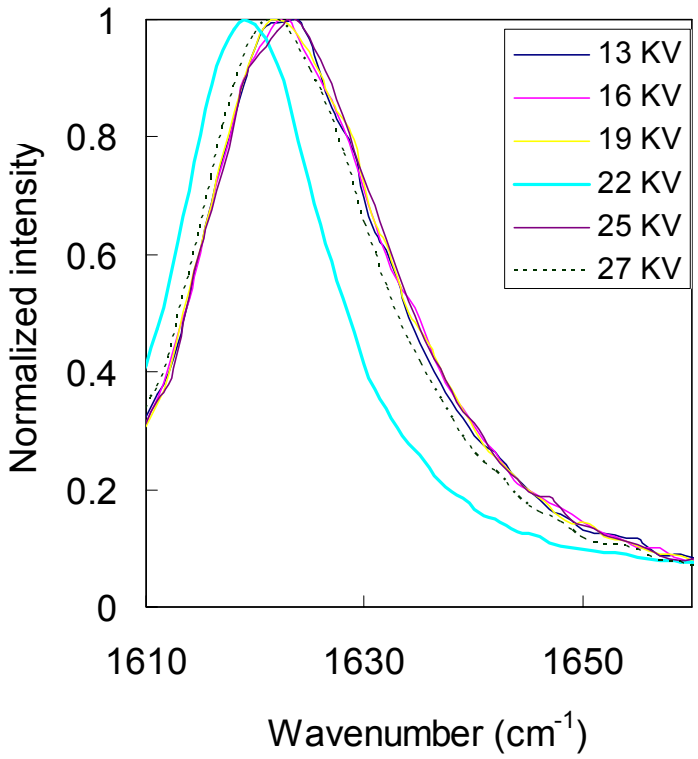

Figure 2.32. G band position of PAN/SWNT (99.9/0.1) fiber mats electropun at different voltages (PAN copolymer, MW 100,000 g/mol, the solid content of dispersion is about 12 wt%, flow rate is 1 ml/hr, the distance between the needle tip and the target is 10 cm).

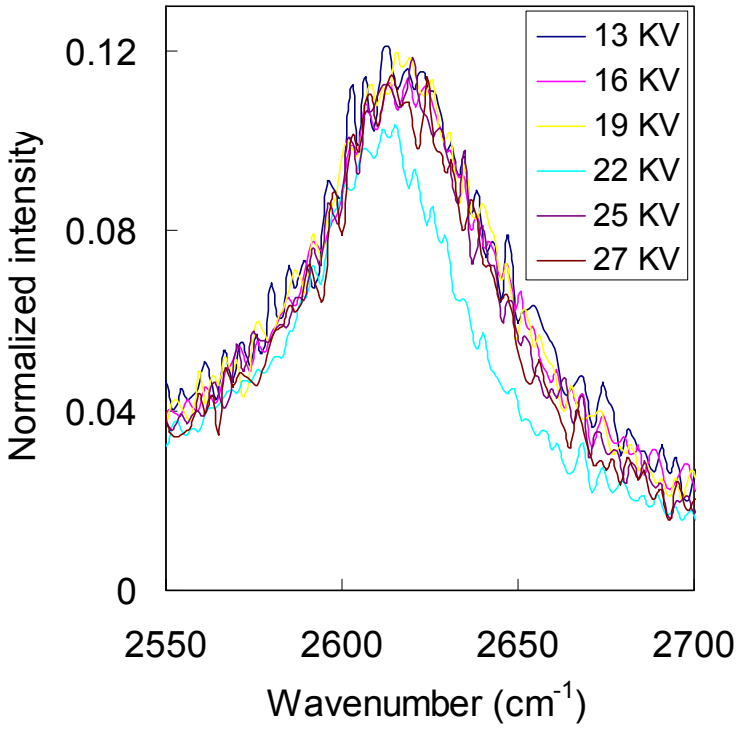

Figure 2.33. G' band position of PAN/SWNT (99.9/0.1) fiber mats electropun at different voltages (PAN copolymer, MW 100,000 g/mol, the solid content of dispersion is 12 wt%, flow rate is 1 ml/hr, the distance between the needle tip and the target is 10 cm).

Table 2.9. G and G' band position of SWNT powder, PAN/SWNT (99.9/0.1) composite film and fiber mats electrospun at different voltages.

Sample		**G band position (cm^{-1})**	**G' band position (cm^{-1})**
SWNT powder		1590	2577
PAN/SWNT film		1592	2579
Electrospun PAN/SWNT fiber mat*	13 kV	1597	2586
	16 kV	1596	2592
	19 kV	1595	2589
	22 kV	1592	2588
	25 kV	1597	2593
	27 kV	1595	2587

* PAN copolymer, MW 100,000 g/mol, solid content of dispersion is 12 wt%, flow rate is 1 ml/hr, the distance between the needle tip and the target is 10 cm.

2.3.8 High speed photography of the electrospinning process

High speed photography was used to record the electrospinning process of PAN solutions and PAN/carbon nanotube dispersions. Figure 2.34 to 2.36 show various photography regions (A, B, and C as described in Figure 2.1) for the electrospinning process of PAN solutions at different concentrations. The three stages in the electrospinning process, namely Taylor cone formation, jet initiation, and jet whipping were observed. When the jet initiates from the Taylor cone, it first goes for a straight distance and then undergoes whipping and bending. Similar observations have also been reported in the literature.[59, 60]

When electrospinning low concentration PAN/DMF solution (1 wt%), the jet is straight for a short distance then bends with occurrence of jet breaking up (Figure 2.34 (a)). Insufficient polymer chain entanglements in the low concentration solution

may be responsible for jet break up. Electrospinning at 9 and 16 wt% polymer concentration, resulted in a single continuous jet without break up (Figure 2.35 (b) and Figure 2.36 (b)). At high solution concentration, the jet whipped very frequently at the final stage, therefore, only the first two positions (A and B) could be imaged for PAN solutions with concentration of 9 and 16 wt%.

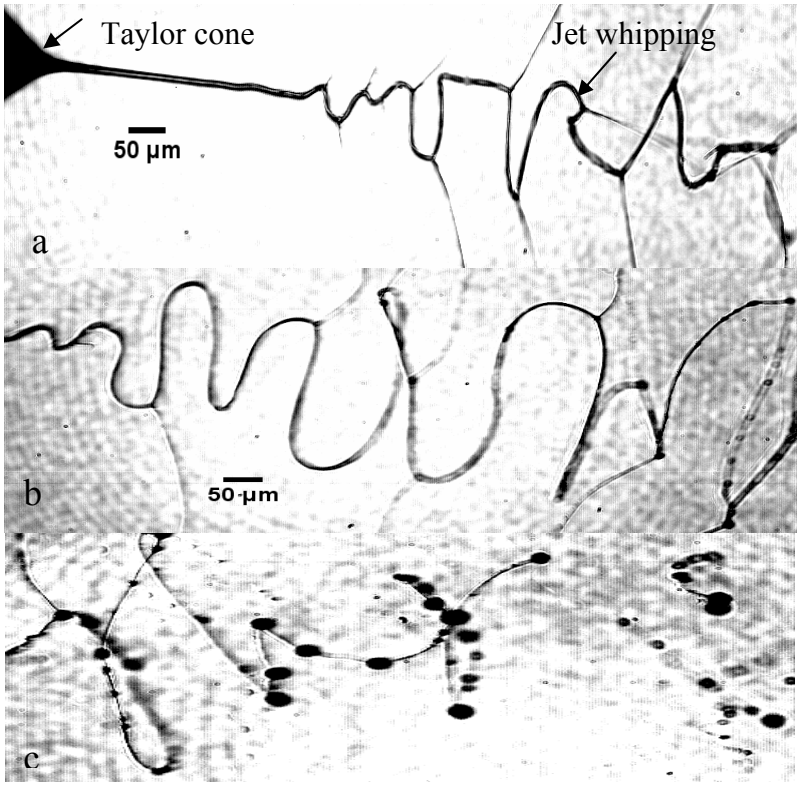

Figure 2.34. High speed photographs of electrospinning process of 1 wt% PAN/DMF solution of (a) region A, (b) region B, and (c) region C (PAN copolymer, MW 100,000 g/mol, flow rate is 1 ml/hr, the distance between the needle tip and the target is 10 cm, and voltage is 22 kV).

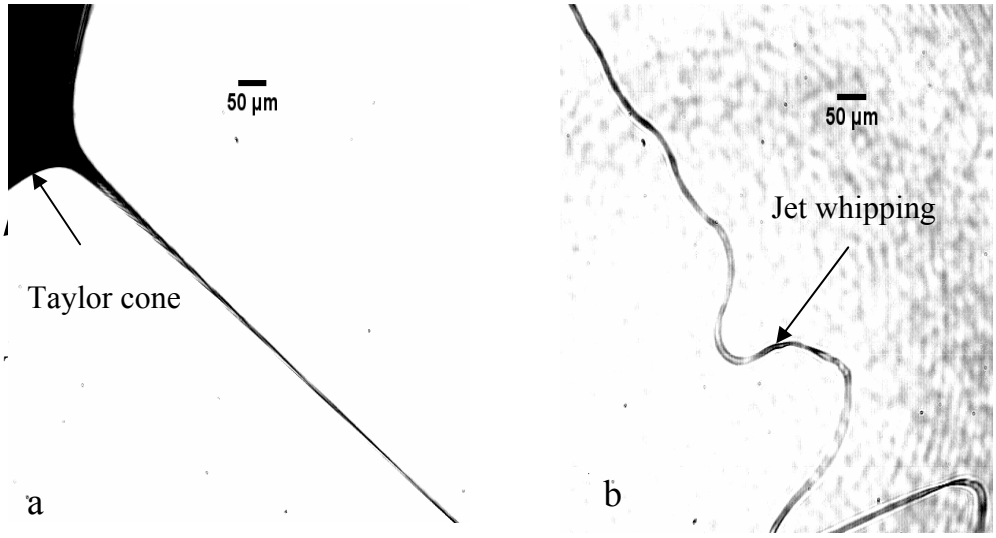

Figure 2.35. High speed photographs of electrospinning process of 9 wt% PAN/DMF solution of (a) region A and (b) region B (PAN copolymer, MW 100,000 g/mol, flow rate is 1 ml/hr, the distance between the needle tip and the target is 10 cm, and voltage is 22 kV).

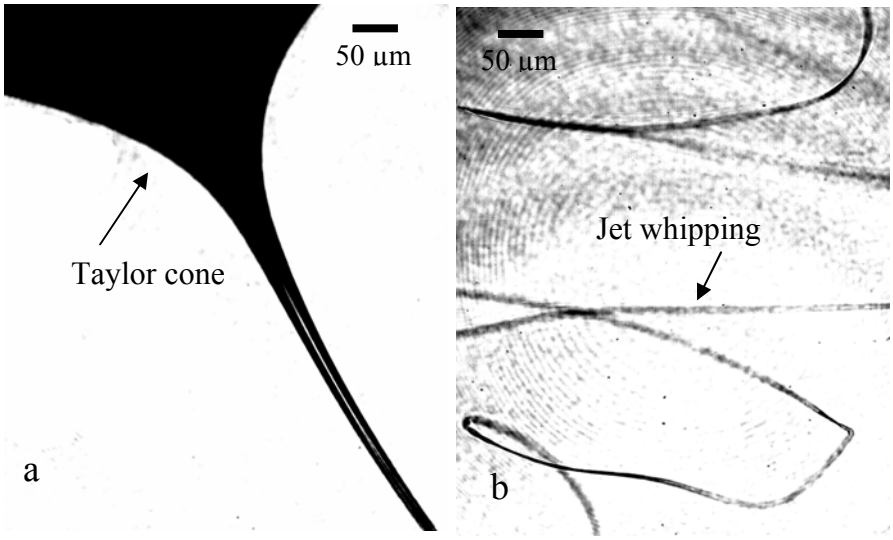

Figure 2.36. High speed photographs of electrospinning process of 16 wt% PAN/DMF solution of (a) region A and (b) region B (PAN copolymer, MW 100,000 g/mol, flow rate is 1 ml/hr, the distance between the needle tip and the target is 10 cm, and voltage is 22 kV).

The semi-angles of the Taylor cones were measured as shown in Figure 2.37 and the results are listed in Table 2.10. The shapes of the Taylor cones observed in Figure 2.37 (a), (b), (c), (d), (e), (g), and (h) are similar to those reported in the literature,[61, 62] while a different shape of Taylor cone was shown in Figure 2.37 (f), which was also observed in other work.[63] The semi-angle of Taylor cone of PAN/SWNT is the highest, with a value of about 73°. For PAN solutions, the semi-angle of Taylor cone slightly increased with solution concentration. Semi-angle was reported to be 49° for water[64] and 33.5° for poly(ethylene oxide).[62] No explanation for the observation of different Taylor cone semi-angles has been provided in the literature. The variation of electric field and solution viscoelasticity may be the possible reasons for variation in Taylor cone angle.

Table 2.10. Semi-angle of Taylor cone of electrospinning of PAN solutions and PAN/CNT dispersions.

Solution or dispersion		**Taylor cone semi angle (°)**
Theoretical		49
1 wt % PAN	(a) 13 kV	29 ± 4
	(b) 22 kV	30 ± 3
	(c) 25 kV	31 ± 3
	(d) 27 kV	39 ± 3
(e) 9 wt% PAN(22 kV)		37 ± 2
(f) 16 wt% PAN(22 kV)		58 ± 3
(g) 12 wt% PAN/SWNT (95/5)(22 kV)		73 ± 3
(h) 10 wt% PAN/MWNT (70/30)(22 kV)		37 ± 2

(Flow rate is 1 ml/hr, the distance between the needle tip and the target is 10 cm).

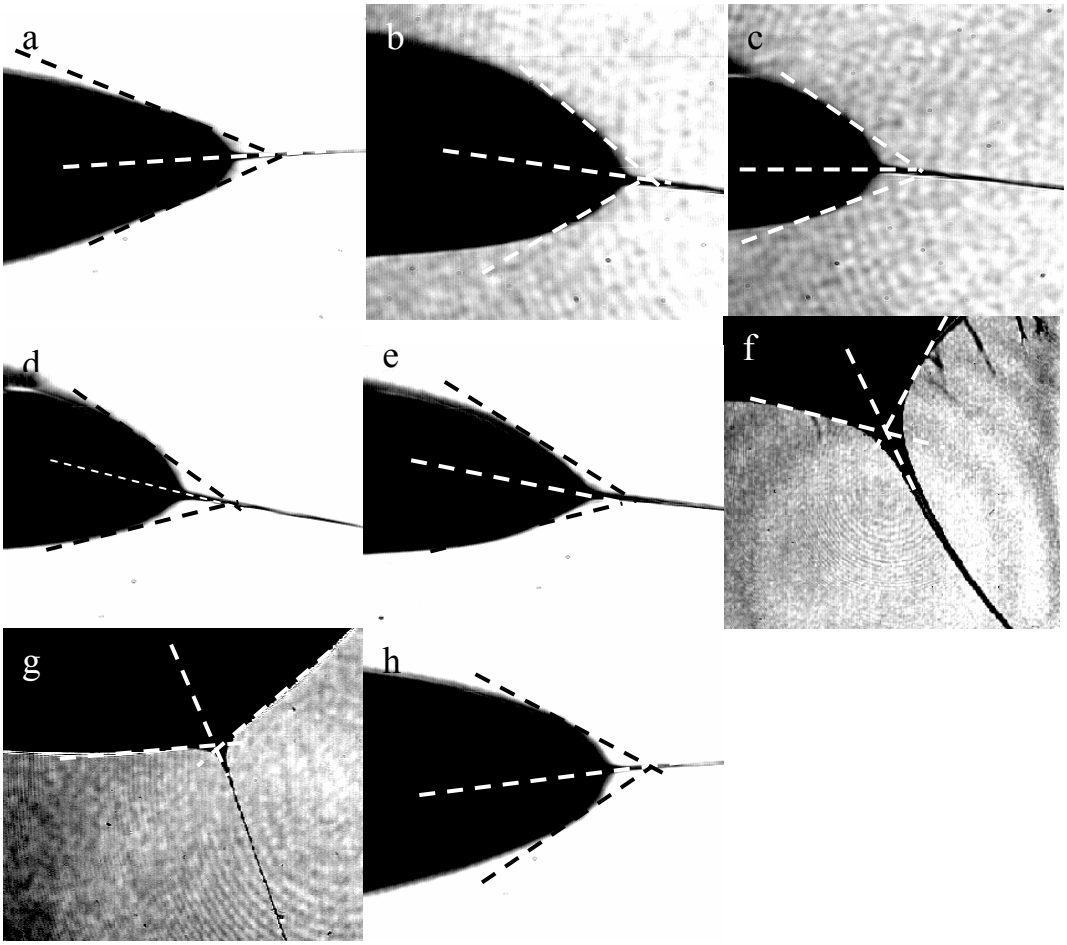

Figure 2.37. Semi-angle of Taylor cone of (a) 1 wt% PAN solution (13 kV), (b) 1 wt% PAN solution (22 kV), (c) 1 wt% PAN solution (25 kV), (d) 1 wt% PAN solution (27 kV), (e) 9 wt% PAN solution (22 kV), (f) 16 wt% PAN solution (22 kV), (g) 12 wt% PAN/SWNT dispersion (22 kV), and (h) 10 wt% PAN/MWNT dispersion (22 kV) (For all the electrospinning processes, flow rate is 1 ml/hr, the distance between the needle tip and the target is 10 cm)

Figure 2.38 shows the high speed photographs of 1 wt% PAN solution electrospun at different voltages. Several secondary jets were observed to emanate from the primary jet to form branching. It is also noted that the branches appear only at bent section, while no branches were observed at straight section of the jet. At higher PAN concentrations (9 and 16 wt%), no branching was observed.

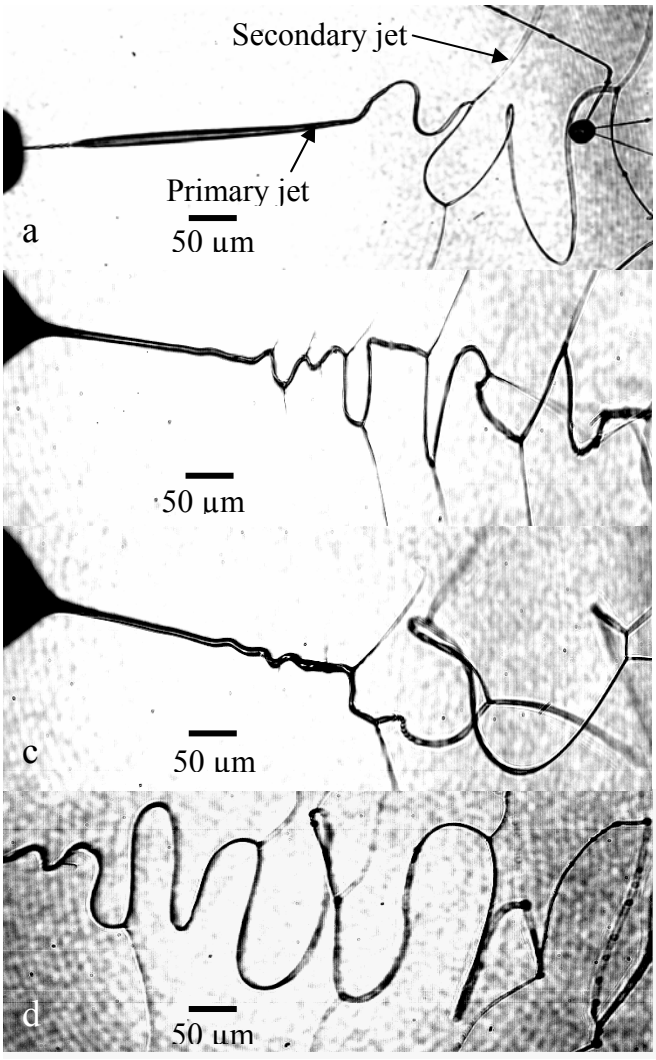

Figure 2.38. High speed photographs of PAN/DMF solution (1 wt%) electrospun at different voltages of (a) 13 kV, (b) 22 kV, (c) 25 kV, and (d) 27 kV (PAN copolymer, MW 100,000 g/mol, flow rate is 1 ml/hr, the distance between the needle tip and the target is 10 cm).

Jet branching was also observed when electrospinning PAN/CNT dispersions. Figure 2.39 and 2.40 give high speed photographs of electrospinning process of PAN/SWNT (95/5) and PAN/MWNT (70/30) dispersions, respectively. For both electrospinning processes, short and long branches were observed at straight and bent sections of the jet, respectively. Compared to PAN/SWNT, the branching density of PAN/MWNT jet is much higher.

Branching appears in both PAN and PAN/CNT fiber jets, however, at different locations. The high speed photographs show that all the fiber jets have two sections: straight and bent sections. Branching occurs only at bent sections of the jet, when electrospinning a low concentration PAN solution (Figure 2.38). On the other hand, branching was observed at both straight and bent sections, when electrospinning PAN/CNT dispersions (Figure 2.39 and Figure 2.40).

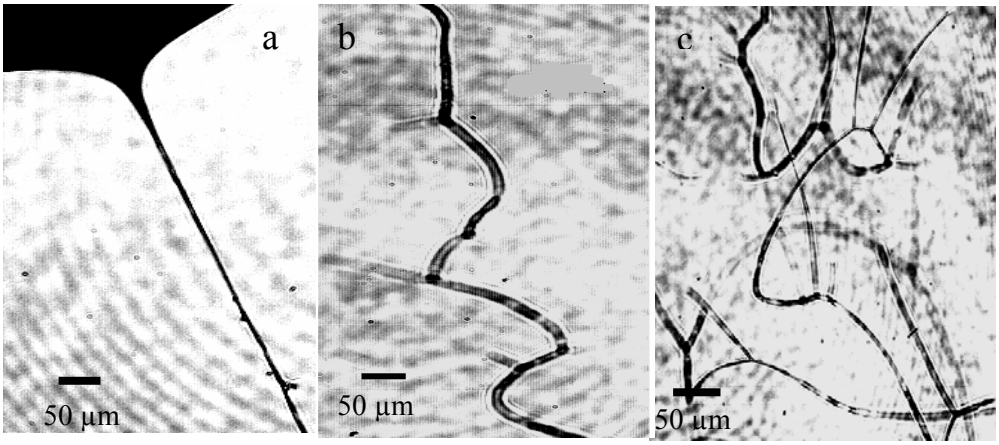

Figure 2.39. High speed photographs of electrospinning of PAN/SWNT (95/5) for (a) region A, (b) region B, and (c) region C (solid content of PAN/SWNT in DMF dispersion is about 12 wt%, flow rate is 1 ml/hr, the distance between the needle tip and the target is 10 cm, and voltage is 22 kV).

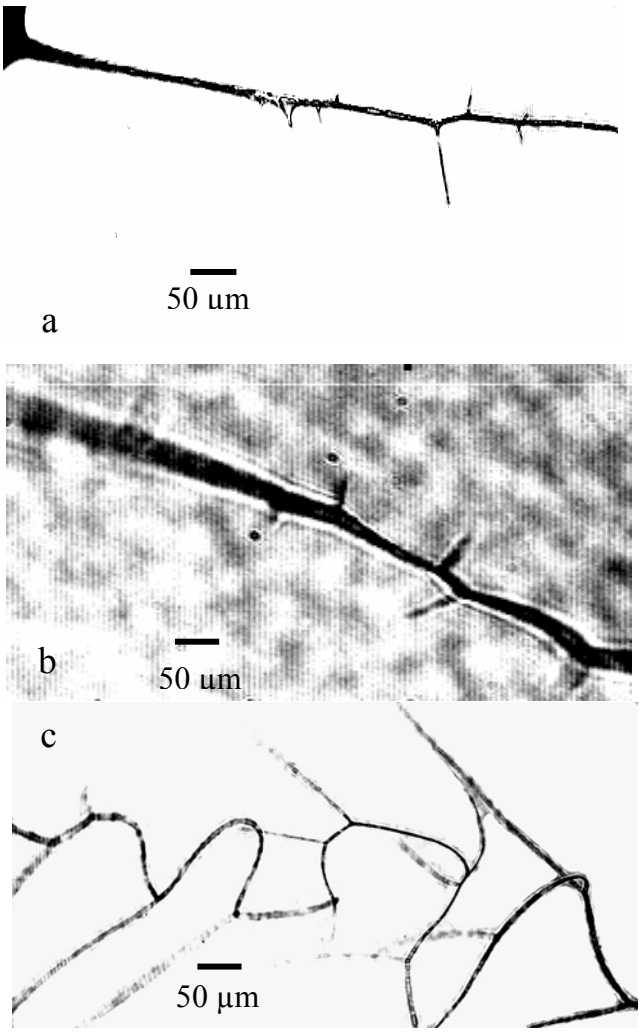

Figure 2.40. High speed photographs of electrospinning of PAN/MWNT (70/30) for (a) region A, (b) region B, and (c) region C (concentration of PAN/MWNT in DMF dispersion is about 10 wt%, flow rate is 1 ml/hr, the distance between the needle tip and the target is 10 cm, and voltage is 22 kV).

Jet branching was reported in poly(2-hydroxyethyl methacrylate) (HEMA) when electrospun from ethanol and formic acid mixture[65] and in poly(caprolacton) when electrospun from acetone.[66] In this work, the "charge redistribution" was proposed to explain the origination of jet branching. It was stated that during electrospinning, jet shape and the charge density can possibly be changed by the jet elongation and rapid solvent evaporation. The balance between the surface tension and electrical forces may be shifted, resulting in unstable charge distribution. To stabilize the jet, secondary jets are ejected from the surface of the primary jet, resulting in branching.

2.4 Conclusions

Key conclusions of this study are summarized below:

- PAN fiber diameter is significantly affected by solution flow rate or distance between the needle tip and the target, while it was relatively insensitive to change in voltage at a given distance or flow rate.
- The solution concentration plays an important role in controlling fiber diameter and morphology. Electrospinning of PAN solution in the semidilute unentangled regime resulted in microscopic and nanoscopic particles, while the continuous fibers were obtained when solution was in the semidilute entangled regime. The PAN fiber diameter (d) exhibited two distinct power law dependences on the concentration (C) in the semidilute entangled regime ($d \sim C^{1.2}$ and $C^{7.5}$ for PAN of 100, 000 g/mol molecular weight; $d \sim C^{0.88}$ and $C^{3.5}$ for PAN of 250,000 g/mol molecular weight, and $d \sim C^{0.99}$ and $C^{2.5}$ for PAN of 700,000 g/mol molecular weight).

- Addition of $ZnCl_2$ in the PAN/DMF solution results in significant decrease in the beads on the fiber. Using this approach, nearly bead free fibers of 60 nm diameter were obtained.
- The PAN crystallite size in all the electrospun fiber mats was about 3 nm, while in solution cast films was in the range of 5 to 6 nm. Electrospinning process hinders polymer crystallization.
- Compared to SWNT powder and PAN/SWNT film, an up-shift of G and G' bands was observed in Raman spectra of electrospun PAN/SWNT fiber mats, suggesting stronger compressive force on SWNT bundles during electrospinning than observed in cast films.
- High speed photography was used to study the electrospinning process. Branching was observed when electrospinning low concentration PAN solution or PAN/CNT dispersions.

2.5 References

1. A. Chambers, C. Park, R. T. K. Baker, and N. M. Rodriguez, the Journal of Physical Chemistry B, **1998**, 102, 4253

2 . R. Ströbel, L. Jörissen, T. Schliermann, V. Trapp, W. Schütz, K. Bohmhammel, G. Wolf, and J. Garche, Journal of Power Sources, **1999**, 84, 221.

3. T. Wang and S. Kumar, to be published.

4. C. Kim and K. S. Yang, Applied Physics Letters, **2003**, 83, 1216.

5. M. L. Toebes, F. F. Prinsloo, J. H. Bitter, A. J. van Dillen, and K. P. de Jong, Journal of Catalysis, **2003**, 214, 78.

6. C. Park and R. T. K. Baker**,** the Journal of Physical Chemistry B, **1998**, 102, 5168.

7. K. Lozano and E. V. Barrera, Journal of Applied Polymer Science, **2001**, 79, 125.

8. B. D. Cullity, Elements of X-ray Diffraction. 2nd ed. Reading, MA: Addison-Wesley Publishing Company, **1978**.

9. P. G. De Gennes, Scaling Concepts in Polymer Physics, Cornell University Press, Ithaca, NY, **1979**.

10. M. G. Mckee, G. L. Wilkes, R. H. Colby, and T. E. Long, Macromolecules, **2004**, 37, 1760.

11. P. Gupta, C. Elkins, T. E. Long, and G. L. Wilkes, Polymer, **2005**, 46, 4799.

12. R. H. Colby, L. H. Fetters, W. G. Funk, and W. W. Graessley, Macromolecules, **1991**, 24, 3873.

13. R. H. Colby and M. Rubinstein, Macromolecules, **1990**, 23, 2753.

14. J. M. Deitzel, J. Kleinmeyer, D. Harris, and N. C. Beck Tan, Polymer, **2001**, 42, 261.

15. M. M. Demir, I. Yilgor, E. Yilgor, and B. Erman, Polymer, **2002**, 43, 3303.

16. G. E. Wnek, M. E. Carr, D. G. Simpson, and G. L. Bowlin, Nano Letters, **2003**, 3, 213.

17. C. M. Uppatham, M. Nithitanakul, and P. Supaphol, Macromolecular Chemistry and Physics, **2004**, 205, 2327.

18. Q. Yang, Z. Li, Y. Hong, Y. Zhao, S. Qiu, C. Wang, and Y. Wei, Journal of Polymer Science, Part B: Polymer Physics, **2004**, 42, 3721.

19. X. Yuan, Y. Zhang, C. Dong, and J. Sheng, Polymer International, **2004**, 53,

1704.

20. J. B. Christopher, L. C. Chen, Y. Shen, and D. C. Martin, Polymer, **1999**, 40, 7397.

21. S. A. Theron, E. Zussman, and A. L. Yarin, Polymer, **2004**, 45, 2017.

22. T. V. Sreekumar and S. Kumar, US patent, **2005**, 6, 852, 410.

23. J. Brandrup, E. H. Immergut, E. A. Grulke, Polymer Handbook, John Wiley & Sons, 4th edition, New York, NY, **1999**.

24. G. Wypych, Handbook of Solvents, ChemTec Publishing, Ontario, Canada, **2001**.

25. J. Liu and S. Kumar, Polymer Communication, **2005**, 46, 3211.

26. Y. You, S. J. Lee, B. M. Min, and W. H. Park, Journal of Applied Polymer Science, **2006**, 99, 1214.

27. B. E. Conway, Electrochemical Capacitors, Scientific Fundamental and Technological Applications, Plenum Publishers, **1999**.

28. M. Bognitzki, M. Czado, T. Frese, A. Schaper, M. Hellwig, M. Steinhart, A. Greiner, and J. H. Wendorff, Advanced Materials, **2001**, 13, 70.

29. S. Megelski, J. S. Stephens, D. B. Chase, and J. F. Rabolt, Macromolecules, **2002**, 35, 8456.

30. A. Koski, K. Yim, and S. Shivkumar, Materials Letters, **2004**, 58, 493.

31. K. H. Lee, H. Y. Kim, H. J. Bang, Y. H. Jung, and S. G. Lee, Polymer, **2003**, 44, 4029.

32. M. Cloupeau and B. P. Foch, Journal of Electrostatics, **1989**, 22, 135.

33. V. Pornsopone, P. Supaphol, R. Rangkupan, and S. Tantayanon, Polymer Engineering and Science, **2005**, 45, 1073.

34. J. H. Yu, S. V. Fridrikh, and G. C. Rutledge, Polymer, **2006**, 47, 4789.

35. H. Fong, I. Chun, and D. H. Reneker, Polymer, **1999**, 40, 4585.

36. T. Jarusuwannapoom, W. Hongrojjanawiwat, S. Jitjacham, L. Wannatong, M. Nithitanakul, C. Pattamaprom, P. Koombhongse, R. Rangkupan, and P. Supaphol, European Polymer Journal, **2005**, 41, 409.

37. A. Ziabicki, Fundamentals of Fiber Formation: the Science of Fiber Spinning and Drawing, A Wiley-Interscience Publication, John Wiley & Sons, **1976**.

38. R. V. N. Krishnappa, K. Desai, and C. Sung, Journal of Materials Science, **2003**,

38, 2357.

39. S. Shukla, E. Brinley, H. J. Cho, and S. Seal, Polymer, **2005**, 46, 12130.

40. W. Zuo, M. Zhu, W. Yang, H. Yu, Y. Chen, and Y. Zhang, Polymer Engineering and Science, **2005**, 45, 704.

41. C. M. Hsu and S. Shivkumar, Journal of Materials Science, **2004**, 39, 3003.

42. K. H. Lee, H. Y. Kim, M. S. Khil, Y. M. Ra, and D. R. Lee, Polymer, **2003**, 44, 1287.

43. L. Wannatong, A. Sirivat, and P. Supaphol, Polymer International, **2004**, 53, 1851.

44. C. L. Yaws, Yaws' Handbook of Thermodynamic and Physical Properties of Chemical Compounds, **2003**, Knovel.

45. S. J. Kim, C. K. Lee, and S. I. Kim, Journal of Applied Polymer Science, **2005**, 96, 1388.

46. X. Zong, K. Kim, D. Fang, S. Ran, B. S. Hsiao, and B. Chu, Polymer, **2002**, 43, 4403.

47. J. Liu, Private communication.

48. C. Shao, H. Y. Kim, J. Gong, B. Ding, D. R. Lee, and S. J. Park, Materials Letters, **2003**, 57, 1579.

49. A. R. Hoskins, H. G. M. Edwards, and A. F. Johnson, Polymer Communication, **1991**, 32, 89.

50. H. G. M. Edwards, A.R. Hoskins, A. F. Johnson, and I. R. Lewis, Polymer International, **1993,** 30, 25.

51. S. H. Cho, J. S. Park, S. M. Jo, and I. J. Chung, Polymer International, **1994,** 34, 333.

52. M. A. Phadke, D. A. Musale, S. S. Kulkarni, S. K. Karode, Journal of Polymer Science: Part B: Polymer Physics, **2005,** 43, 2061.

53. R. Jalili, M. Morshed, S. A. H. Ravandi, Journal of Applied Polymer Science, **2006**, 101, 4350.

54. C. A. Cooper, R. J. Young, and M. Halsall, Composite: Part A, Applied Science and Manufacturing, **2001**, 32, 401.

55. P. Dharad, Z. Li, S. Nagarajaiah, and E. V. Barrera, Nanotechnology, **2004**, 15, 379.

56. F. Huang, K. T. Yue, P. Tan, S. L. Zhang, Z. Shi, X. Zhou, and Z. Gu, Journal of Applied Physics, **1998**, 84, 4022.

57. U. D. Venkateswaran, M. É. Gosselin, B. Postek, D. L. Masica, G. Chen, R. Gupta, and P. C. Eklund, Physical Status Solidi, B: Basic Research, **2003**, 235, 364.

58. J. Liu, T. Wang, T. Uchida, and S. Kumar, Journal of Applied Polymer Science, **2005**, 96, 1992.

59. D. H. Reneker, A. L. Yarin, H. Fong, and S. Koombhongse, Journal of Applied Physics, **2000**, 87, 4531.

60. M. M. Hohman, M. Shin, G. Rutledge, and M. P. Brenner, Physics of Fluids, **2001**, 13, 2221.

61. K. Tang and A. Gomez, Journal of Colloid and Interface Science, **1995**, 175, 326.

62. A. L. Yarin, S. Koombhongse, and D. H. Reneker, Journal of Applied Physics, **2001**, 90, 4836.

63. A. M. Gañán-Calvo, Physical Review Letters, **1997**, 79, 217.

64. J. S. Eow and M. Ghadiri, Colloids and Surfaces A: Physicochemical Engineering Aspects, **2003**, 215, 101.

65. S. Koombhongse, W. Liu, and D. H. Reneker, Journal of Polymer Science: Part B: Polymer Physics, **2001**, 39, 2598.

66. A. L. Yarin, W. Kataphinan, and D. H. Reneker, Journal of Applied Physics, **2005**, 98, 064501.

CHAPTER 3

ELECTROCHEMICAL CAPACITOR BEHAVIOR OF CARBON NANOFIBERS

3.1 Introduction

In this chapter stabilization and carbonization studies of various fiber mats as well as their characterization as electrochemical capacitor electrode are reported. The effects of fiber diameter, CO_2 activation, the presence of sacrificial component, poly(styrene-co-acrylonitrile)(SAN), and addition of carbon nanotubes on capacitor performance are investigated. The capacitance performance is correlated with surface area and pore size distribution. The role of sacrificial component SAN is to increase mesoporosity. PAN and SAN are immiscible polymers with different thermal stability. During carbonization, PAN is converted into carbon, while SAN burns out, leaving the pores in the fibers. Therefore, the addition of SAN is expected to result in increased porosity. This should result in high capacitance at high current density. Power density of an electrochemical capacitor depends on the internal resistance of the electrode and the electrolyte as well as the contact resistance between the electrode and the current collector.[1] Carbon nanotubes have high electrical conductivity and can significantly improve electrical conductivity when they are incorporated into the polymer matrix. Single wall carbon nanotubes (SWNTs) and multi wall carbon nanotubes (MWNTs) have been added in PAN and PAN/SAN, to improve the electrical conductivity and hence power density.

3.2 Experimental

3.2.1 Characterization of carbon nanotubes

SWNT (containing 6 wt% impurity, received from Carbon Nanotechnologies Inc., Houston, TX), DWNT (double wall carbon nanotubes from Nanocyl Co., Belgium), and MWNT (from Iljin Nanotech Co., Ltd, Seoul, Korea) were used in this study.

3.2.2 Processing of various fiber mats and films

Solution of PAN (containing less than 5 % itaconic acid and methacrylate copolymer, from Enichem Solution Corp) and SAN (25 wt% acrylonitrile and 75 wt% styrene random copolymer, MW 165,000 g/mole, from ACROS Organics, New Jersey) in dimethylformamide (DMF, Fisher Scientific, Pittsburgh, PA) was prepared in the desired PAN/SAN ratio (90/10, 80/20, 70/30, and 50/50) in 30 ml DMF. All PAN/SAN fiber mats were electrospun at a polymer concentration of 18 wt%, at 22 kV, using an 18 gauge needle, at a needle tip to target distance of 10 cm, and the flow rate was 1 ml/h.

To make PAN/SAN/SWNT(80/20/1 wt%) dispersion, about 24 mg SWNT was first dispersed in 300 ml DMF and sonicated in a bath sonicator (Cole–Parmer 8891R-DTH, 80 W, 43 kHz, Vernon Hills, IL) for 24 hrs. To this SWNT/DMF dispersion, 1.9 g PAN and 0.48 g SAN powder (the ratio of PAN to SAN was 80/20) were added and dissolved by high speed stirring until the homogenous dispersion was obtained. Then the excess DMF was removed by heating and stirring, and about 20 ml dispersion with solid content of 12 wt% was obtained. Following the same procedure, 20 ml PAN/SAN/SWNT (80/20/3 wt%) dispersion with solid content of 12 wt% was prepared by adding 72 mg SWNT, 1.86 g PAN, and 0.47 g SAN into DMF.

To make PAN/MWNT (95/5) dispersion, about 100 mg MWNT was first dispersed in 300 ml DMF by sonicating in a bath sonicator for 24 hrs followed by horn sonication (Model 2020, Misonix Inc., Farmingdale, NY) for 30 min. To this MWNT/DMF dispersion, 1.9 g PAN powder was added and dissolved by high speed stirring until the homogenous dispersion was obtained. Then the excess DMF was removed by heating and stirring, and 20 ml PAN/MWNT dispersion with solid content of 10 wt% was obtained. Following the same procedure, 20 ml PAN/MWNT dispersions in the 90/10, 80/20, and 70/30 weight ratio with 10 wt% solid content were prepared.

The PAN and PAN/SAN solutions as well as PAN/carbon nanotube dispersions were electrospun as described in Chapter 2. For all the fiber mats used for processing electrochemical capacitors, the electrospinning conditions were kept constant: the solution flow rate was 1 ml/hr, the distance between the needle tip and the target was 10 cm, and the voltage was 22 kV.

In order to prepare PAN/SAN (70/30) film, the 10 ml PAN/SAN (70/30) solution with concentration of 5 wt% was poured into a petri dish and evaporated in air at room temperature for one week.

3.2.3 SWNT and DWNT bucky papers

SWNT bucky paper (HiPCO^{TM}) was supplied by Carbon Nanotechnologies, Inc. (CNI, Houston, TX) with the thickness of 70 μm. To prepare DWNT bucky paper, 50 mg DWNT was dispersed into 150 ml DMF, and then sonicated in a bath sonicator (Cole–Parmer 8891R-DTH, 80 W, 43 kHz, Vernon Hills, IL) for 24 hrs followed by filtration through poly(tetrafluoroethylene) (PTFE) filter paper (1.0 μm pore size, Pall Gelman Laboratory, East Hills, NY) under water pump pressure. The

resulting bucky paper was peeled off from the filter paper and vacuum dried at 70 °C for four days. The thickness of this DWNT bucky paper was about 60 μm.

3.2.4 Activated carbon pellet

800 mg activated carbon powder M20 (Spectracorp, Lawrence, MA) and 200 mg poly(vinylidene fluoride) (PVDF) purchased from Aldrich (Milwaukee, WI) were dispersed into 10 ml DMF by stirring. This paste was pressed into 1 mm thick disc using laboratory press (Model 3912, Fred S. Carver Inc., Menomonee Falls, WI). The resulting pellets were vacuum dried at 70 °C for four days. The thickness of the dried activated carbon pellet was about 0.68 mm.

3.2.5 Heat treatment of electrospun fiber mats

Various fiber mats were stabilized in a box furnace (51668-HR Box Furnace 1200C, Blue M Electric, Asheville, NC) at a heating rate of 1 °C/min up to 250 °C and held at that temperature for 2 hrs in air. The stabilized fiber mats were subsequently carbonized at a heating rate of 5 °C/min up to 900 °C and held at that temperature for 30 min under argon flow. The carbonized PAN fiber mats were thus obtained. To activate the fiber mats, the carbonized PAN fiber mats were further held at 900 °C for 30 min under CO_2 flow.

3.2.6 Characterization of fiber mats

Fiber mats were gold-coated and observed by scanning electron microscopy (SEM) (LEO 1530, Osaka, Japan) at 15 kV. Energy Dispersive X-Ray Spectroscopy (EDX) of the carbonized PAN fiber mats and activated PAN fiber mats was conducted on LEO 1530 at 10 kV. Thermogravimetric analysis (TGA) of PAN and

SAN powder was conducted on a TGA model (TA instruments, New Castle, DE) at a heating rate of 5 °C/min from 25 to 800 °C in N_2. The contact angles between various carbon materials and 6M KOH solutions were measured on VCA Optima contact angle analysis system (AST Products, Inc., Billerica, MA). In plane dc electrical conductivity was measured by four-probe method.

3.2.7 Capacitance and impedance measurement

The capacitance, power density and energy density measurements of the electrochemical capacitors were conducted on Solartron 1470 cell test station (Solartron Analytical, Houston, TX) using 6 M KOH aqueous electrolyte. The schematic sketch of the two-electrode cell is given in Figure 3.1. Two circular shape electrodes with diameter of 1.27 cm separated by microporous membrane with pore size of 0.117 μm × 0.042 μm (Celgard 3400, Celgard Inc., Charlotte, NC) were sandwiched between nickel current collectors. In the constant current (CC) charge/discharge measurement, the cell was charged and discharged between 0 and 0.8 V at a current of 0.5, 1, 5, and 10 mA. All the constant current charge/discharge plots are documented in Appendix C. In the cyclic voltammetry (CV) measurement, scan rates of 5, 10, 20, and 50 mV/s were used.

Specific capacitance, power density, and energy density were calculated by using the following equations:[2]

$$C_{sp} = \frac{I}{dV(t)/dt}\left(\frac{1}{m_A} + \frac{1}{m_B}\right)$$

$$PD = IV(t)/(m_A+m_B)$$

$$ED = \int_{t=0}^{t} IV(t)dt/(m_A + m_B)$$

where C_{sp} is specific capacitance; PD is power density; ED is energy density; V(t) is potential; I is current; m_A and m_B are the masses of the two electrodes.

Current density (current per unit mass) can be represented by:

$$\text{Current density} = I\left(\frac{1}{m_A} + \frac{1}{m_B}\right) = C_{sp} \cdot (dV(t)/dt) = C_{sp} \cdot s$$

where s is the scan rate.

The impedance analysis of the electrochemical capacitors was conducted on Solartron 1255B Frequency Response Analyzer (Solartron, Houston, TX). A 0.05 V AC perturbation was used in the impedance measurements over a frequency range of 100 kHz to 50 mHz.

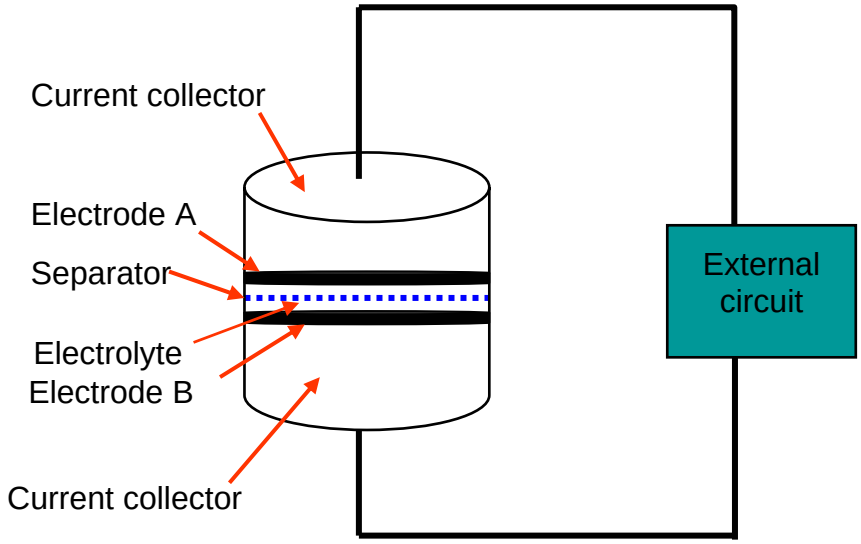

Figure 3.1. Schematic sketch of the electrochemical capacitor test cell.

3.2.8 Surface area and pore size measurement

To measure the surface area and porosity, samples were degassed at 90 °C for 16 hrs at a pressure of 1×10^{-4} Pa. The isothermal N_2 gas adsorption and desorption studies at 77 K were carried out on ASAP 2020 (Micromeritics Instrument Corporation, Norcross, GA). The quantity of gas (V) absorbed or released at 77 K was measured as

a function of gas pressure (P). The pore size distribution was evaluated by using the density functional theory (DFT).[3] The specific surface area was evaluated by using Brunauer–Emmett–Teller (BET)[4] and DFT[3] theories. All the isothermal adsorption and desorption plots are documented in Appendix B.

3.3 Results and Discussion

3.3.1 Characterization of various carbon nanotubes

The TEM images of various carbon nanotubes given in Figure 3.2, show that the SWNT forms about 30 nm diameter bundles, while DWNT and MWNT mostly exist individually with diameter of 5 and 20 nm, respectively. The TGA plots given in Figure 3.3 show that SWNT, DWNT, and MWNT degrade at about 500, 440, and 600 °C in air, respectively. The Raman spectra (Figure 3.4**)** show that the disorder band (D band, about 1300 cm^{-1}) of MWNT is the highest among three kinds of carbon nanotubes, indicating highly defective graphitic structure.

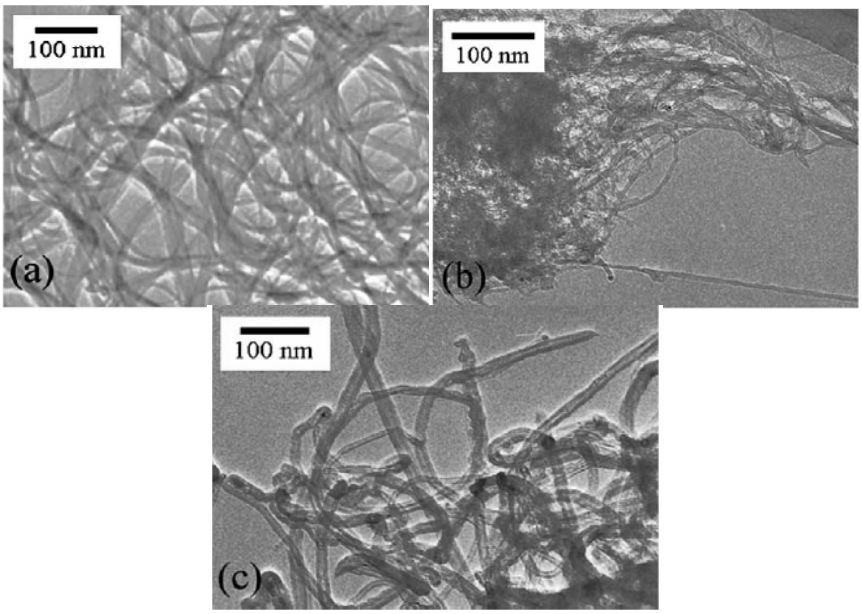

Figure 3.2. Transmission electron micrographs of (a) SWNT, (b) DWNT, and (c) MWNT. (From ref. 5.)

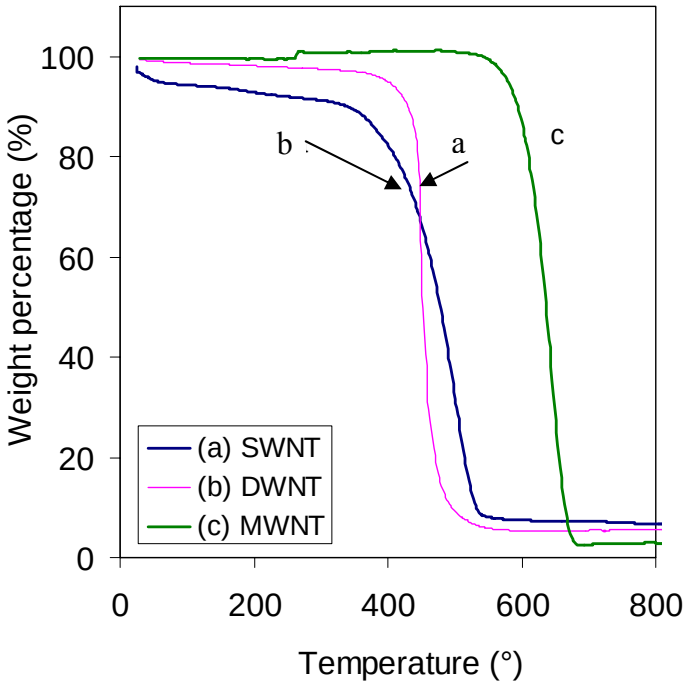

Figure 3.3. Thermogravimetric analysis plots of (a) SWNT, (b) DWNT, and (c) MWNT at a heating rate of 10 °C/min in air. (From ref. 5.)

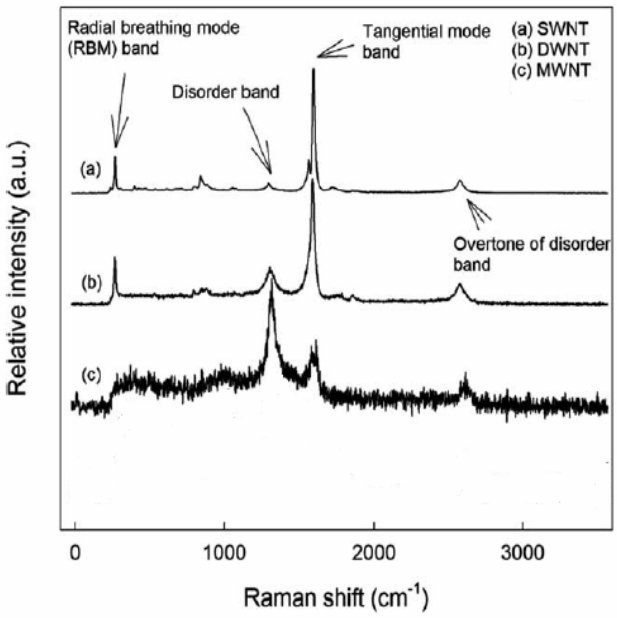

Figure 3.4. Raman spectra of various carbon nanotubes. (From ref. 5.)

3.3.2 Effect of fiber diameter on electrochemical capacitor performance

Fiber diameter affects surface area and pore size distribution, which ultimately influences the electrochemical capacitor performance. In this work, the effect of fiber diameter on electrochemical capacitor performance was studied. The electrospun fibers mats with diameters of 100, 200, and 400 nm were stabilized, carbonized, and processed into electrochemical capacitor electrodes. The fiber mats show about 30 % area shrinkage after carbonization without significant change in fiber diameter. The fiber mat of 100 nm diameter has many beads and is densely packed, while the fiber mats of 200 and 400 nm diameters have relatively loose packing (Figure 3.5). The density for each carbonized PAN fiber mat was determined by dividing the sample weight by the sample volume (sample volume = fiber mat area × thickness). The carbon residue for each fiber mat was also determined by weighing the fiber mat before and after carbonization. The results are given in Table 3.1

Table 3.1. Carbon residue and density of the carbonized PAN fiber mats.

Fiber diameter (nm)	**Carbon residue (wt%)**	**Density (g/cm^3)**
100	49.7	0.41 ± 0.08
200	44.8	0.37 ± 0.05
400	46.3	0.37 ± 0.04

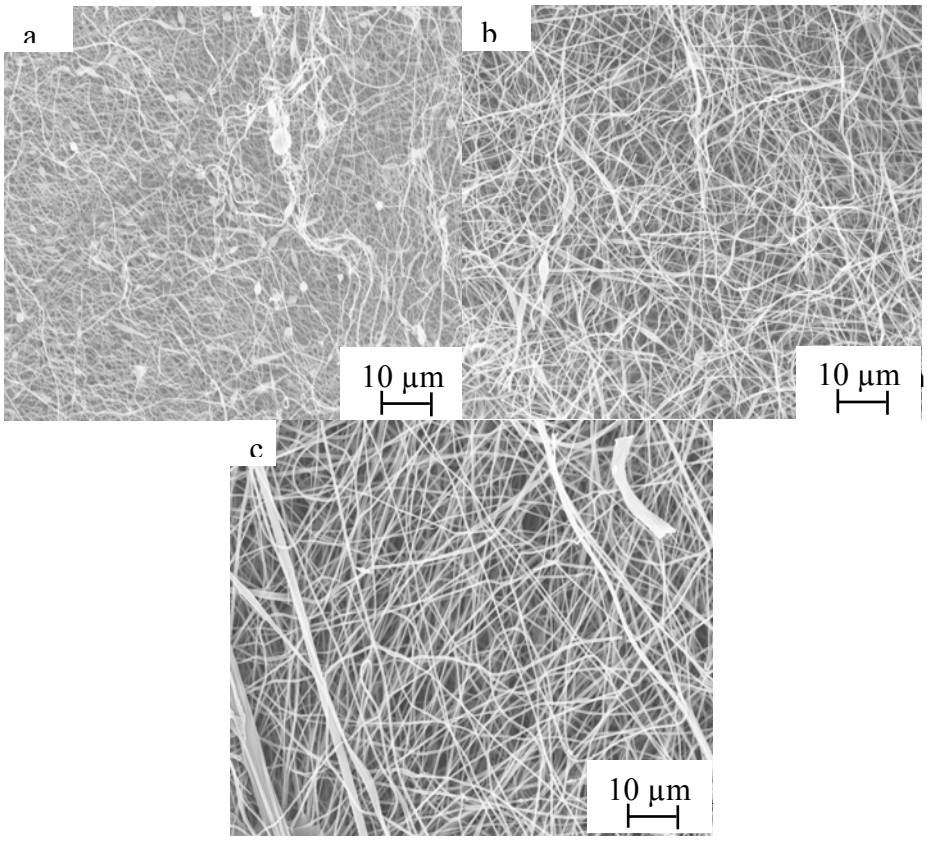

Figure 3.5. Scanning electron micrographs of carbonized PAN fibers with diameter of (a) 100 nm, (b), 200 nm, and (c) 400 nm.

The BET surface area and DFT volume of the pristine PAN and carbonized PAN fiber mats were measured, and the results are given in Table 3.2 and 3.3, respectively. It shows that the surface area of pristine PAN fiber mat is quite low without stabilization and carbonization. After carbonization, the surface area significantly increases. For all the carbonized PAN fiber mats, BET surface area values are significantly higher than their DFT surface area values. Higher BET surface area was also reported in other research work.[6, 7, 8] The difference in BET and DFT surface area are due to their different assumptions for calculating the surface area. In BET model, it assumes that the surface is covered by multilayer gas molecules, while DFT theory reveals the pore structures filled by the gas molecules.[3] Therefore, BET surface area is different from DFT surface area. The theoretical

specific surface area of a fiber can also be calculated assuming a cylindrical solid fiber with smooth surface by using the following equation:

$$S = 4/(\rho d)$$

where S is the specific surface area, ρ is density, and d is fiber diameter. For all the samples, the theoretical surface area is much lower than BET or DFT surface area. When calculating theoretical surface area, the fiber is assumed to be solid. In reality, after carbonization, the surface of the fiber become rough and small pores reside inside the fiber, resulting in much higher BET and DFT surface areas.

Table 3.2. Surface area and pore volume of 200 nm diameter pristine PAN fiber mat without stabilization and carbonization.

Sample		**200 nm diameter**
S_{BET} (m^2/g)		11
S_{DFT} (m^2/g)		6
DFT pore volume (cm^3/g)	V_{micro}	0.001
	V_{meso}	0.026
	V_{macro}	0.018
	V_{total}	0.045

Table 3.3. Specific capacitance, surface area, pore volume, and double layer capacity of the carbonized PAN fiber mats of different fiber diameters.

Sample		**100 nm diameter**	**200 nm diameter**	**400 nm diameter**
Theoretical surface area of carbon fiber (m^2/g)*		24	12	6
S_{BET} (m^2/g)		494	268	140
S_{DFT} (m^2/g)		42	39	20
DFT pore volume (cm^3/g)	V_{micro}	0.025	0.021	0.015
	V_{meso}	0.011	0.005	0.038
	V_{macro}	0.004	0.008	0.009
	V_{total}	0.040	0.034	0.062
Specific capacitance (F/g, 1 mA charge/discharge, at 0.1 V)		58	165	115
BET double layer capacity ($\mu F/cm^2$)		12	62	82

*For surface area calculation, ρ for carbon fiber was assumed to be 1.7 g/cm^3.

The pore size distribution of the pristine PAN and carbonized PAN fiber mats is given in Figure 3.6. It shows that pristine PAN fiber mat has very small micropores, resulting in low surface area. With carbonization, micropore volume increases. The micropores are dominant in the carbonized PAN nanofibers with diameters of 100 and 200 nm, while mesopores become dominant in the carbonized PAN nanofibers with 400 nm diameter. The micropores mostly reside inside or on the surface of the carbonized PAN nanofibers, while the macropores are present between the entangled nanofibers. In the carbonized PAN nanofibers with diameter of 100 nm, the dense packing (Figure 3.5 (a)) results in small macropores. On the other hand, 200 and 400 nm diameter fiber mats (Figure 3.5 (b) and (c)) result in relatively larger macropores.

The specific capacitance of the carbonized PAN fiber mats is plotted as a function of current density in Figure 3.7. For all the fiber mats, the capacitance decreases with increasing current density due to the difficulty of the electrolyte ions accessing small pores at high current density. At low charge/discharge current density, the electrolyte ions move slowly and have sufficient time to access most of small pores, resulting in high capacitance. At high charge/discharge current density, the electrolyte ions move rather fast and do not have sufficient time to access all the small pores, resulting in low capacitance.

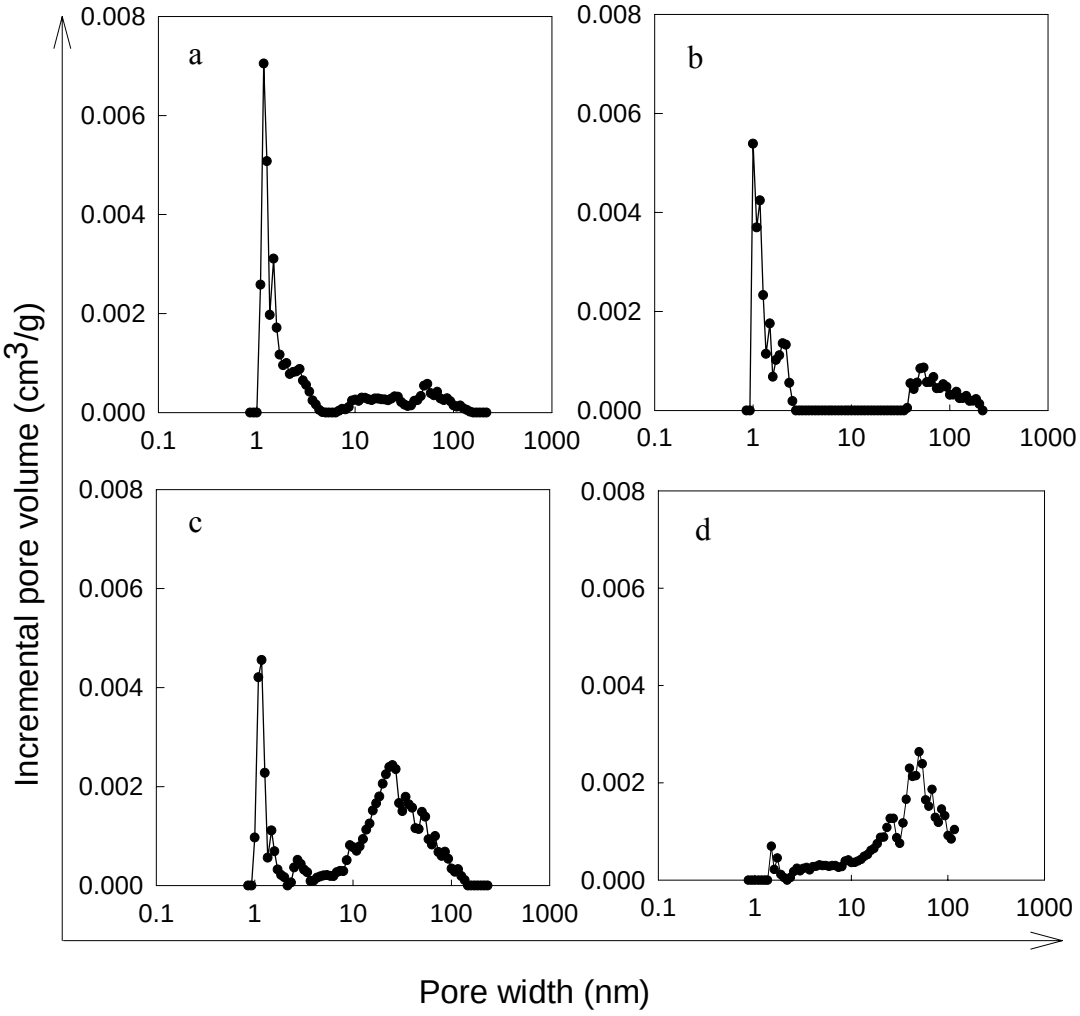

Figure 3.6. Pore size distribution of carbonized PAN nanofibers with diameter of (a) 100 nm, (b) 200 nm, and (c) 400 nm, and (d) pore size distribution of 200 nm diameter pristine PAN fiber mat without stabilization and carbonization.

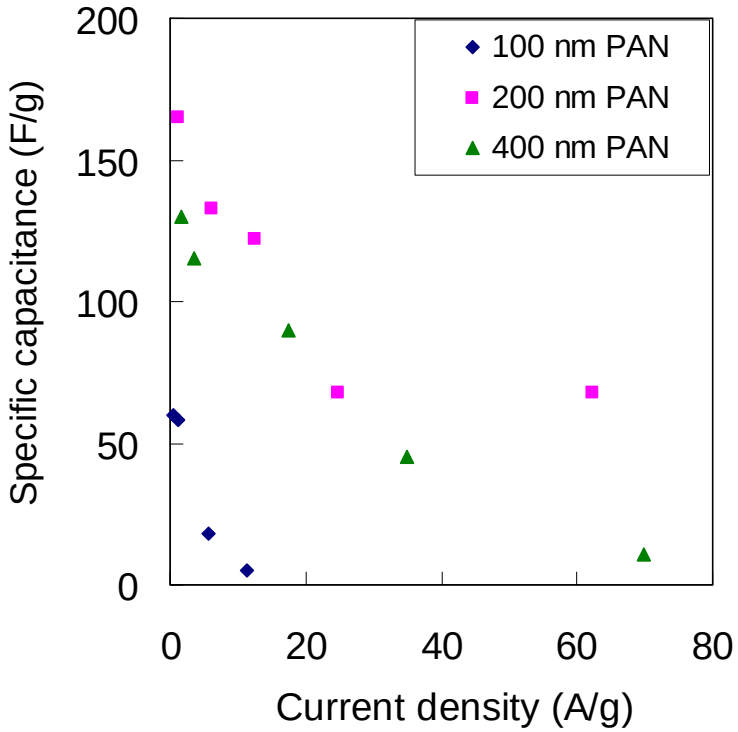

Figure 3.7. Specific capacitance as a function of current density for various electrospun fibers. 100 nm PAN (1.90 mg-1.63 mg), 200 nm PAN (1.34 mg-2.01 mg), and 400 nm PAN (0.71 mg-0.48 mg). The numbers in brackets represent the masses of the electrodes used for capacitance testing.

Figure 3.7 also shows that the carbonized PAN fiber mat of 100 nm diameter has lower capacitance than those of 200 and 400 nm diameter fiber mats. Macropores are reported to play an important role in electrochemical capacitor performance.[8] The high macropore volume in the carbonized PAN nanofibers with diameter of 200 and 400 nm in the current work may be responsible for their high capacitance performance.

3.3.3 Solid or porous PAN nanofibers based electrochemical capacitors

In this section, the electrochemical performance of solid and porous PAN nanofibers based electrochemical capacitors was compared. The solid PAN/$ZnCl_2$ nanofibers with diameter of 60 nm (Figure 2.19 (e)) and porous PAN nanofibers with

diameter of 600 nm (Figures 2.11 (f)) were stabilized, carbonized, and processed into electrochemical capacitor electrodes. The SEM images of these nanofibers after carbonization are given in Figure 3.8, showing that the shallow pores are present on the surface of the carbonized porous fibers.

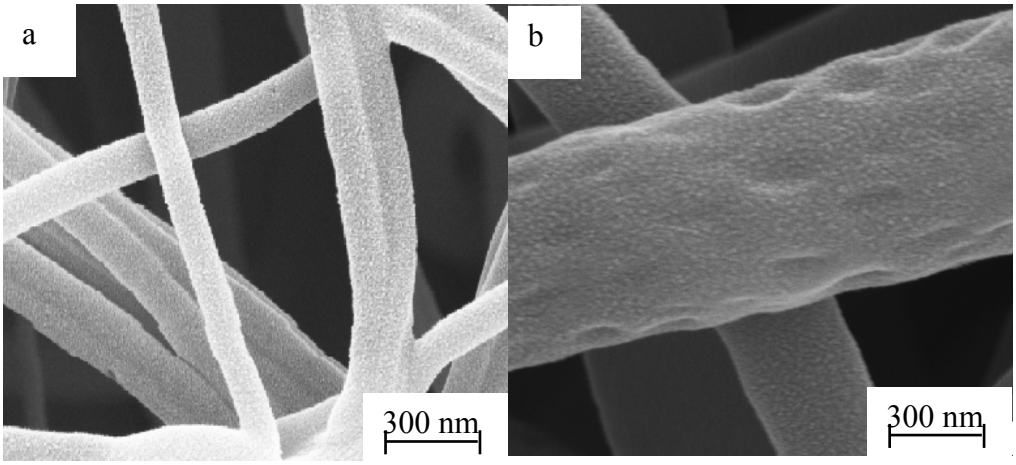

Figure 3.8. Scanning electron micrographs of carbonized (a) 60 nm PAN/$ZnCl_2$ fibers and (b) 600 nm porous PAN fibers.

The specific capacitance of the carbonized solid or porous PAN nanofibers is plotted as a function of current density in Figure 3.9. It shows that 600 nm PAN porous nanofibers have comparable capacitance with 60 nm PAN/$ZnCl_2$ solid nanofibers. The pore size distribution of these two fiber mats is plotted in Figure 3.10 and their surface area and DFT pore volume are given in Table 3.4. Figure 3.10 shows that both solid and porous nanofibers exhibit similar pore size distribution with micropore domination. Compared to the porous PAN nanofibers, the solid PAN/$ZnCl_2$ nanofibers have slightly larger surface area because of their small fiber diameter and presence of $ZnCl_2$. $ZnCl_2$ can act as chemical activation agent, which would increase the surface area.[9] The similar pore size distribution and pore volume

are responsible for the similar capacitance values in the solid and porous PAN nanofibers of significantly different diameters.

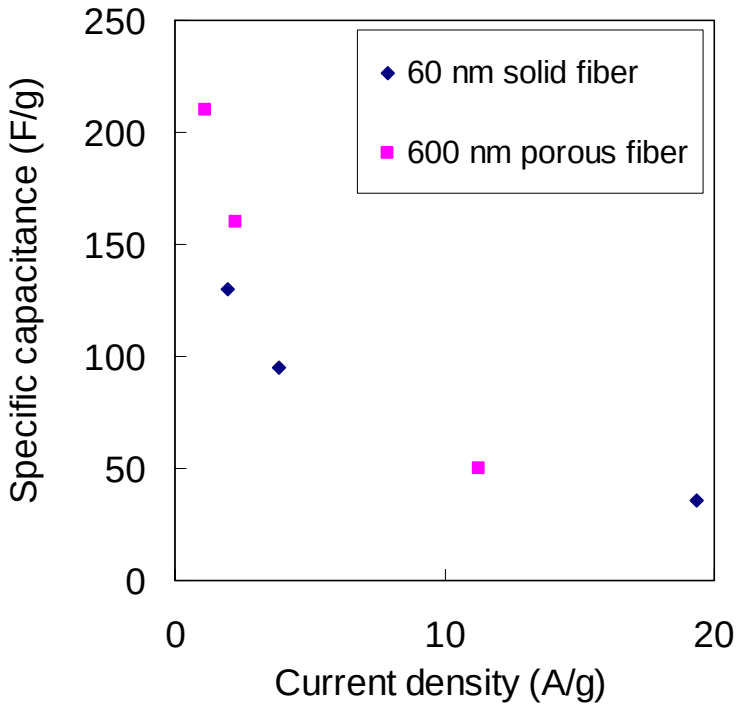

Figure 3.9. Specific capacitance as a function of current density for 60 nm solid fiber(0.42 mg-0.67 mg) and 600 nm porous fiber(0.94 mg-0.84 mg).

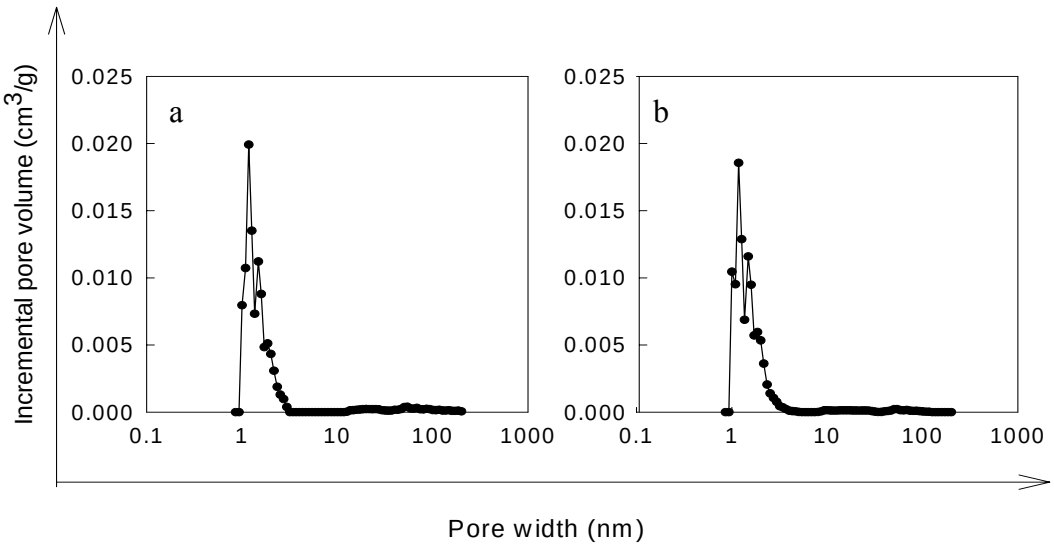

Figure 3.10. Pore size distribution of carbonized (a) 60 nm solid PAN/$ZnCl_2$ fibers and (b) 600 nm porous PAN fibers

Table 3.4. Specific capacitance, surface area, pore volume, and double layer capacity of carbonized solid and porous PAN fibers.

Sample		**60 nm PAN/$ZnCl_2$ solid nanofibers**	**600 nm PAN porous nanofibers**
Theoretical surface area of carbon fiber (m^2/g)*		39	4
S_{BET} (m^2/g)		645	583
S_{DFT} (m^2/g)		150	155
DFT pore volume (cm^3/g)	V_{micro}	0.089	0.091
	V_{meso}	0.015	0.018
	V_{macro}	0.004	0.001
	V_{total}	0.108	0.110
Specific capacitance (F/g, 1 mA charge/discharge, at 0.1 V)		95	160
BET double layer capacity ($\mu F/cm^2$)		15	27

* For carbon fiber, ρ was assumed to be 1.7 g/cm^3.

3.3.4 Effect of activation on performance of PAN fiber mat based electrochemical capacitor

With activation by CO_2, steam, or chemical agents, the surface chemistry and porosity of graphite change, [10, 11] which may affect electrochemical capacitor performance. In this work, PAN nanofibers of 200 nm diameter were stabilized, and further carbonized or activated by CO_2, and their electrochemical performance was compared. Figure 3.11 shows the SEM images of the carbonized PAN and the activated PAN fiber mats. After activation, the surface of nanofibers becomes coarse, which may come from the etching effect of CO_2.

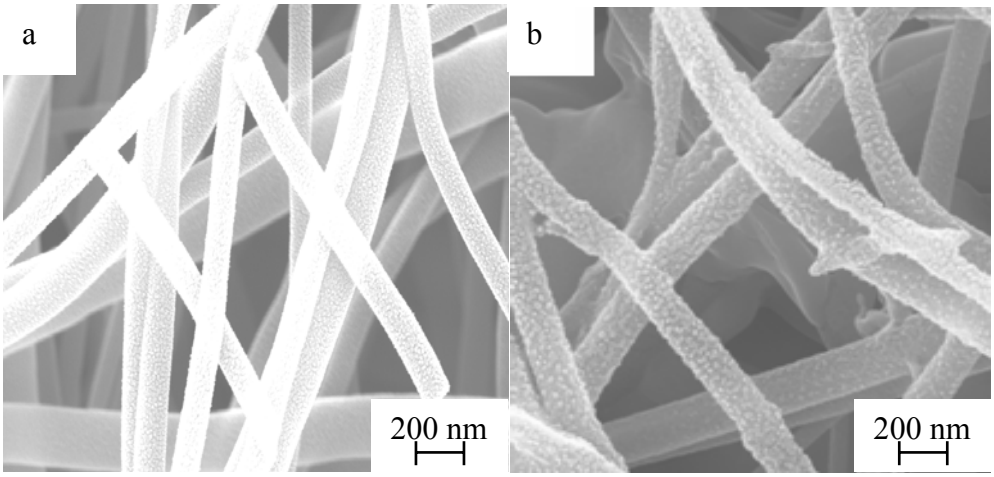

Figure 3.11. Scanning electron micrographs of (a) carbonized PAN and (b) activated PAN fiber mats.

The pore size distribution of the activated PAN fiber mat is plotted in Figure 3.12. The specific capacitance, surface area and pore volume of the carbonized PAN fiber mat and the activated PAN fiber mat are given in Table 3.5. It shows that micropores are dominant in both carbonized and activated PAN fiber mats. With activation, BET surface area, micropore and mesopore volumes increase.

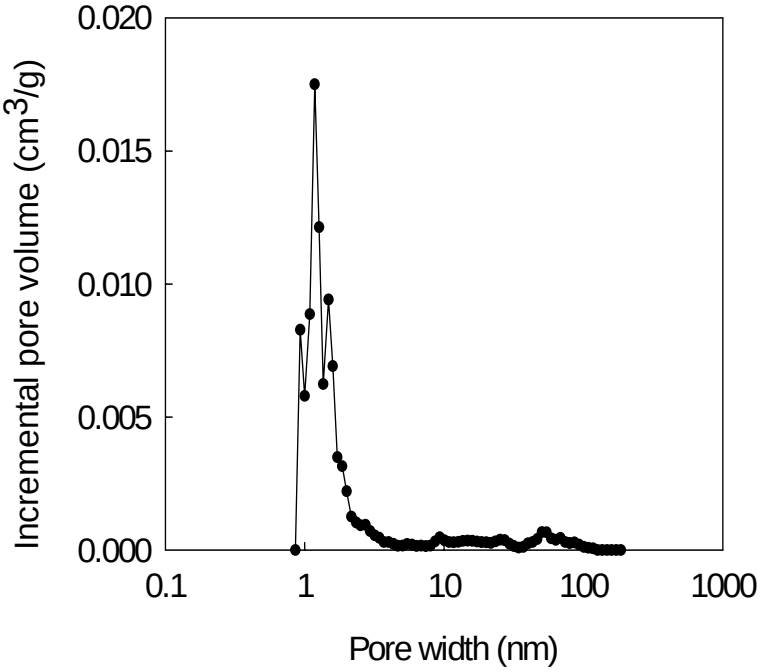

Figure 3.12. Pore size distribution of activated PAN fiber mat.

Table 3.5. Specific capacitance, surface area, pore volume, and double layer capacity of carbonized and activated PAN fiber mats.

Sample		**Carbonized PAN**	**Activated PAN**
S_{BET} (m^2/g)		268	730
S_{DFT} (m^2/g)		39	142
DFT pore volume (cm^3/g)	V_{micro}	0.021	0.081
	V_{meso}	0.005	0.017
	V_{macro}	0.008	0.004
	V_{total}	0.034	0.102
Specific capacitance (F/g, 1 mA charge/discharge, at 0.1 V)		165	165
BET double layer capacity ($\mu F/cm^2$)		62	23

The specific capacitance of the carbonized PAN and the activated PAN fiber mat is plotted as a function of current density in Figure 3.13. When the activated PAN fiber mat was charged/discharged from low to high current density, its specific capacitance is higher than that of the carbonized PAN fiber mat by 35 F/g at low current density, while the specific capacitance becomes lower than that of the carbonized PAN with increasing current density. On the other hand, when the activated PAN fiber mat was charged/discharged from high to low current density, the trend was reversed. The capacitance of the activated PAN is lower than that of the carbonized PAN at low current density but higher at high current density.

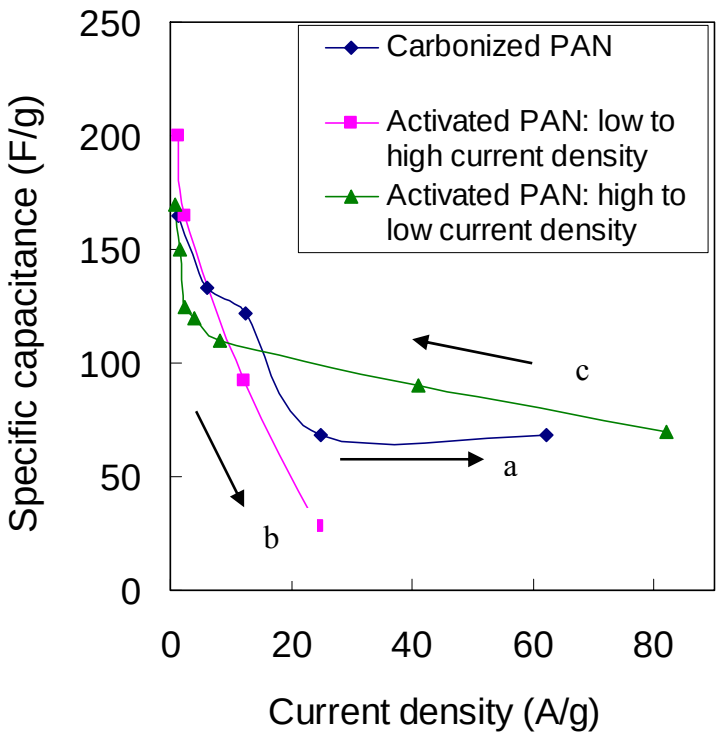

Figure 3.13. Specific capacitance as a function of current density for (a) carbonized PAN(1.34mg-2.01 mg), (b) activated PAN(0.80 mg-0.85 mg), and (c) activated PAN(0.23 mg-0.26 mg). Arrows indicate testing direction.

The high micropore volume in the activated PAN fiber mat may be responsible for its high capacitance at low current density; however, it cannot explain why the activated PAN has lower capacitance at high current density since it also has higher mesopore volume. The large pores, such as mesopores can help to maintain high capacitance at high current density.[12] Therefore, it is expected that the activated PAN should still have higher capacitance than the carbonized PAN at high current density. Instead, lower capacitance was obtained in the activated PAN, which suggests that other factor such as pseudocapacitance may be responsible for this phenomenon. To study the pseudocapacitance, the carbonized PAN and the activated PAN fiber mats were tested by cyclic voltammetry, and their specific capacitance is plotted as a function of voltage in Figure 3.14. A deformed rectangular shape is obtained for both samples, indicating the presence of a certain pseudocapacitance.[1, 7] Current density data obtained at different scan rates at a given voltage (0.1 V) for the carbonized PAN and activated PAN fiber mats is also plotted as a function of scan rate in Figure 3.15. It shows that the plot of the activated PAN deviates from linearity more significantly than that of the carbonized PAN, indicating surface functional groups or distributive capacitance behavior.[1, 7]

The presence of functional groups can also be confirmed by the elemental analysis of the fiber mats. Table 3.6 shows that carbon, nitrogen, and oxygen are present in both carbonized PAN and activated PAN fiber mats. The oxygen content in the activated PAN fiber mat is slightly higher than that in the carbonized PAN fiber mat. The oxygen containing groups can enhance the capacitance by improving the wettability of the electrodes or by introducing redox reactions.[13, 14]

In order to test the stability of the functional groups in the fiber mats, the cycle life of the carbonized and the activated PAN fiber mats was tested and the results are

given in Figure 3.16. For comparison, the cycle life of SWNT bucky paper is also included. For an electrochemical capacitor without any redox reactions, the capacitance should be stable for large number of charge/discharge cycles.[15] However, the capacitance of the carbonized or the activated PAN fiber mat decreases rapidly with cycle times compared to SWNT bucky paper, suggesting irreversible redox reactions. The capacitance of the activated PAN fiber mat decreases even more dramatically than that of the carbonized PAN fiber mat.

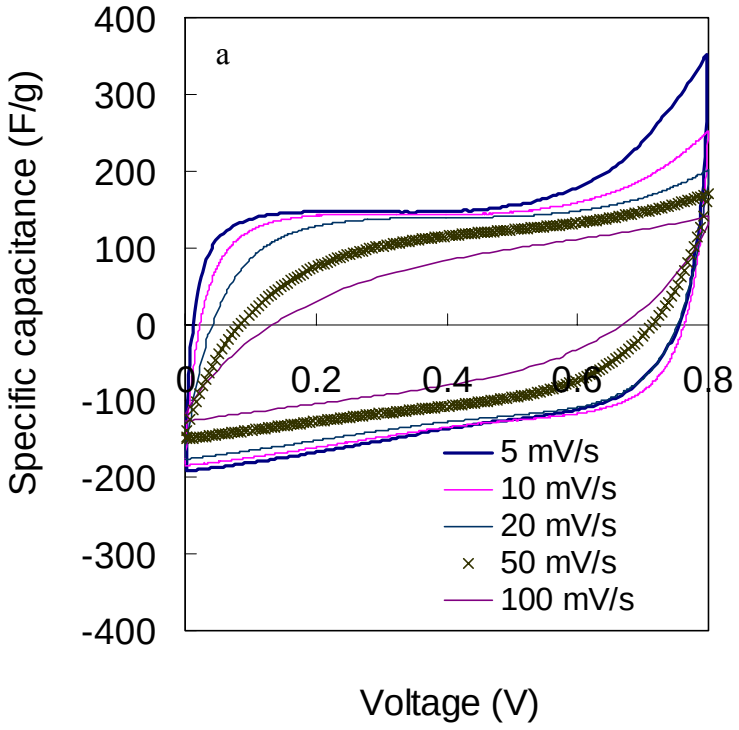

Figure 3.14. Specific capacitance as a function of voltage in cyclic voltammetry for (a) carbonized PAN and (b) activated PAN fiber mat.

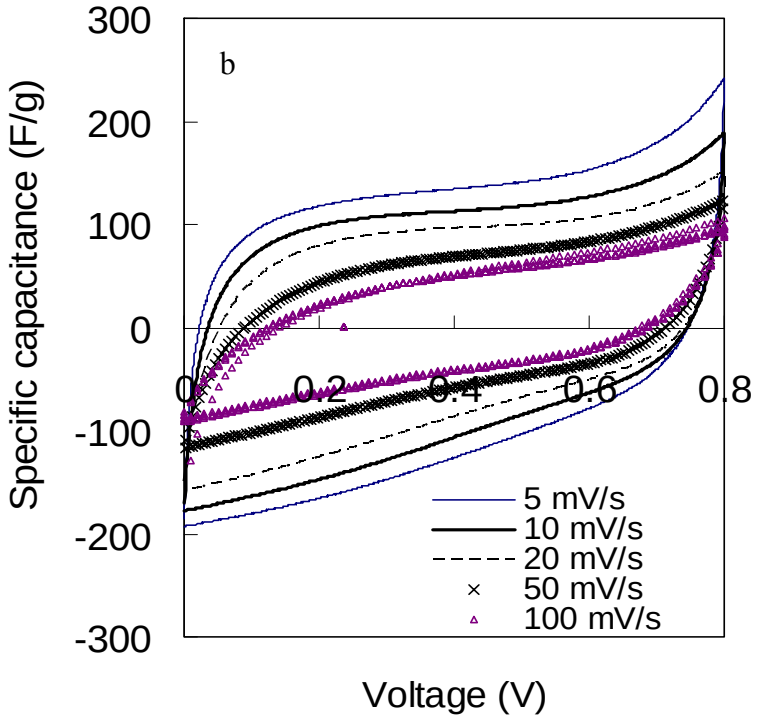

Figure 3.14. Continued.

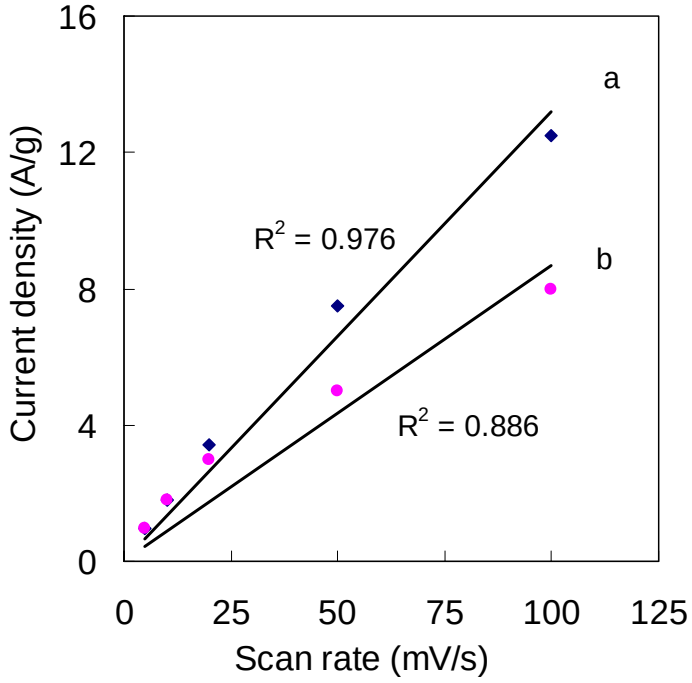

Figure 3.15. Current density as a function of scan rate for (a) carbonized PAN and (b) activated PAN (R^2 is the correlation coefficient, low R^2 value indicates significant deviation from linearity).

Table 3.6. Elemental analysis of carbonized PAN and activated PAN fiber mats.

Sample	**Carbon atomic percentage (%)**	**Nitrogen atomic percentage (%)**	*Oxygen atomic percentage (%)*
Carbonized PAN (1 st measurement)	82.4	10.2	7.4
Carbonized PAN (2 nd measurement)	84.5	8.3	7.2
Average	83.5	9.3	7.3
Activated PAN (1 st measurement)	81.8	9.5	8.7
Activated PAN (2 nd measurement)	81.2	9.7	9.1
Average	81.5	9.6	8.9

Constant current charge/discharge testing was typically carried out from low to high current density (Figure 3.13). In this process, when data was obtained at high current density, sample has already experienced 50 or more charge/discharge cycles. In this process, some of the functional groups may be already consumed due to irreversible redox reactions at low current density. Therefore, the contribution of pseudocapacitance to the total capacitance decreases, resulting in lower capacitance at high current density. Similarly, when the activated PAN fiber mat was charged/discharged from high to low current density, the reverse trend was observed.

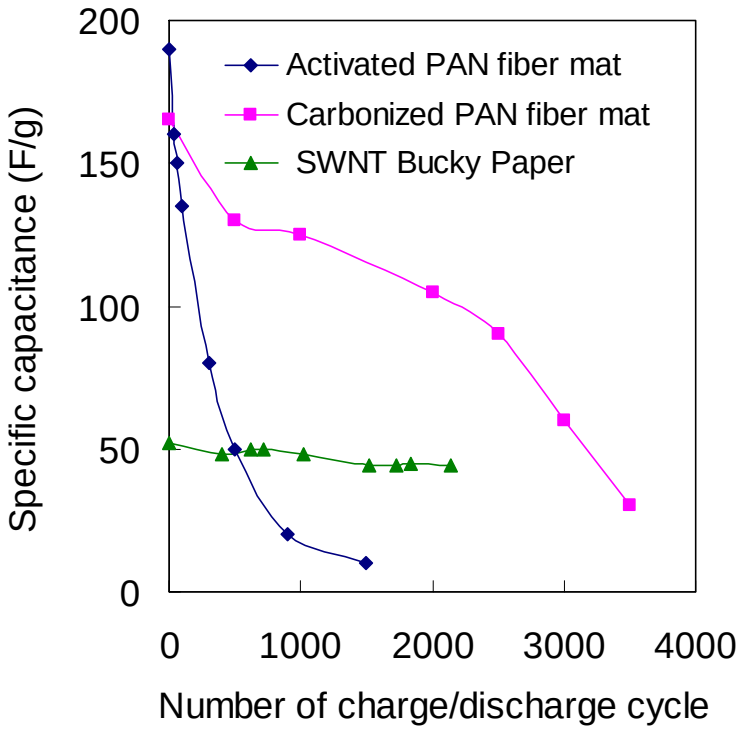

Figure 3.16. Specific capacitance as a function of charge/discharge cycle for carbonized PAN fiber mat (0.63 mg-0.47 mg), activated PAN fiber mat (0.37 mg-0.51 mg), and SWNT bucky paper (4.41-4.45 mg) at a charge/discharge current of 1 mA using 6M KOH electrolyte.

3.3.5 Carbonized PAN/SAN fiber mat based electrochemical capacitors

Micropores are dominant in both carbonized and activated PAN nanofibers (Table 3.5), which results in the capacitance at low current density; however, they cannot maintain high capacitance at high current density. On the other hand, mesopores can accommodate the electrolyte ions even when they have fast movement, which helps to maintain high capacitance at high current density. It was reported that mesoporous carbon exhibited high capacitance compared to microporous carbon at high current density.[16] The high capacitance was also maintained at high current density in poly(vinylidene chloride) based electrochemical capacitor with large pore volume.[12]

To provide better pore size control, PAN/SAN blends were electrospun into fiber mats and subsequently stabilized, carbonized. The pore formation process in the electrospun PAN/SAN nanofibers during carbonization is illustrated in Figure 3.17. TGA study indicates that PAN and SAN have different thermal stability, where SAN totally burns out while PAN leaves carbon residue when heated above 500 °C in nitrogen (Figure 3.18). Hence by burning out SAN domains in the electrospun PAN/SAN fibers, high porosity can be achieved.

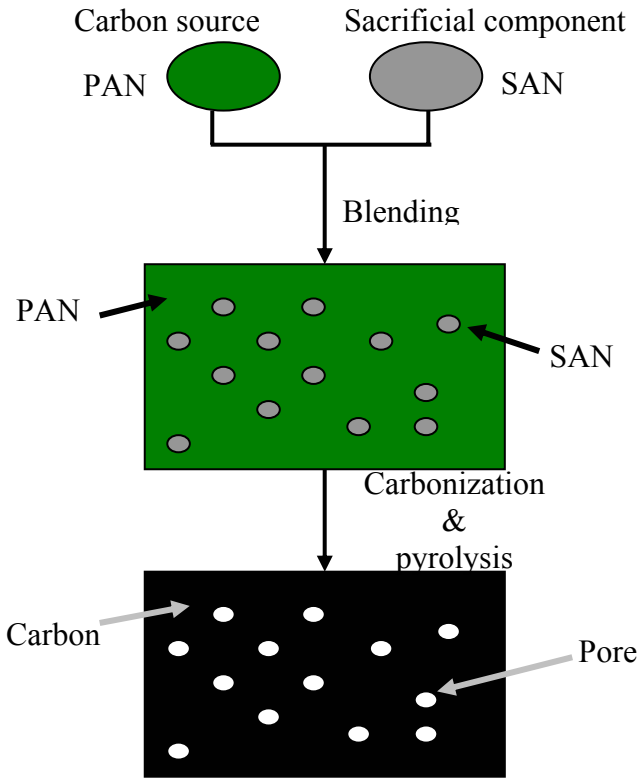

Figure 3.17. Schematic sketch of pore formation. (From ref. 17.)

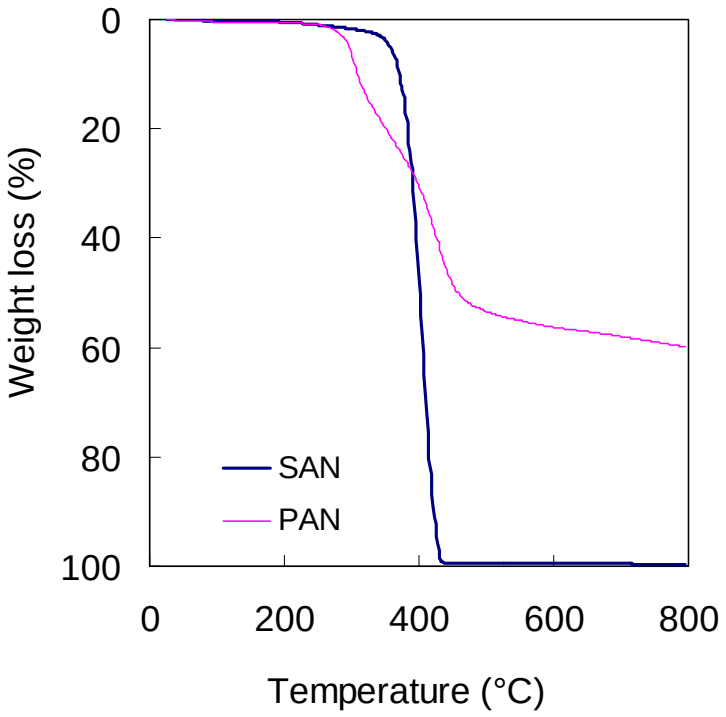

Figure 3.18. Thermogravimetric analysis plots of PAN and SAN at a heating rate of 5 °C/min in nitrogen.

3.3.5.1 Effect of PAN/SAN ratio on electrochemical capacitor performance

PAN and SAN form immiscible blend and their solutions in the PAN/SAN ratio of 90/10, 80/20, 70/30, and 50/50 appeared cloudy when dissolved at 18 wt% polymer (PAN + SAN in the desired PAN/SAN ratio) concentration in DMF. The SEM images of the carbonized PAN/SAN fiber mats are given in Figure 3.19. For comparison, the SEM image of the carbonized PAN/SAN (90/10) film[18] is also included. No visible pores are observed in the carbonized PAN/SAN (90/10) fibers. With further increasing SAN content, pores with dimensions of 20 to 50 nm are observed in the carbonized PAN/SAN fibers. On the other hand, rather large pores with dimension of several microns are observed in the carbonized PAN/SAN (90/10) film. The different pore size in the carbonized PAN/SAN fiber mats and PAN/SAN (90/10) film is due to difference in SAN domain size, which may be caused by

different solvent evaporation rate in electrospinning and film casting process. In electrospinning, solvent evaporates more rapidly due to the jet thinning and increasing of jet surface area, which causes formation of small SAN domain. On the other hand, in film casting, slower solvent evaporation allows enough time for SAN to form large domain.

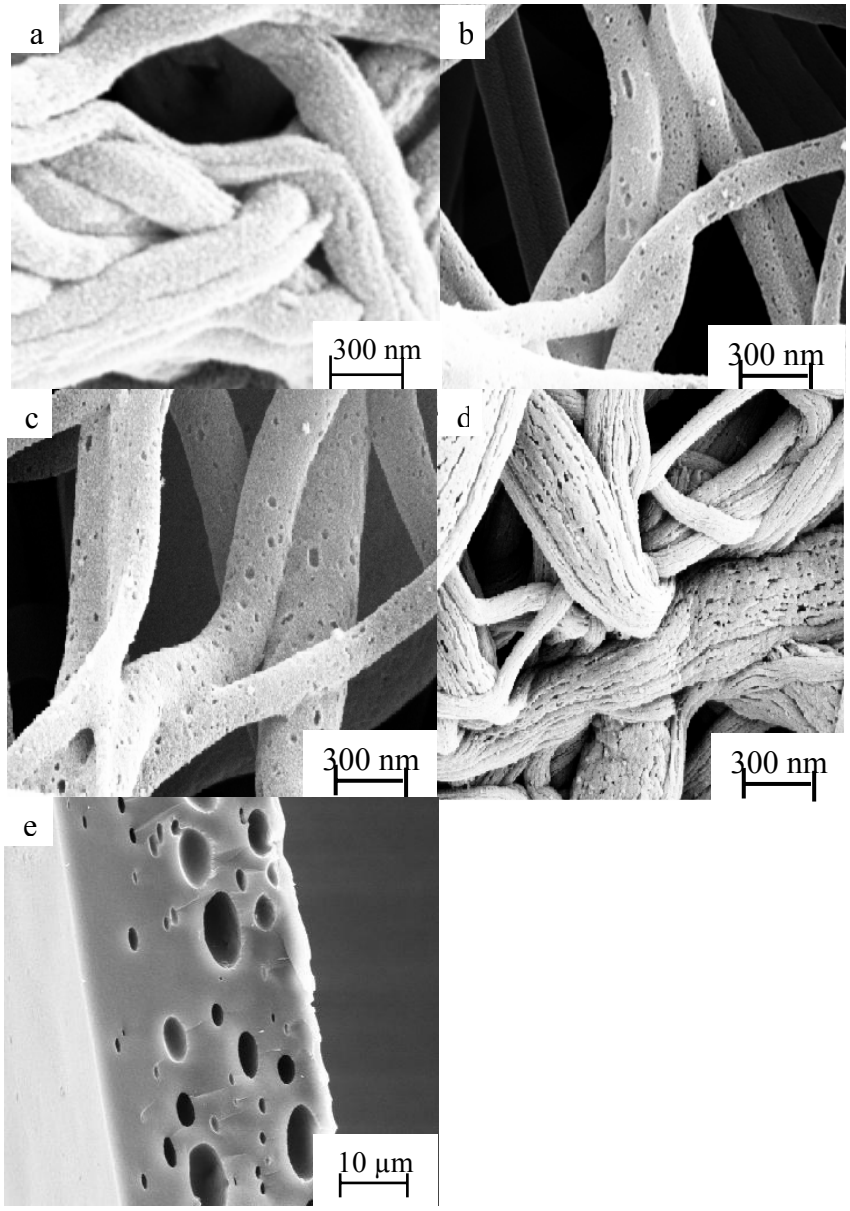

Figure 3.19. Scanning electron micrographs of carbonized PAN/SAN fiber mats in the PAN/SAN ratios of (a) 90/10, (b) 80/20, (c) 70/30, (d) 50/50 fiber mats, and (e) 90/10 film. ((e) From ref.18.)

The specific capacitance, surface area, and pore volume of the carbonized PAN and PAN/SAN fiber mats are given in Table 3.7. For comparison, the results of activated carbon reported in the literature are also included.[19, 20] The BET surface area values of the carbonized PAN and PAN/SAN fiber mats are below 400 m^2/g, which are much lower than that of the activated carbon (1000~3000 m^2/g).[21] The high capacitance and relatively low BET surface area of the carbonized PAN and PAN/SAN fiber mats result in high double-layer capacity values (double layer capacity = specific capacitance/surface area).

The pore size distribution of the carbonized PAN/SAN fiber mats is given in Figure 3.20. Compared to the carbonized PAN fiber mat, mesopore and macropore volumes of carbonized PAN/SAN fiber mats are much higher. The pore volume of the carbonized PAN/SAN fiber mats is plotted as a function of SAN content in Figure 3.21. The results indicate that SAN forms domains of size corresponding to the mesopores, which upon carbonization change the pore size distribution from micro- to mesopore domination. The carbonized PAN (Table 3.5) and PAN/SAN (90/10) fiber mats (Table 3.7) have similar pore volume, surface area, and capacitance, while with different pore size distributions. In the carbonized PAN fiber mat, micropores are dominant, while in the carbonized PAN/SAN (90/10) fiber mat, mesopores are dominant. The micropore or mesopore domination in these two fiber mats result in their different electrochemical behaviors, which will be discussed in section 3.3.5.2.

Table 3.7. Specific capacitance, surface area, pore volume, and double layer capacity of carbonized PAN/SAN fiber mats, and activated carbon reported in the literature.

Sample		**PAN/SAN (90/10)**	**PAN/SAN (80/20)**	**PAN/SAN (70/30)**	**PAN/SAN (50/50)**	**Activated carbon[19]**	**Activated carbon[20]**
S_{BET} (m^2/g)		252	306	374	367	2130	3150
S_{DFT} (m^2/g)		14	41	48	59	/	/
DFT pore volume (cm^3/g)	V_{micro}	0.005	0.025	0.024	0.029	/	/
	V_{meso}	0.027	0.068	0.059	0.067	/	/
	V_{macro}	0.005	0.033	0.014	0.026	/	/
	V_{total}	0.037	0.126	0.097	0.122	/	/
Specific capacitance (F/g, 1 mA charge/discharge, at 0.1 V)		170	210	190	175	100	312
BET double layer capacity ($\mu F/cm^2$)		68	69	51	48	4.7	9.9

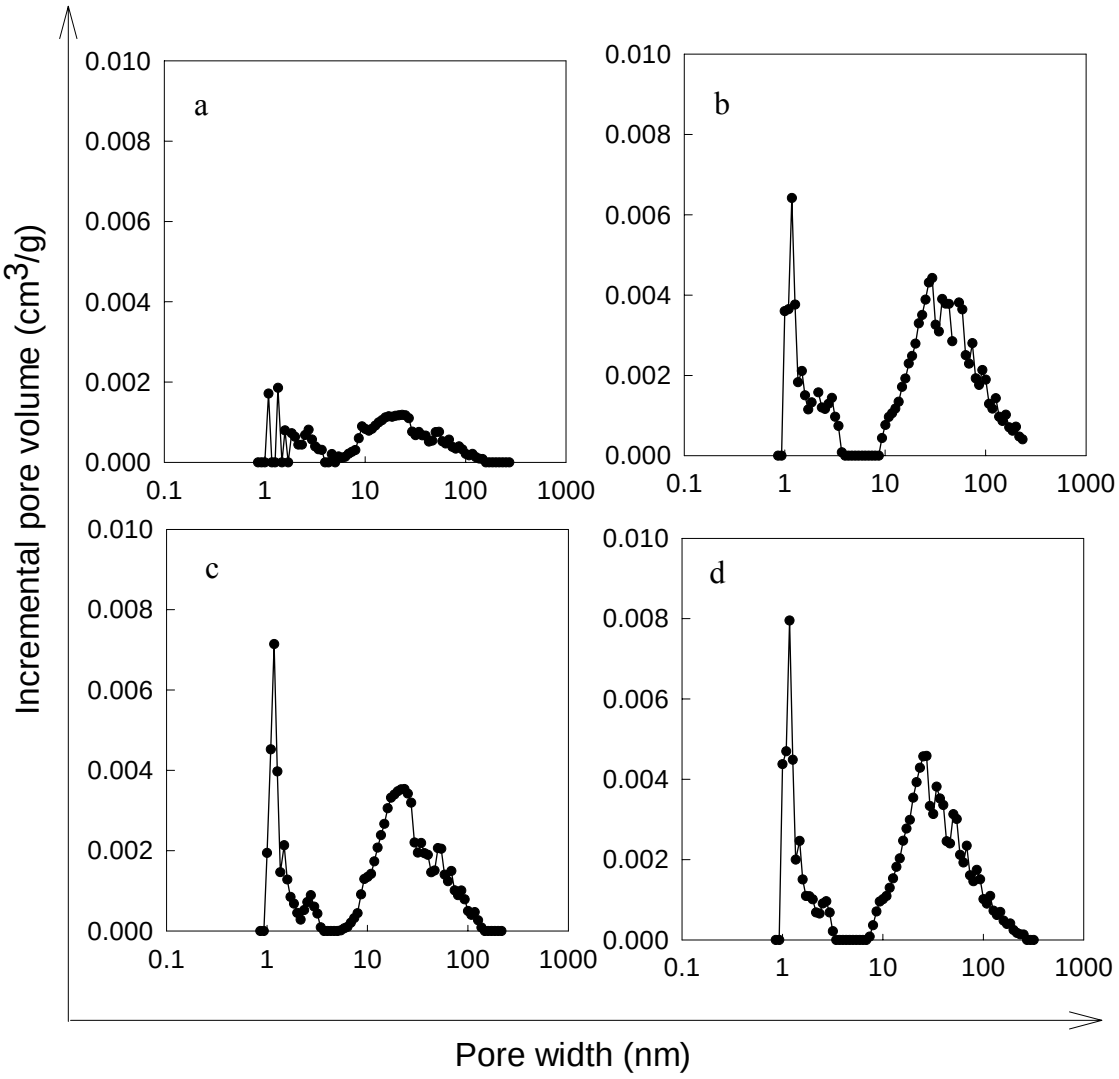

Figure 3.20. Pore size distribution of the carbonized PAN/SAN fiber mats in the PAN/SAN ratio of (a) 90/10, (b) 80/20, (c) 70/30, and (d) 50/50.

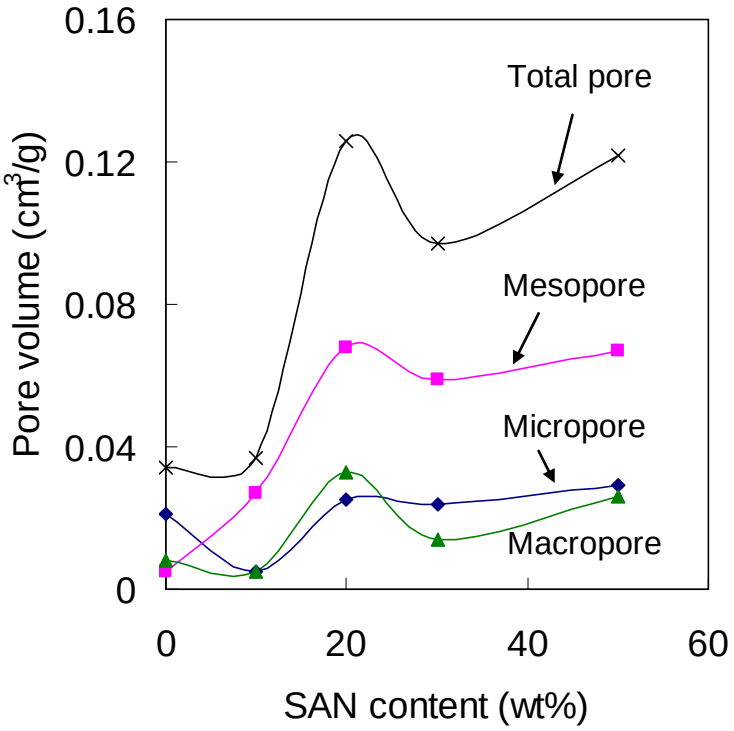

Figure 3.21. Pore volume as a function of SAN weight content.

3.3.5.2 Capacitance of carbonized PAN/SAN fiber mats as a function of current density

Figure 3.22 shows the specific capacitance of the carbonized PAN and PAN/SAN fiber mats as a function of current density. The results of steam activated electrospun PAN nanofibers reported in the literature are also included in this figure.[22] The carbonized PAN and PAN/SAN fiber mats processed in this study exhibit a capacitance of about 200 F/g at a current density of 1 to 2 A/g, while at this current density the capacitance value of steam activated PAN based nanofibers reported in the literature is below 100 F/g. The specific capacitance of PAN/SAN (80/20 and 50/50 ratio) fiber mats decreases rather rapidly with increasing current density, even though mesopore volume in these fiber mats is quite high. This behavior was confirmed on two different fiber mats carbonized in different batches. Figure 3.23 shows data for both batches, showing good reproducibility.

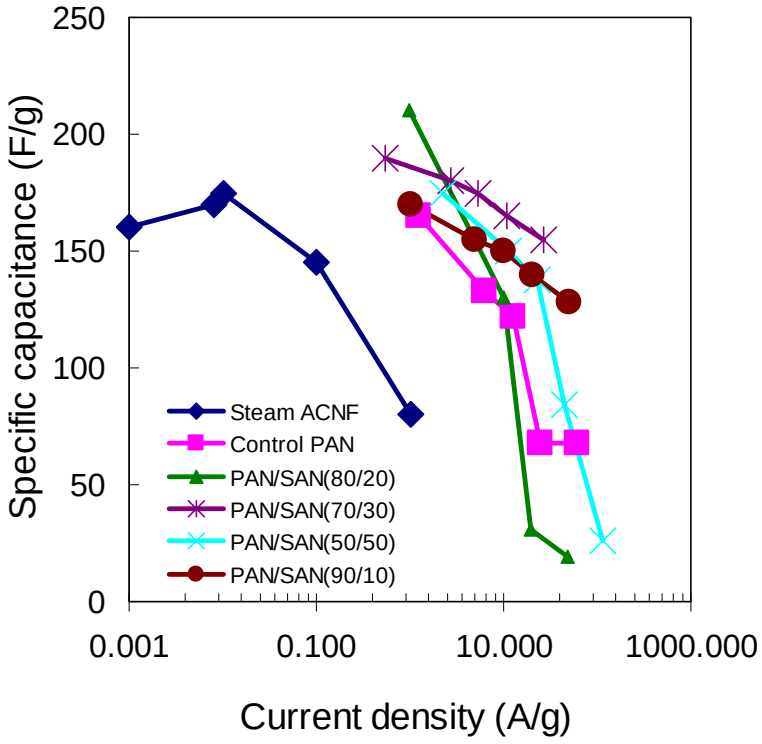

Figure 3.22. The specific capacitance as a function of current density for steam activated PAN (From ref. 22.), carbonized PAN(1.34 mg-2.01 mg), carbonized PAN/SAN(90/10) (3.72 mg-1.36 mg), carbonized PAN/SAN (80/20) (1.07 mg-1.0 mg), carbonized PAN/SAN (70/30)(3.44 mg-4.05 mg), and carbonized PAN/SAN (50/50) (0.77mg-1.04 mg) fiber mats from current studies.

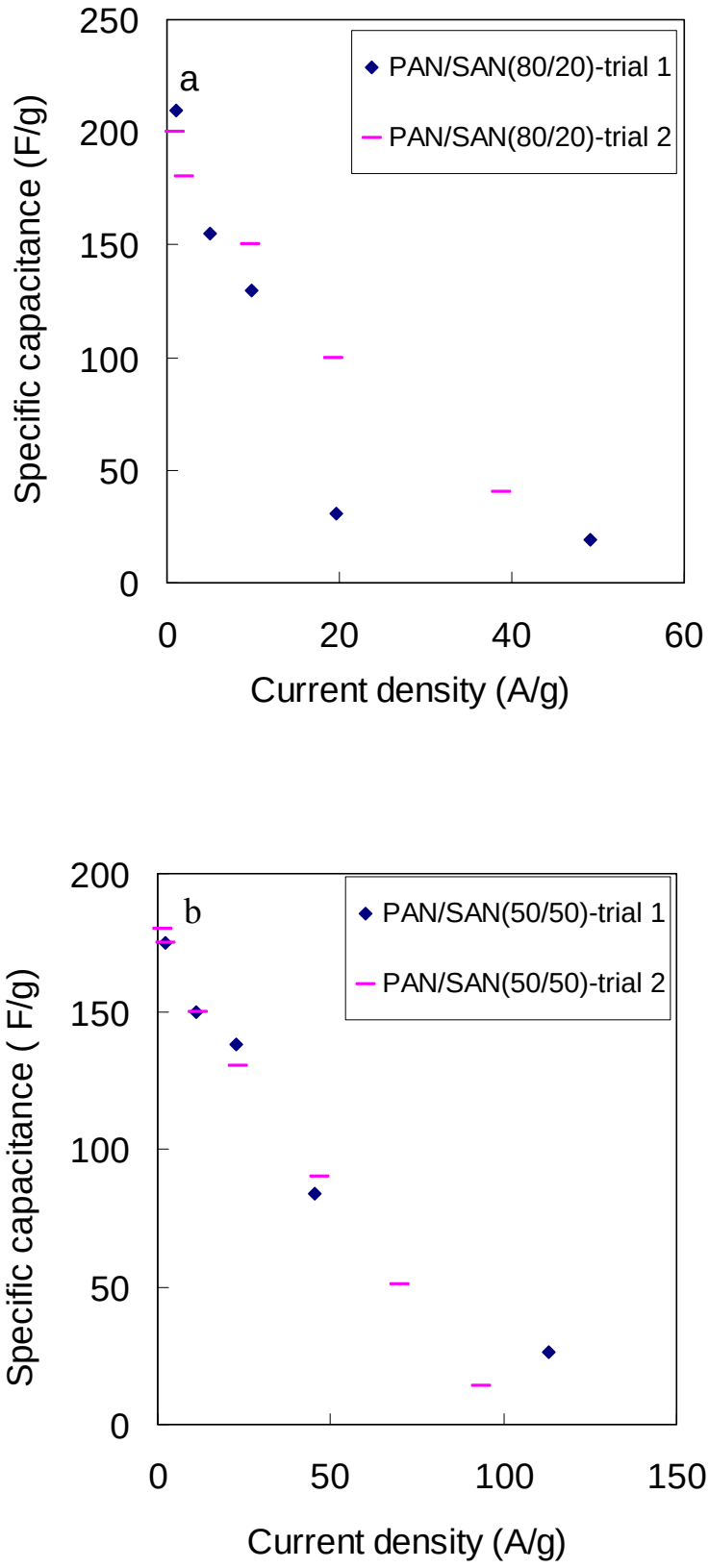

Figure 3.23. Specific capacitance as a function of current density for carbonized PAN/SAN fiber mats in the ratio of (a) 80/20 (trial 1(1.07 mg-1.00 mg) and trial 2 (6.35 mg-1.21 mg)) and (b) 50/50 (trial 1(0.77 mg-1.04 mg) and trial 2(0.81 mg-0.91 mg)).

3.3.6 Comparison between fiber mat and film based capacitors

The capacitance performance of carbonized PAN/SAN films (80/20[18] and 70/30) and PAN/SAN/SWNT (63/30/7) films[18] was compared with fiber mats. Figure 3.24 shows the SEM images of the carbonized PAN/SAN and PAN/SAN/SWNT films. Carbonized PAN/SAN fiber mat contains pore size of typically below 50 nm (Figure 3.19), while the carbonized PAN/SAN films exhibit much larger pores with typical dimensions ranging from 2 to 10 μm. The specific capacitance, surface area, and pore volumes of the carbonized fiber mats and films are given in Table 3.8. Compared to the carbonized PAN/SAN (80/20 and 70/30) fiber mats, the carbonized PAN/SAN (80/20 and 70/30) films have larger pores, smaller surface area, and lower capacitance.

The pore size distribution of the carbonized PAN/SAN/SWNT (63/30/7) film is shown in Figure 3.25. Even though the electrospun PAN/SAN (70/30) fiber mat and PAN/SAN/SWNT (63/30/7) film have the same SAN content (30%), they have different pore size distribution after carbonization. The carbonized PAN/SAN (70/30) fiber mat has high micropore volume (0.024 cm^3/g), while the carbonized PAN/SAN/SWNT film exhibits relatively high mesopore volume (0.157 cm^3/g). The high micropore volume in the carbonized PAN/SAN (70/30) fiber mat is responsible for the high capacitance at 1 mA charge/discharge. Meanwhile, compared to the PAN/SAN/SWNT film, the relatively loose structure of the electrospun PAN/SAN fiber mat can absorb more electrolytes in the open space between the nanofibers, which further improves the capacitance. Therefore, the specific capacitance of the carbonized PAN/SAN (70/30) fiber mat is higher than that of the carbonized PAN/SAN/SWNT (63/7/30) film by 84 F/g

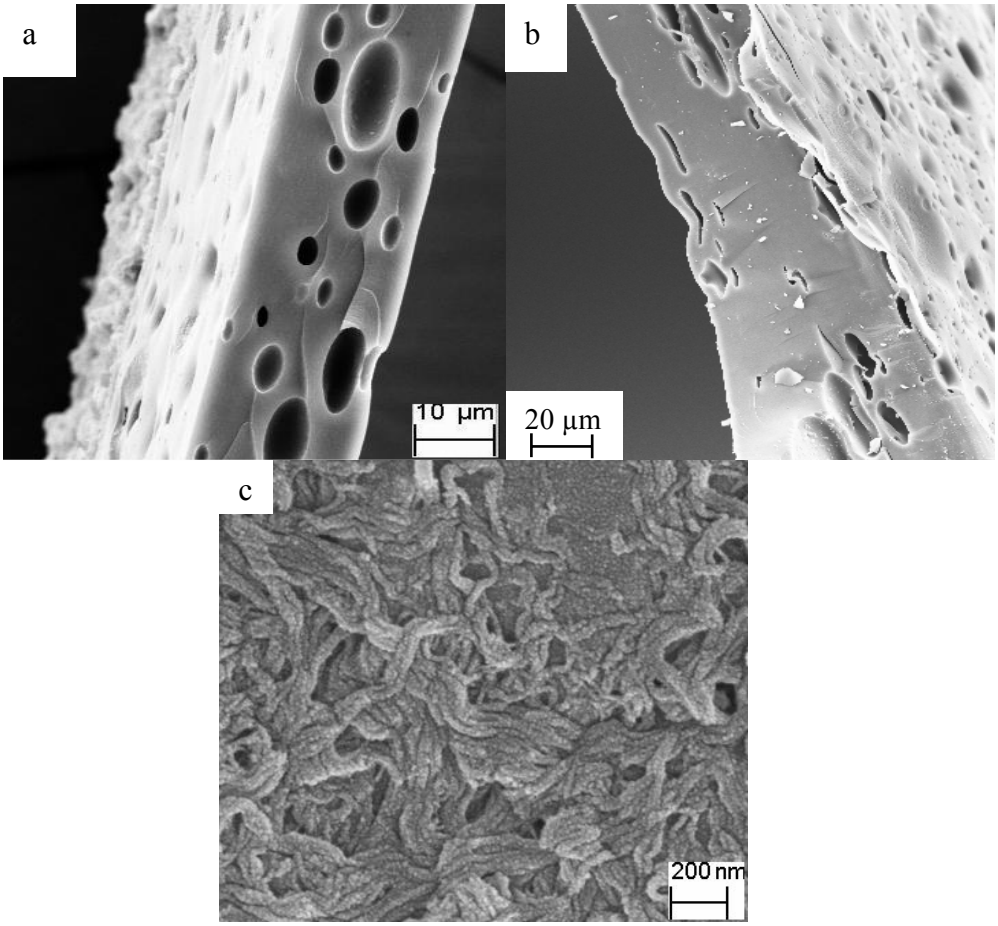

Figure 3.24. Scanning electron micrographs of carbonized PAN/SAN films in the PAN/SAN ratio of (a) 80/20, (from ref.18.) (b) 70/30, and (c) PAN/SAN/SWNT (63/30/7) film. (From ref.18)

Table 3.8. Specific capacitance, surface area, pore volume and double layer capacity of the carbonized fiber mats and films.

Sample		**PAN/SAN (80/20) film****	**PAN/SAN (80/20) fiber mat**	**PAN/SAN (70/30) film**	**PAN/SAN (70/30) fiber mat**	**PAN/SAN/SWNT (63/30/7) film****
Pore size*		2-10 μm	20-50 nm	2-10 μm	20-50 nm	/
S_{BET} (m^2/g)		/	306	/	374	87
S_{DFT} (m^2/g)		/	41	/	48	48
DFT pore volume (cm^3/g)	V_{micro}	/	0.025	/	0.024	0.011
	V_{meso}	/	0.068	/	0.059	0.157
	V_{macro}	/	0.033	/	0.014	0.070
	V_{total}	/	0.126	/	0.097	0.238
Specific capacitance (F/g, 1 mA charge/discharge, at 0.1 V)		10	210	10	190	106
BET double layer capacity ($\mu F/cm^2$)		/	69	/	51	122

* Pore size was determined by SEM images.
** From ref.18.

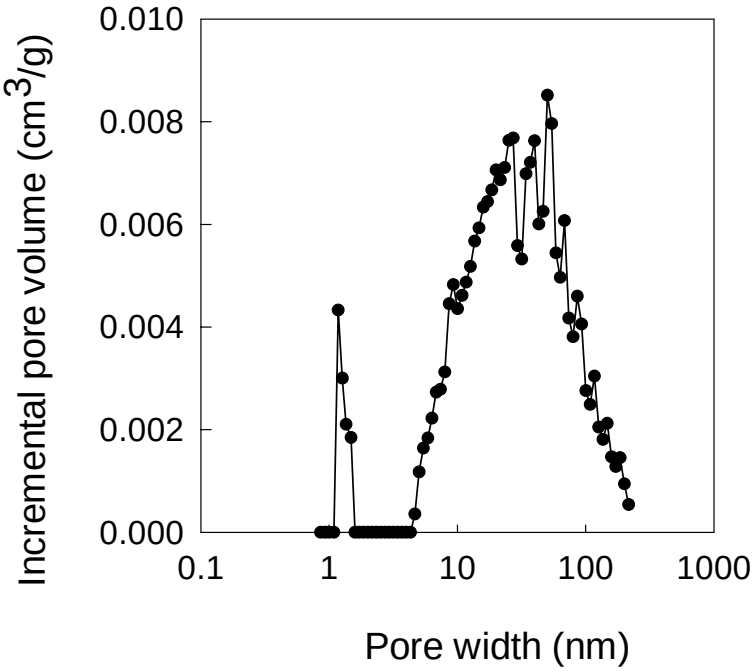

Figure 3.25. Pore size distribution of carbonized PAN/SAN/SWNT (63/30/7) film. (From ref.18.).

3.3.7 Carbonized PAN/carbon nanotube fiber mat based electrochemical capacitors

3.3.7.1 Carbonized PAN/SAN/SWNT fiber mat based electrochemical capacitors

1 or 3 wt% SWNT was added into PAN/SAN (80/20) electrospinning solution. The dispersions were electrospun into the fiber mats, subsequently stabilized and carbonized to develop electrochemical capacitor electrodes. Figure 3.26 and Figure 3.27 show the SEM images of the electrospun PAN/SAN/SWNT fiber mats before and after carbonization, respectively. Compared to the electrospun PAN/SAN (80/20) nanofibers, the surface of the electrospun PAN/SAN/SWNT fibers is rough. After carbonization, SWNT bundles with diameter of 50 to 60 nm are observed to protrude out of the fibers.

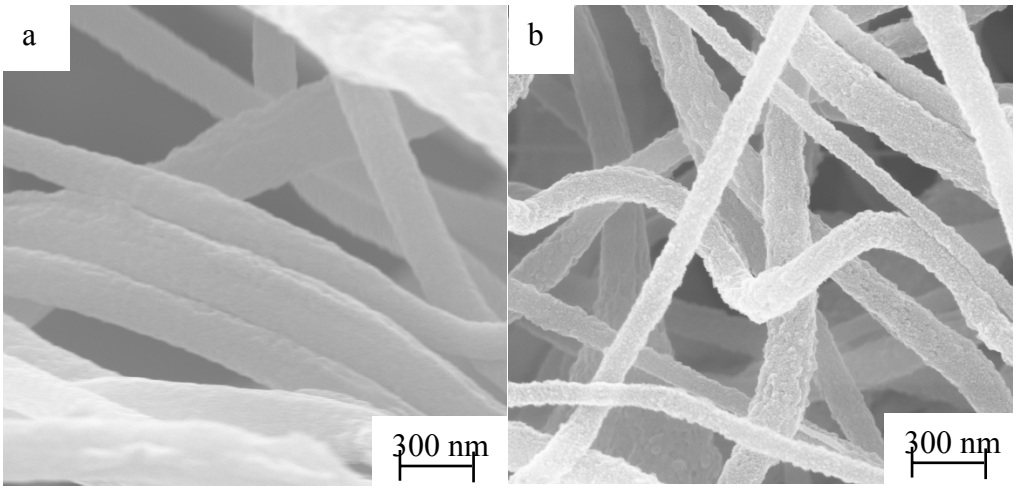

Figure 3.26. Scanning electron micrographs of (a) PAN/SAN/SWNT (80/20/1 wt%) and (b) PAN/SAN/SWNT (80/20/3 wt%) fiber mats.

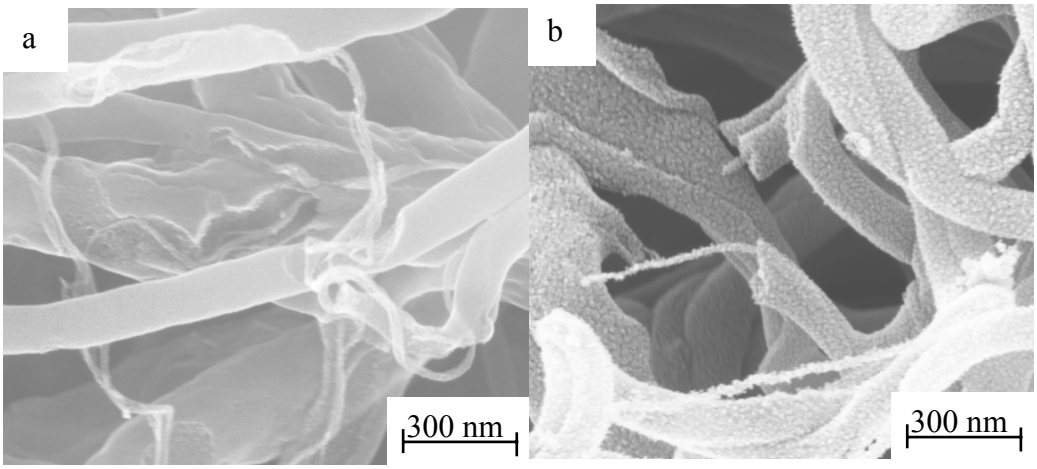

Figure 3.27. Scanning electron micrographs of carbonized (a) PAN/SAN/SWNT (80/20/1 wt%) and (b) PAN/SAN/SWNT (80/20/3 wt%) fiber mats.

The specific capacitance of the carbonized PAN/SAN and PAN/SAN/SWNT fiber mats is plotted as a function of current density in Figure 3.28. It shows that both carbonized PAN/SAN and PAN/SAN/SWNT fiber mats have comparable capacitance at low current density, but with increasing current density, the capacitance of the carbonized PAN/SAN/SWNT is higher than that of the carbonized PAN/SAN fiber mat. Figure 3.29 shows the Ragone plots of the carbonized PAN/SAN (80/20) and PAN/SAN/SWNT (80/20/1 wt % and 80/20/3 wt%) fiber mats at 1 mA charge/discharge. With the addition of 1 wt% SWNT into PAN/SAN, the power density is enhanced by a factor of four from 180 to 850 W/kg, and the energy density is improved from 5000 to 8500 J/kg. With further increasing in SWNT concentration, the power density increases only slightly from 850 to 950 W/kg, and the energy density is enhanced from 8500 to 8700 J/kg. Figure 3.30 shows the Ragone plots of the carbonized PAN/SAN/SWNT (80/20/3 wt%) fiber mat charged/discharged at different currents. It shows that at 20 mA charge/discharge current, the power density is 7000 W/kg.

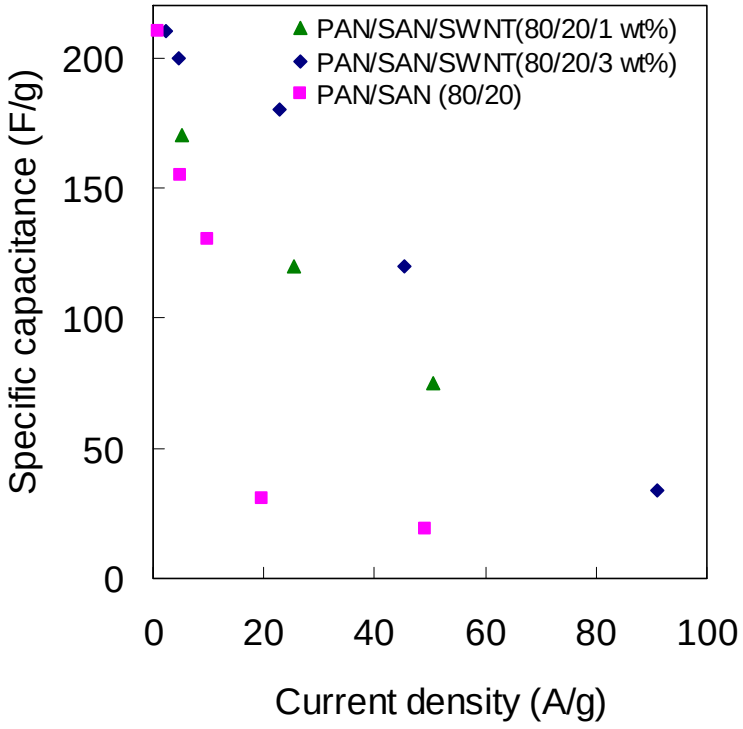

Figure 3.28. Specific capacitance as a function of current density for carbonized PAN/SAN(80/20) (1.07 mg-1.00 mg), carbonized PAN/SAN/SWNT (80/20/1wt%) (0.40 mg-0.39 mg), and carbonized PAN/SAN/SWNT (80/20/3 wt%) (0.44 mg-0.44 mg) fiber mats.

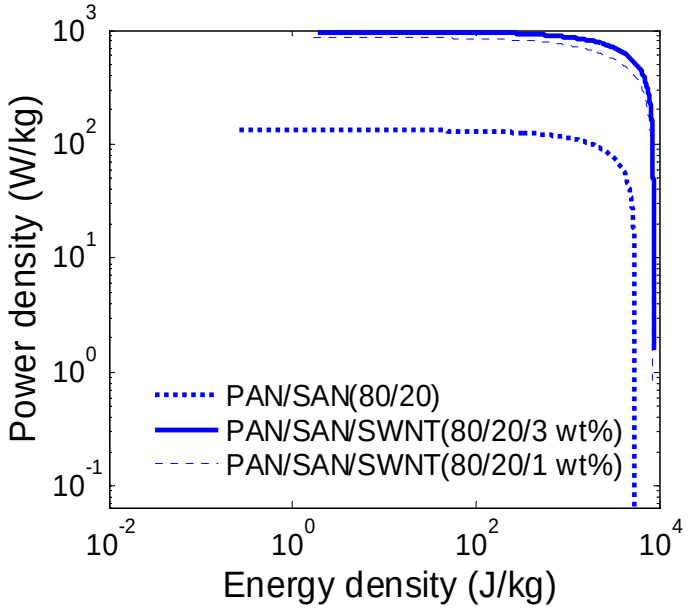

Figure 3.29. Ragone plots of carbonized fiber mats at 1 mA charge/discharge.

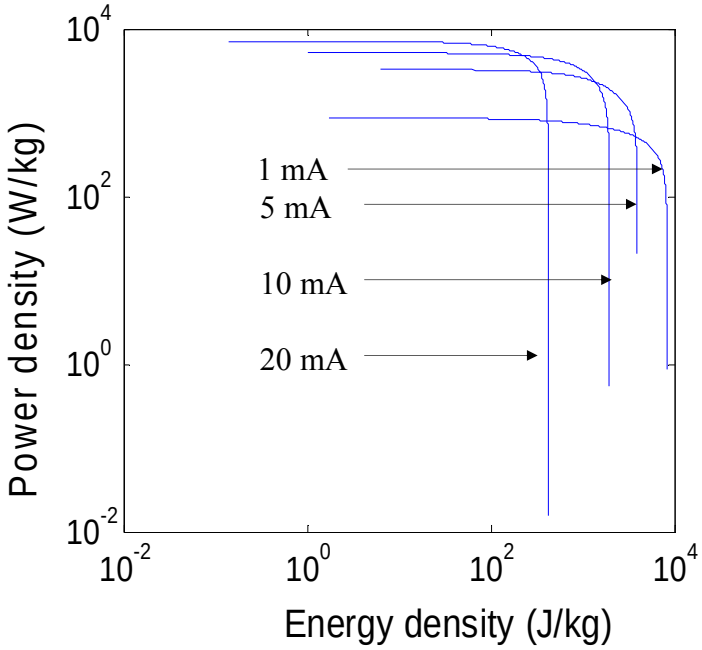

Figure 3.30. Ragone plots of carbonized PAN/SAN/SWNT (80/20/3 wt%) fiber mat charged/discharged at different currents.

The direct current (dc) electrical conductivity of the carbonized PAN/SAN and PAN/SAN/SWNT fiber mats was determined by four probe conductivity method, and the results are given in Table 3.9. With the addition of 1 and 3 wt% SWNT into PAN/SAN, the electrical conductivity is improved by almost a factor of two and three, respectively.

Table 3.9. In plane DC conductivity of the carbonized PAN/SAN and PAN/SAN/SWNT fiber mats.

Sample	**Conductivity (S/m)**
Carbonized PAN/SAN(80/20) fiber mat	4.3
Carbonized PAN/SAN/SWNT(80/20/1 wt%) fiber mat	9.7
Carbonized PAN/SAN/SWNT(80/20/3 wt%) fiber mat	12.2

The impedance of the carbonized PAN/SAN and PAN/SAN/SWNT fiber mats in 6 M KOH was measured and the results are shown in Figure 3.31. At high low frequency region, the straight line indicates the diffusion accessibility of electrolyte ions, which is affected by the electrode thickness[23]; at low frequency region, a semicircle is intercepts with the impedance real axis at R_Ω and (R_Ω + R_F). R_Ω represents the ohmic solution resistance and should be constant for a given electrolyte. R_F represents the sum of the bulk of the electrodes and the contact resistance between the electrode and the current collector.[22, 24] For all three samples, R_Ω is about 1 Ω, which is consistent with the reported resistance value of KOH.[25] In all three samples, the contact resistance between the electrode and current collector should be identical. Therefore, the decrease in R_F suggests a decrease in the electrode resistance. With addition of SWNT, the R_F value of the electrodes decreases, resulting in higher power density. Since the carbonized PAN/SAN/SWNT (80/20/1 wt%) and (80/20/3 wt%) have similar resistance, their power density values are quite comparable.

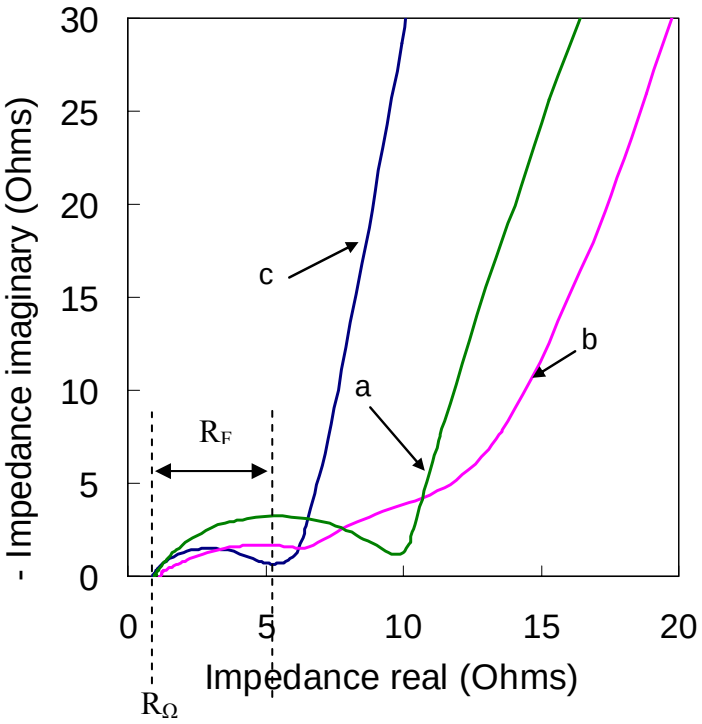

Figure 3.31. Impedance plots of (a) carbonized PAN/SAN (80/20), (b) carbonized PAN/SAN/SWNT (80/20/1 wt%), and (c) carbonized PAN/SAN/SWNT (80/20/3 wt%) fiber mats.

3.3.7.2 Carbonized PAN/MWNT fiber mat based electrochemical capacitors

Figure 3.32 shows the SEM images of electrospun PAN/MWNT fiber mats before carbonization. At low MWNT concentration, fiber surface is smooth. With increasing MWNT concentration, the fiber surface becomes rough with aggregates and irregularities. For PAN/MWNT fiber mats in the ratio of 80/20 and 70/30, some MWNTs are observed to protrude out of the fiber surface. Figure 3.33 gives the SEM images of the carbonized PAN/MWNT fiber mats. With increasing MWNT concentration, more and more MWNTs are observed to protrude out of the nanofibers.

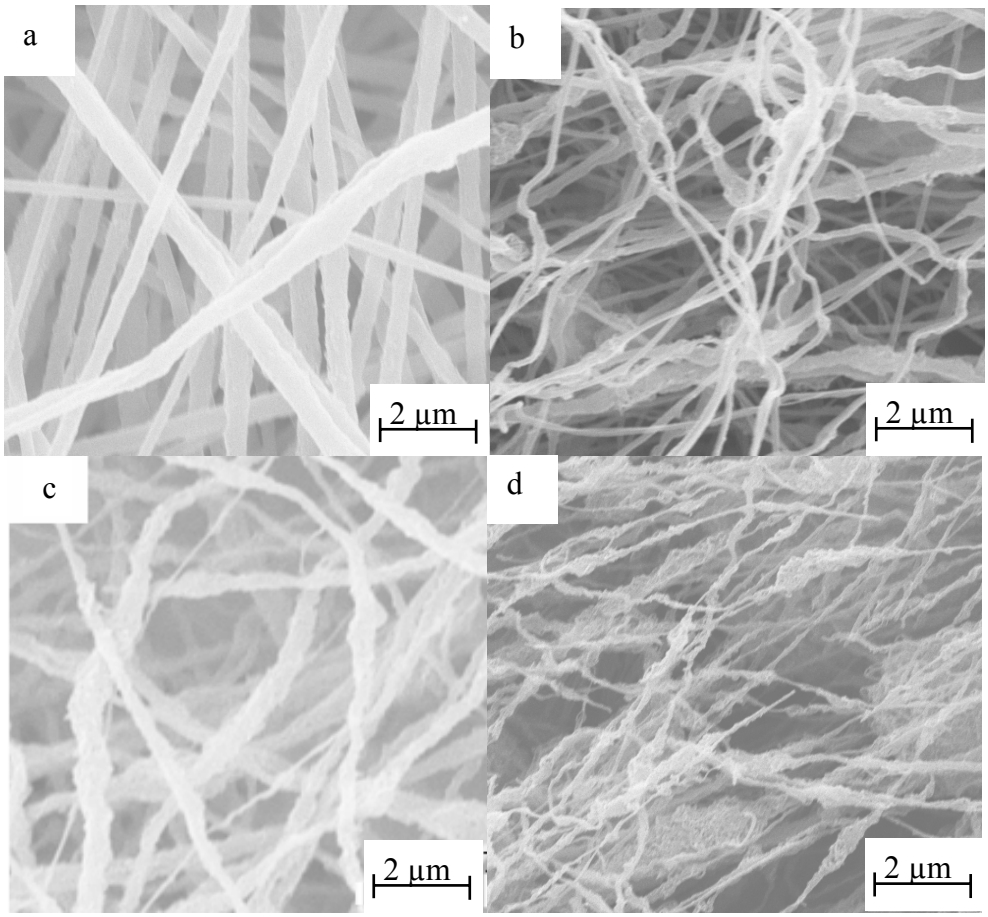

Figure 3.32. Scanning electron micrographs of electrospun PAN/MWNT fiber mats before carbonization in the PAN/MWNT ratios of (a) 95/5, (b) 90/10, (c) 80/20, and (d) 70/30.

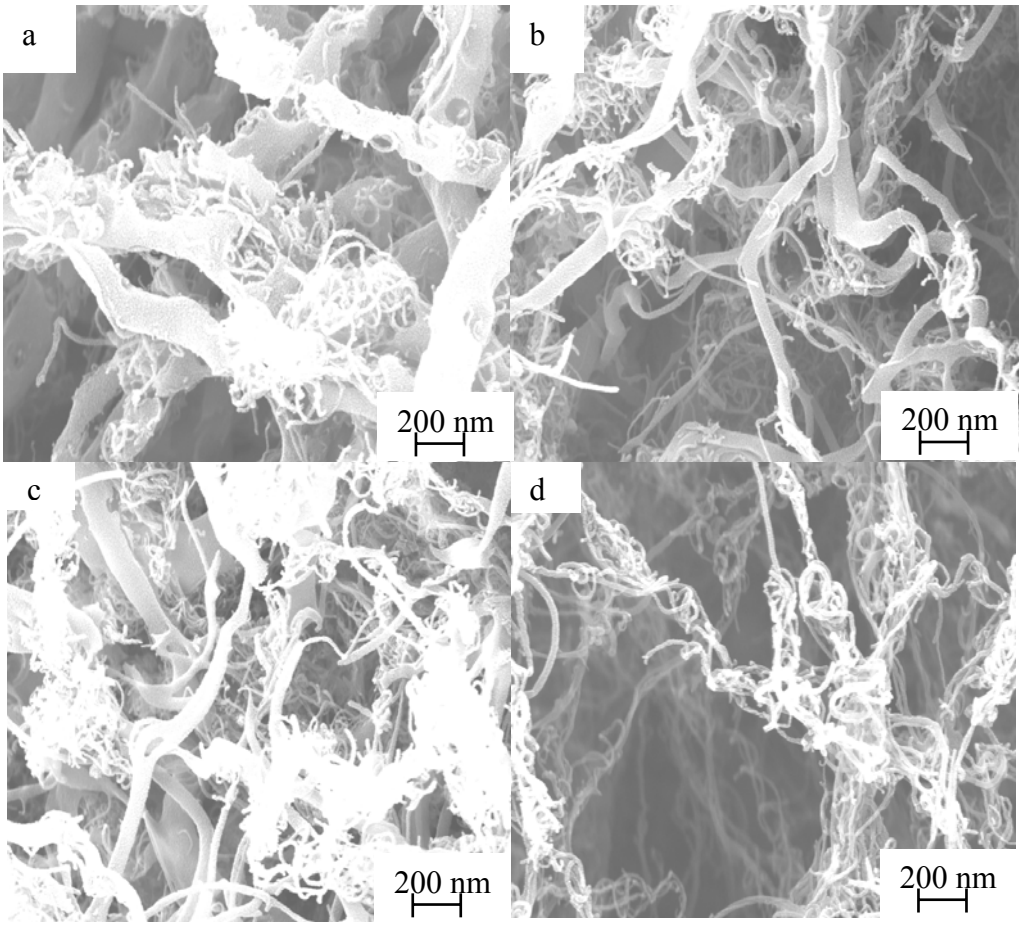

Figure 3.33. Scanning electron micrographs of carbonized PAN/MWNT fiber mats in the PAN/MWNT ratio of (a) 95/5, (b) 90/10, (c) 80/20, and (d) 70/30.

The pore size distribution of the carbonized PAN/MWNT fiber mats and MWNT powder are given in Figure 3.34. Their specific capacitance, surface area and pore volume are given in Table 3.10. Compared to the carbonized PAN fiber mat, micro-, meso-, macropore and total pore volume of carbonized PAN/MWNT fiber mats are significantly higher. The micro- and mesopore volume percentages are plotted as a function of MWNT content in Figure 3.35. With the addition of MWNT, the micropore percentage decreases while mesopore percentage increases, which indicates that the role of MWNT is to change the pore size distribution from micro to mesopore domination.

Table 3.10. Specific capacitance, surface area, pore volume and double layer capacity of the carbonized PAN/MWNT fiber mats and MWNT powder.

Sample		**PAN/MWNT (95/5)**	**PAN/MWNT (90/10)**	**PAN/MWNT (80/20)**	**PAN/MWNT (70/30)**	**MWNT powder**
S_{BET} (m^2/g)		447	343	340	274	162
S_{DFT} (m^2/g)		93	132	66	90	78
DFT pore volume (cm^3/g)	V_{micro}	0.053	0.069	0.033	0.023	0.015
	V_{meso}	0.055	0.105	0.076	0.234	0.283
	V_{macro}	0.064	0.158	0.073	0.096	0.355
	V_{total}	0.172	0.332	0.182	0.353	0.653
Specific capacitance (F/g, 1 mA charge/discharge, at 0.1 V)		140	108	73	18	/
BET double layer capacity ($\mu F/cm^2$)		31.3	31.5	21.5	6.6	/

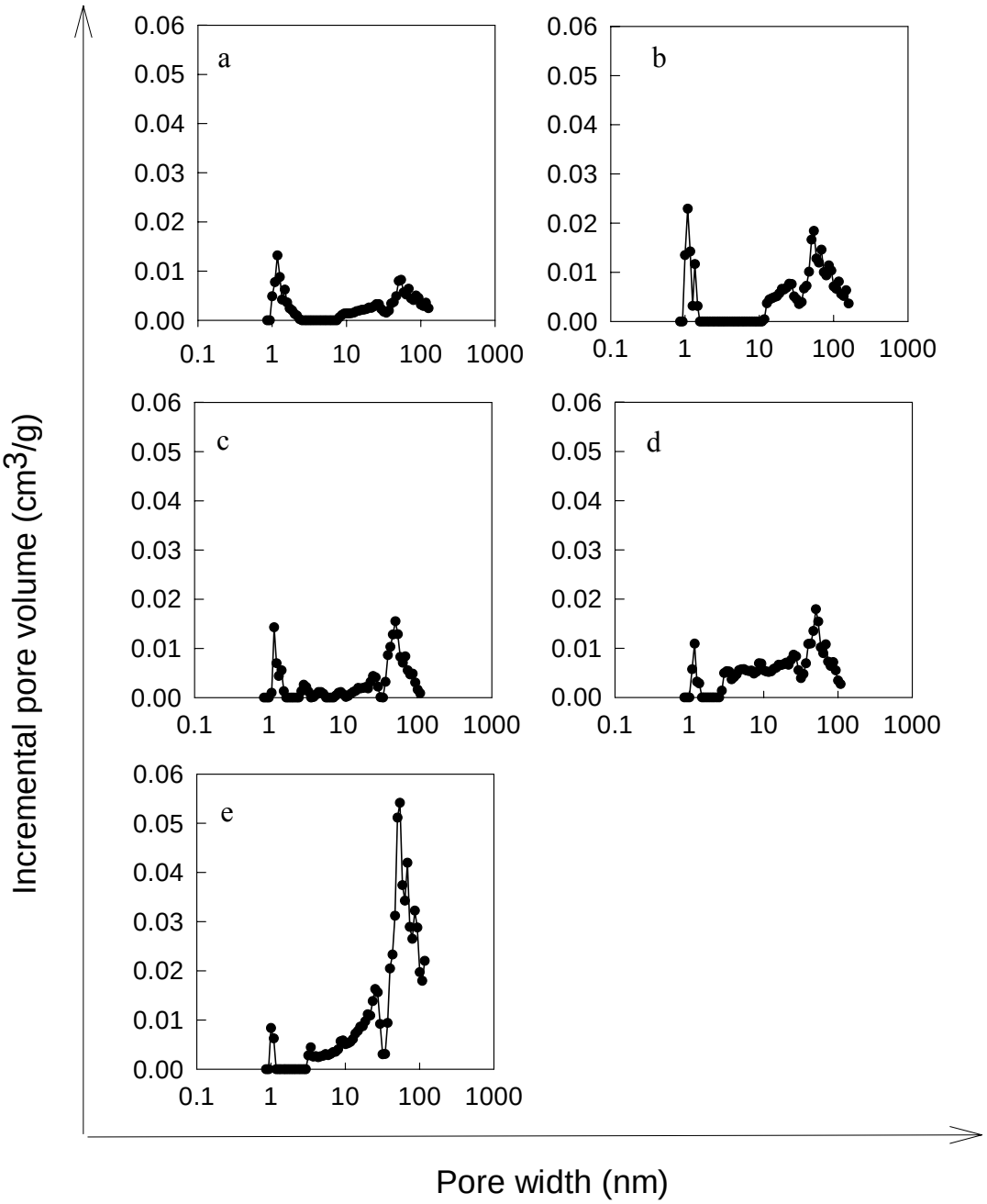

Figure 3.34. Pore size distribution of carbonized PAN/MWNT fiber mats in the ratio of (a) 95/5, (b) 90/10, (c) 80/20, (d) 70/30, and (e) MWNT powder.

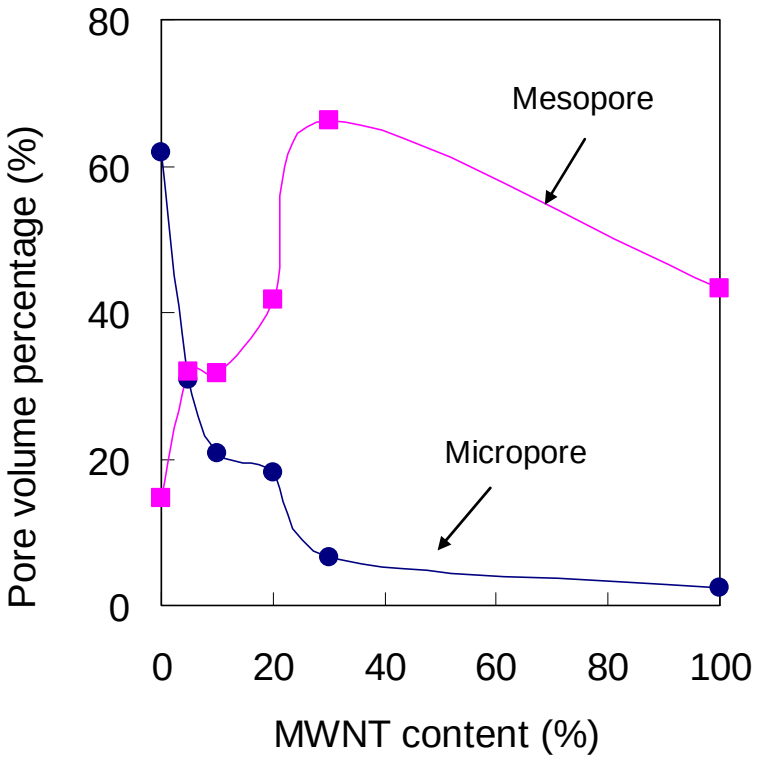

Figure 3.35. Pore volume percentage as a function of MWNT content.

Figure 3.36 shows the specific capacitance of carbonized PAN/MWNT fiber mats as a function of current density. The carbonized PAN/MWNT (95/5) fiber mat has highest capacitance, while other carbonized PAN/MWNT fiber mats with ratio of 90/10, 80/20, and 70/30 exhibit lower capacitance than the carbonized PAN/MWNT (95/5) or PAN fiber mats. With increasing MWNT concentration, the capacitance of the carbonized PAN/MWNT fiber mat rather decreases.

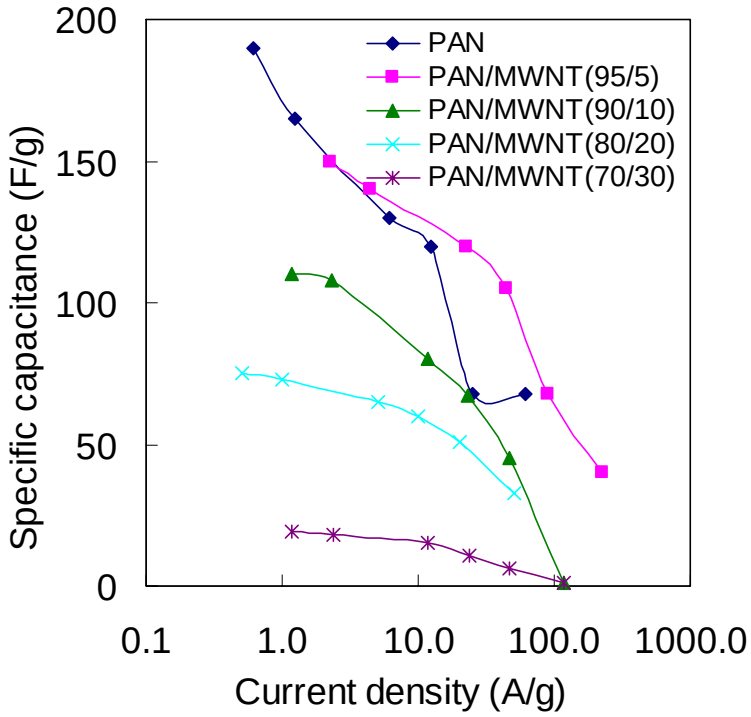

Figure 3.36. Specific capacitance as a function of current density for carbonized PAN (1.34 mg-2.01 mg), carbonized PAN/MWNT(95/5)(0.42 mg-0.46 mg), carbonized PAN/MWNT (90/10)(0.80 mg-0.92 mg), carbonized PAN/MWNT(80/20)(1.84 mg-2.17 mg), carbonized PAN/MWNT(70/30)(0.90 mg-0.80 mg) fiber mats.

The electrolyte wettability plays an important role in electrochemical capacitor performance. It was reported that the surface modification of the activated carbon aerogel by a surfactant enhanced the electrolyte wettability and improved the capacitance by a factor of two.[15] Oxidation of MWNT improved the electrode wettability by H_2SO_4 electrolyte, and thus, enhanced the capacitance by a factor of two.[26] Surface treated activated carbon was also developed for the electrochemical capacitor.[27] With surface modification, the electrolyte wettability was greatly improved, resulting in the lower internal resistance, and the capacitance was improved by 20 F/g.

In this work, the contact angles between the carbonized PAN/MWNT fiber mats and 6 M KOH were measured. Figure 3.37 shows the micrographs and Table 3.11 summarizes the contact angle results. For low MWNT concentration, carbonized

PAN/MWNT fiber mat can be completely wetted by KOH; while at high MWNT concentration, the fiber mats become hydrophobic. The poor wettability of PAN/MWNT fiber mats may be due to the protruding MWNTs out of fibers as they are hydrophobic. For carbonized PAN/MWNT (95/5) fiber mat, even though its micro- and mesopore volumes are not the highest, it can be completely wetted by the electrolyte, resulting in higher capacitance than other carbonized PAN/MWNT fiber mats.

Poor electrolyte wettability of the carbonized PAN/MWNT fiber mats at high MWNT concentration is also a possible reason for their low power density. The power density of carbonized PAN/MWNT fiber mats as a function of MWNT concentration is given in Figure 3.38, and the Ragone plots are shown in Figure 3.39. The carbonized PAN/MWNT fiber mats have higher power density than the carbonized PAN fiber mat, while the power density does not show a trend with increasing MWNT concentration. With increasing MWNT concentration, the electrolyte wettability of the carbonized PAN/MWNT fiber mats decreases (Table 3.11). It was reported that the electrolyte affinity of the activated carbon was improved by using a surfactant, which resulted in decreased resistance. [27, 28] With increasing MWNT concentration, the electrolyte wettability becomes worse, which decreases the conductivity of the electrodes; therefore, the power density does not show a trend with MWNT concentration.

Table 3.11. Contact angle between various carbonized fiber mats and 6 M KOH electrolyte.

Sample	**Contact angle (°)**
Carbonized PAN fiber mat	< 10
Carbonized PAN/MWNT (95/5) fiber mat	< 10
Carbonized PAN/MWNT (90/10) fiber mat	87 ± 4
Carbonized PAN/MWNT (80/20) fiber mat	132 ± 3
Carbonized PAN/MWNT (70/30) fiber mat	142 ± 4

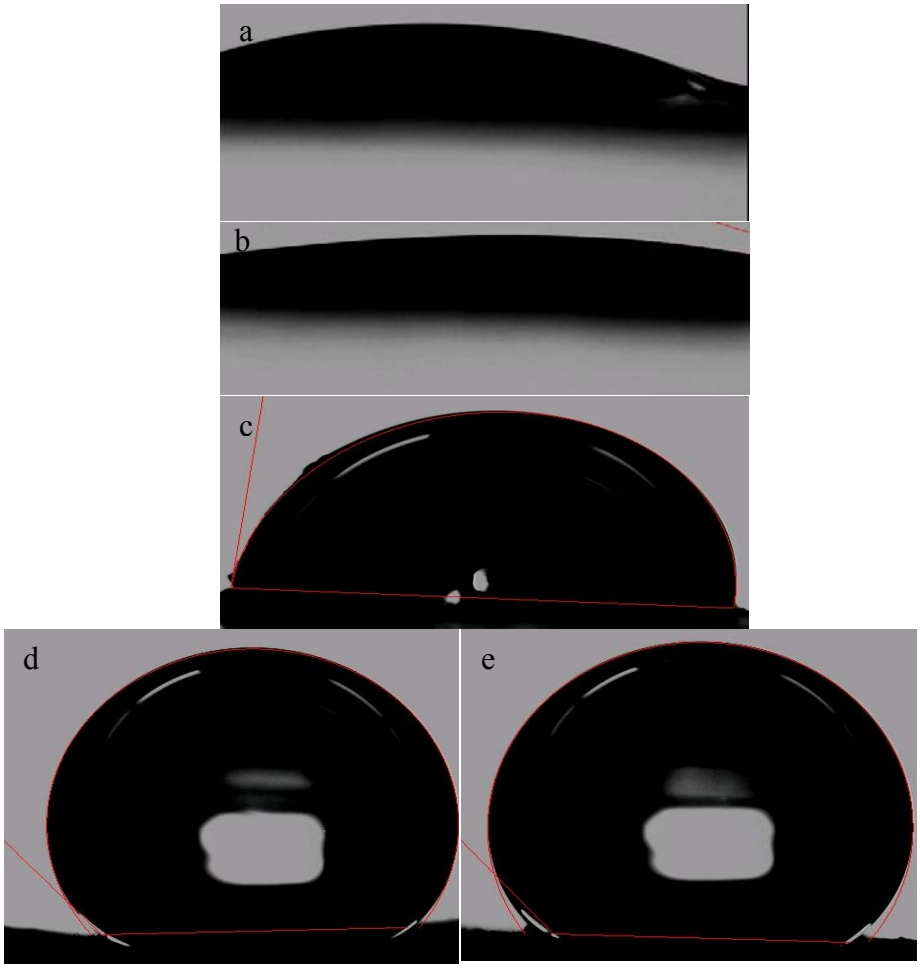

Figure 3.37. Micrographs of contact angle between 6 M KOH and (a) carbonized PAN fiber mat and carbonized PAN/MWNT fiber mats in the PAN/MWNT ratio of (b) 95/5, (c) 90/10, (d) 80/20, and (e) 70/30.

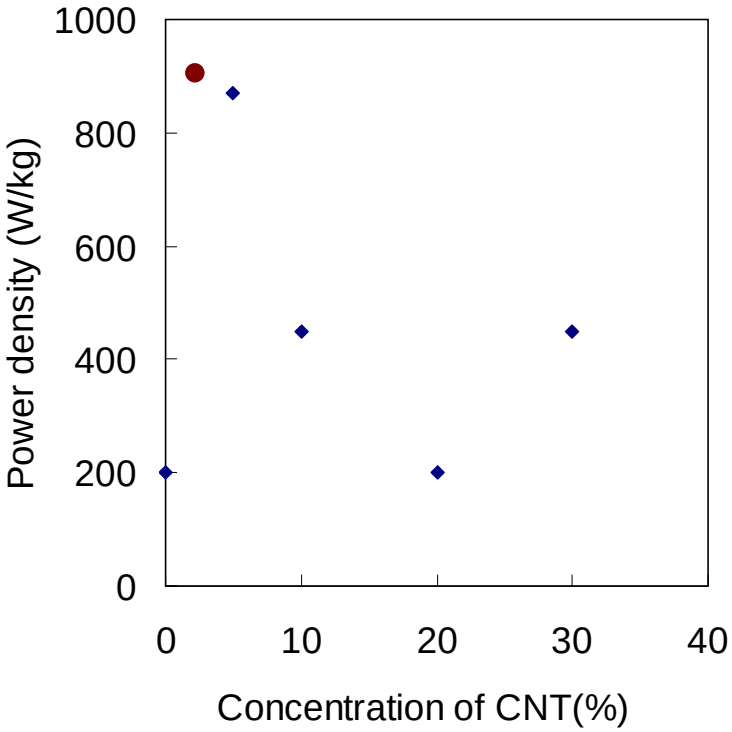

Figure 3.38. Power density as a function of CNT concentration for carbonized PAN/MWNT, carbonized PAN/SAN/SWNT(80/20/3 wt%) (data indicated by symbol ●) fiber mats at 1 mA charge/discharge current.

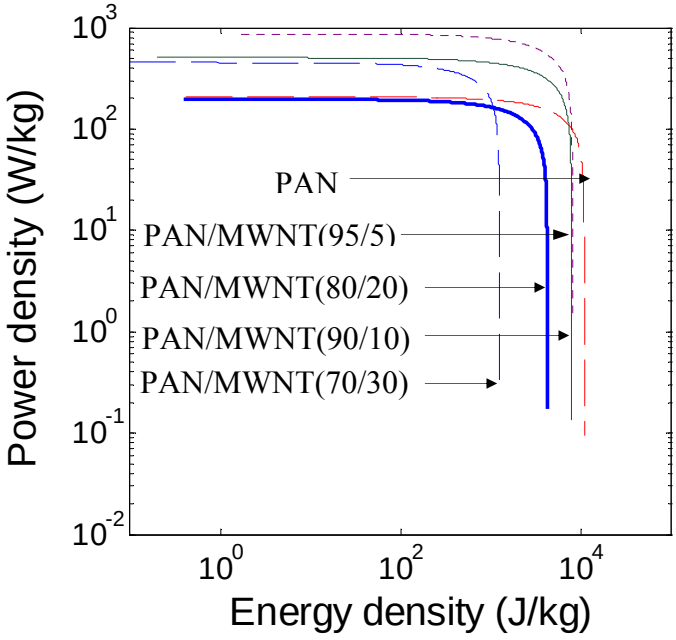

Figure 3.39. Ragone plots of carbonized PAN and PAN/MWNT fiber mats.

3.3.8 Comparison of carbonized fiber mat with other carbon materials.

The capacitance of carbonized PAN/SAN (70/30) fiber mat is compared with that of activated carbon pellet and carbon nanotube (SWNT and DWNT) bucky paper in Figure 3.40. The carbonized PAN/SAN (70/30) fiber mat exhibits a capacitance value of about 190 F/g, while SWNT, DWNT, and activated carbon have much lower capacitance values of 48, 35, and 30 F/g, respectively. The SWNT capacitance is consistent with the value reported by An et al.,[29] while the activated carbon has much lower capacitance than the reported values. It was reported that the capacitance value of the activated carbon with addition of graphite ranged from 270 to 380 F/g.[30] The capacitance value of the activated carbon electrodes using 5 wt% poly(vinylidene fluoride)(PVDF) as binder ranged from 80 to 125 F/g.[31] It was also reported that the capacitance value reached 123 F/g in the activated carbon electrodes using poly(vinylidene fluoride-hexafluoropropylene) (PVdF-HFP) gel electrolyte as binder, and the content of binder materials affected the capacitance.[32] In these literature reports, the surface area and pore size distribution of the activated carbon are different from the one used in the current work; secondly, the composition of the electrode materials such as addition of graphite[31] and content of binder material[32] also influences the capacitance. Therefore, different capacitance values were reported.

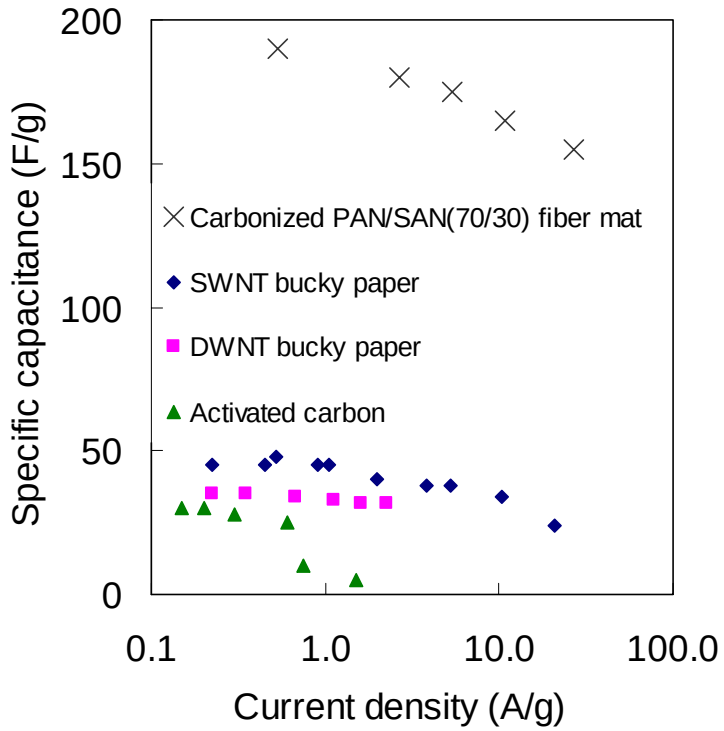

Figure 3.40. Specific capacitance as a function of current density for carbonized PAN/SAN(70/30) fiber mat(3.44 mg-4.05 mg), SWNT bucky paper(1.90 mg-1.93 mg), DWNT bucky paper(8.20 mg-9.61 mg), and activated carbon(13.2 mg-13.33 mg).

The pore size distribution of carbon nanotube bucky papers and activated carbon is given in Figure 3.41. Their specific capacitance, surface area and pore volume are given in Table 3.12. The activated carbon shows the largest surface area and highest micropore volume, while it exhibits the lowest capacitance value. On the other hand, the carbonized PAN/SAN (70/30) fiber mat has the lowest surface area and micropore volume, while it has the highest capacitance value. The high micropore volume in SWNT, DWNT bucky papers, and activated carbon doesn't result in high capacitance.

Table 3.12. Specific capacitance, surface area, pore volume and double layer capacity of various carbon samples.

Sample		**Carbonized PAN/SAN (70/30) fiber mat**	**SWNT bucky paper**	**DWNT bucky paper**	**Activated carbon**
S_{BET} (m^2/g)		374	546	496	1553
S_{DFT} (m^2/g)		48	297	246	609
DFT pore volume (cm^3/g)	V_{micro}	0.024	0.106	0.043	0.328
	V_{meso}	0.059	0.518	0.811	0.121
	V_{macro}	0.014	0.062	0.110	0.002
	V_{total}	0.097	0.686	0.964	0.451
Specific capacitance (F/g, 1 mA charge/discharge, at 0.1 V)		190	48	35	20
BET double layer capacity ($\mu F/cm^2$)		51	8.8	7.1	1.2

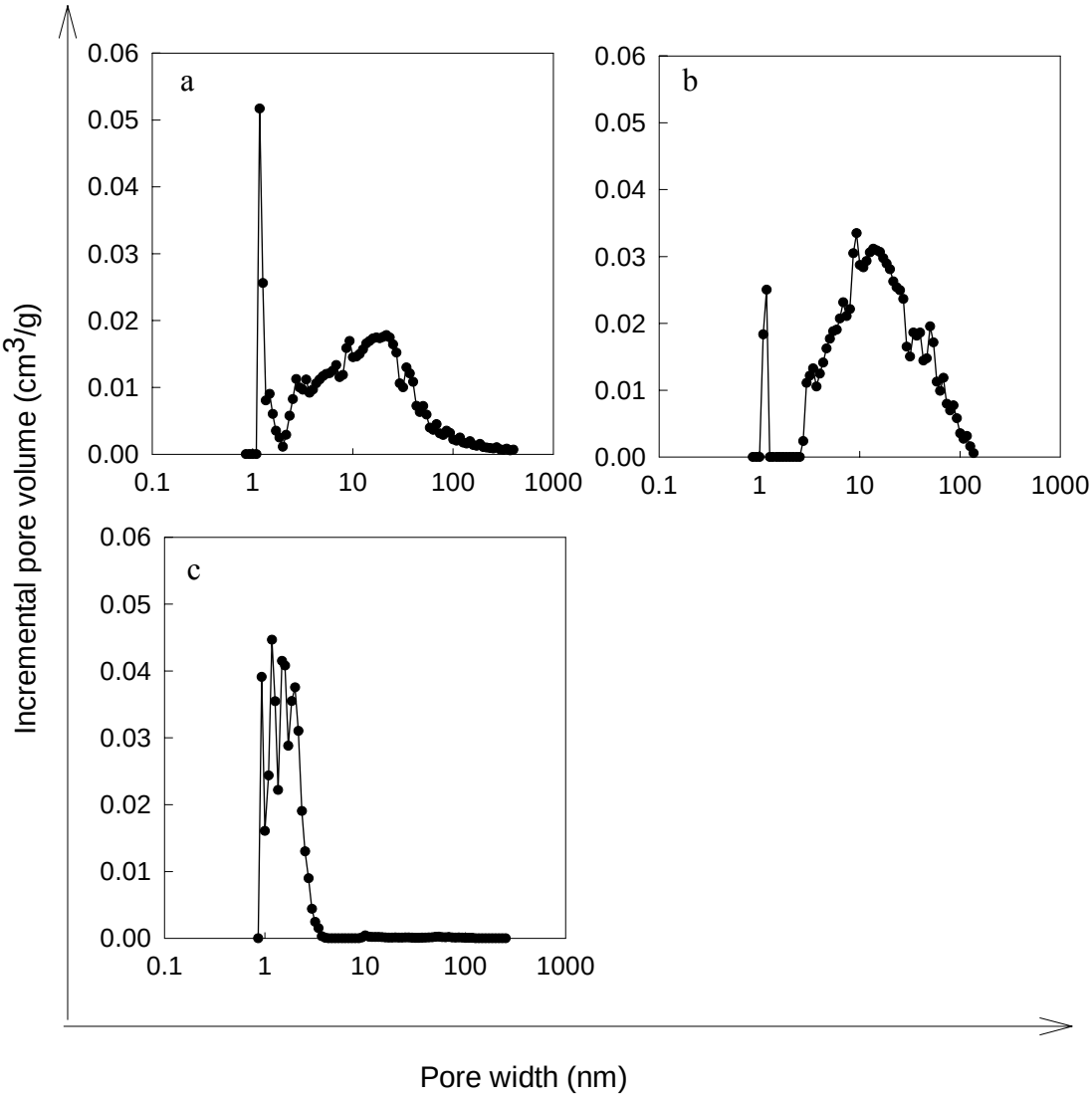

Figure 3.41. Pore size distribution of (a) SWNT, (b) DWNT, and (c) activated carbon pellet.

The 6 M KOH aqueous solution contact angle with the activated carbon, carbonized PAN/SAN fiber mat, and bucky papers were also measured. Figure 3.42 shows the micrographs and results are given in Table 3.13. The contact angle between KOH and SWNT bucky paper, DWNT bucky paper, or activated carbon is above 100°, indicating that these samples do not have good affinity with the electrolyte. On the other hand, the carbonized PAN/SAN (70/30) fiber mat is completely wetted by the electrolyte (contact angle < 10°). The good electrolyte wettability of the carbonized PAN/SAN fiber mat may be responsible for its high capacitance.

Table 3.13. Contact angle between various carbon materials and 6 M KOH.

Sample	**Contact angle (°)**
Carbonized PAN/SAN (70/30) fiber mat	< 10
SWNT bucky paper	101 ± 3
DWNT bucky paper	106 ± 7
Activated carbon	131 ± 2

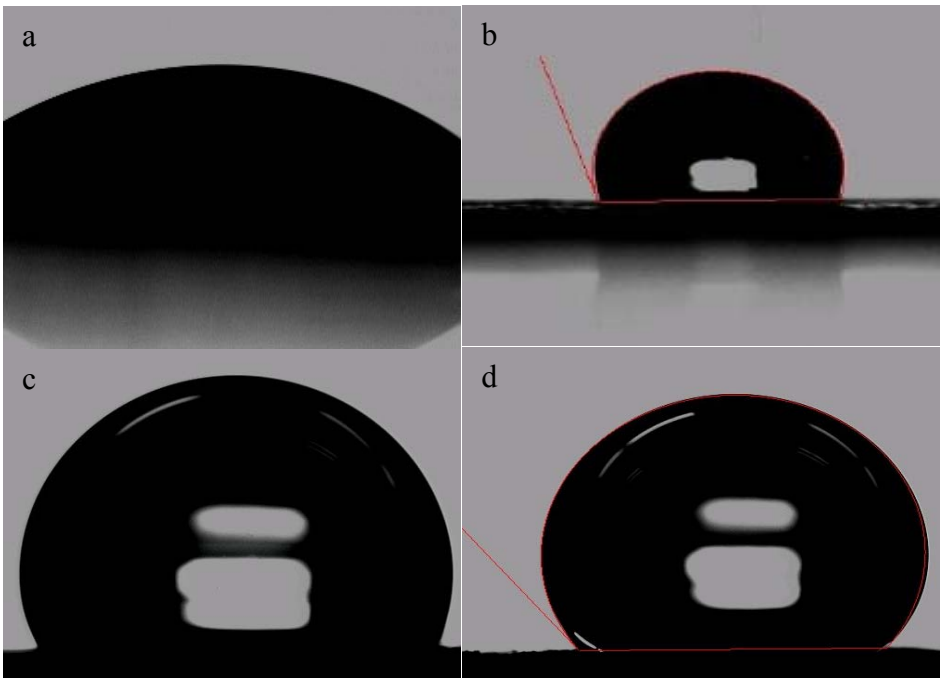

Figure 3.42. Micrographs of contact angle between 6 M KOH and (a) carbonized PAN/SAN (70/30) fiber mat, (b) SWNT bucky paper, (c) DWNT bucky paper, and (d) activated carbon.

3.4 Conclusions

The key conclusions of this study are:

- CO_2 activation increased micro and mesopores in PAN fiber mats, which improved the capacitance at low current density. However, the capacitance at high current density decreased dramatically.
- To maintain high capacitance at high current density, a sacrificial component SAN was added into PAN. This resulted in mesopore domination with high capacitance at high current density.
- Carbon nanotubes were added into PAN and PAN/SAN to improve power density. The power density was enhanced by a factor of four with the addition of 1 wt% SWNT. Power density of

PAN/SAN/SWNT composite as high as 7 kW/kg was measured on a carbonized PAN/SAN/SWNT sample.

- Compared to the activated carbon or carbon nanotube bucky papers, carbonized PAN/SAN fiber mats exhibited significant higher capacitance. This was in part attributed to good electrolyte wettability.

3.5 References

1. B. E. Conway, Electrochemical Supercapacitors: Scientific Fundamentals and Technological Applications, Kluwer Academic/Plenum, **1999**, New York.

2. T. Liu, T.V. Sreekumar, S. Kumar, R. H. Hauge, and R. E. Smalley, Carbon, **2003**, 41, 2440.

3. P. A. Webb and C. Orr. Analytical Methods in Fine Particle Technology, Micromeritics Instrument Corp., **1997**, Norcross, GA.

4. S. Brunauer, P. H. Emmett, and E. Teller, Journal of the American Chemical Society, **1938**, 60, 309.

5. H. G. Chae, T.V. Sreekumar1, T. Uchida, and S. Kumar, Polymer, **2005**, 46, 10925.

6. J. Xie, X. Wang, J. Deng, and L. Zhang, Applied Surface Science, **2005**, 250, 152.

7. C. Zhou, T. Liu, T. Wang, and S. Kumar, Polymer, **2006**, 47, 5831.

8. C. Zhou, S. Kumar, C. D. Doyle and J. M. Tour, Chemistry of Materials, **2005,** 17, 1997.

9. F. Caturla, M. M. Sabio, and F. R. Reinoso, Carbon, **1991**, 29, 999.

10. A. Addoun, J. Dentzer, and P. Ehrburger, Carbon, **2002**, 40, 1140.

11. M. M. Sabio, M. T. Gonzalez, F. R. Reinoso, and A. S. Escribano, Carbon, **1996**, 34, 505.

12. M. Endo, Y. J. Kim, T. Takeda, T. Maeda, T. Hayashi, K. Koshiba, H. Hara, and M. S. Dresselhaus, Journal of the Electrochemical Society, **2001**, 148, A1135.

13. A. Alonso, V. Ruiz, C. Blanco, R. Santamaría, M. Granda, R. Menéndez, and S. G. E. de Jager, Carbon, **2006**, 44, 441.

14. D. Qu, Journal of Power Sources, **2002**, 109, 403.

15. B. Fang, Y. Z. Wei, and M. Kumagai, Journal of Power Sources, **2006**, 155, 487.

16. H. Tamai, M. Kunihiro, M. Morita, and H. Yasuda, Journal of Materials Science, **2005**, 40, 3703.

17. J. Ozaki, N. Endo, W. Ohizumi, K. Igarashi, M. Nakahara, A. Oya, S. Yoshida and T. Ilzuka, Carbon, **1997**, 35, 1031.

18. C. Zhou, PhD thesis, Georgia Institute of Technology, December, **2006**.

19. D. Qu and H. Shi, Journal of Power Sources, **1998**, 74, 99.

20. K. Kierzek, E. Frackowiak, G. Lota, G. Gryglewicz, and J. Machnikowski, Electrochimica Acta, **2004**, 49, 515.

21. J. A. Maciá-Agulló, B. C. Moore, D. C. Amoros, and A. L. Solano, Carbon, **2004**, 42, 1367.

22. C. Kim and K. S. Yang, Applied Physics Letters, **2003**, 83, 1216.

23. Ch. Emmenegger, Ph. Mauron, P. Sudan, P. Wenger, V.Hermann, R. Gallay, and A. Züttel, Journal of Power Sources, **2003**, 124, 321.

24. K. H. An, W. S. Kim, Y. S. Park, J. M. Moon, D. J. Bae, S. C. Lim, Y. S. Lee, and Y. H. Lee, Advanced Functional Materials, **2001**, 11, 387.

25. C. Kim, S. H. Park, W. J. Lee, and K. S. Yang, Electrochimica Acta, **2004**, 50, 877.

26. Y. T. Kim and T. Mitani, Journal of Power Sources, **2006**, 158, 1517.

27. Y. Z. Wei, B. Fang, S. Iwasa, and M. Kumagai, Journal of Power Sources, **2005**, 141, 386.

28. B. Fang and L. Binder, Journal of Physical Chemistry B, **2006**, 110, 7877.

29. K. H. An, K. K. Jeon, J. K. Heo, S. C. Lim, D. J. Bae, and Y. H. Lee, Journal of the Electrochemical Society, **2002**, 149, A1058.

30. H. Shi, Electrochemica Acta, **1996**, 41, 1633.

31. J. Gamby, P. L. Taberna, P. Simon, J. F. Fauvarque, and M. Chesneau, Journal of Power Sources, **2001**, 101, 109.

32. T. Osaka, Xing. Liu, M. Nojima, and T. Momma, Journal of the Electrochemical Society, **1999**, 146, 1724.

CHAPTER 4

CONCLUSIONS AND RECOMMENDATIONS

4.1 Conclusions

Morphology and diameter of electrospun polyacrylonitrile fibers have been studied as a function of polymer molecular weight, solution concentration, solution flow rate, distance between the spinneret and the target, and applied voltage. The key conclusions of this study are:

- In the semidilute unentangled regime, the microscopic or nanoscopic particles were obtained. In the semidilute entangled regime, continuous fibers were obtained, whose diameter exhibited two power law scaling relationship with concentration.
- The diameter of the electrospun PAN fibers increased with solution flow rate and decreased when electric field was increased by changing the working distance, however it did not change significantly when the electric field was varied by changing the voltage at a given working distance. Fiber diameter increased with the polymer concentration and ranged from 30 nm to 3.0 μm.
- Conditions for electrospinning small diameter bead free PAN fibers were developed. Nearly bead free fibers with 60 nm diameter were obtained by using $ZnCl_2$ containing PAN/DMF solutions.
- Branching was observed on the fiber jet when electrospinning low concentration PAN solution or PAN/CNT dispersions.

- The PAN crystal size calculated from the ~17° 2θ peak was about 3 nm in all electrospun fibers and was in the range of 5 to 6 nm in all films. This suggests inhibited crystallization during electrospinning.

Electrospun PAN, PAN/SAN, and PAN/SAN/CNT fiber mats were stabilized, carbonized, and processed into electrochemical capacitor electrodes. The capacitance performance was tested by constant current charge/discharge method or by cyclic voltammetry in 6 M KOH aqueous solution. The key conclusions of this study are:

- With the addition of sacrificial component, poly(styrene-co-acrylonitrile)(SAN), mesopore volume increased, resulting in high capacitance at high current density.
- The capacitance of carbonized electrospun PAN/SAN/CNT fiber mats is up to 100 F/g higher than that of the carbonized PAN/SAN/CNT films, and up to 150 F/g higher than that for the carbon nanotube bucky paper.
- With the addition of 1 wt% single wall carbon nanotube (SWNT) into PAN/SAN, power density increased by a factor of four.

4.2 Recommendations for future work

Current work suggests that electrospun PAN/SAN/CNT fiber mats are good candidates for processing electrochemical capacitors. To further optimize capacitance performance, following study is suggested:

- **Hollow carbon nanofibers**: the central canal of the hollow carbon nanofibers can provide more space to store electrolyte ions, thus resulting in improved capacitance performance. To obtain hollow carbon nanofibers, bicomponent electrospinning is suggested to process PAN shell with sacrificial component

(such as SAN) as the core. In the process of carbonization, core composed of the sacrificial component will be burned out and the shell will be converted to carbon, resulting in a hollow carbon nanofiber.

- **Porous PAN nanofibers**: current study showed that porous PAN nanofibers can be obtained using nitromethane/water as solvent. It has also been reported in the literature that porous PAN nanofibers can be obtained by electrospinning PAN/DMF solution into a cryogenic liquid.[1] Therefore by controlling electrospinning factors such as environment (such as temperature, solvent evaporation rate, etc.), solution phase behavior, the porosity in PAN nano fibers can be controlled. This should prove to be useful in further optimizing capacitance performance.
- **Conducting polymer nanofibers**: electrically conducting polymers such as poly(p-phenylene vinylene)(PPV)[2] and poly(aniline)[3, 4] can be electrospun into nanofibers, which have high surface area, porosity, and good electrical conductivity. The conducting polymer nanofibers based electrochemical capacitors are expected to have high capacitance and power density.

4.3 References

1. J. T. McCann, M. Marquez, and Y. Xia, Journal of the American Chemical Society, 2**006**, 128, 1436

2. Y. Xin, Z. H. Huang, E. Y. Yan, W. Zhang, and Q. Zhao, Applied Physics Letters, 2006, **89**, 053101.

3. A. G. Macdirmid, W. E. Jones, I. D. Norris, J. Gao, A. T. Johnson, N. J. Pinto, J. Hone, B. Han, F. K. Ko, H. Okuzaki, and M. Llaguno, Synthetic Metals, **2001**, 119, 27.

4. N. J. Pinto, A. T. Johnson, A. G. MacDiamid, C. H. Mueller, N. Theofylaktos, D. C. Robinson, and F. A. Miranda, Applied Physics Letters, **2003**, 83, 4244.

APPENDIX A

WIDE ANGLE X-RAY DIFFRACTION (WAXD) OF ELECTROSPUN POLY(ACRYLONITRILE) NANOFIBERS

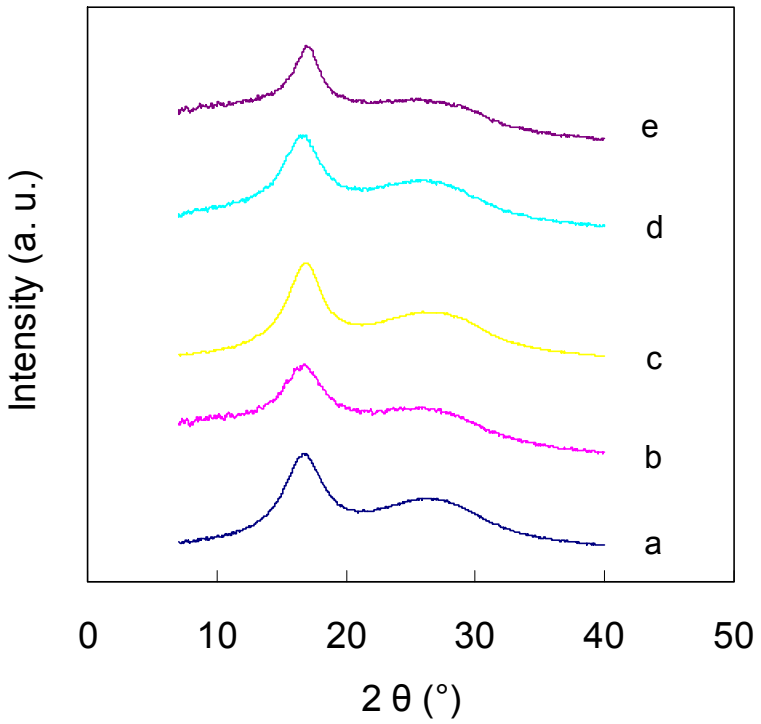

Figure A.1. Plots of integrated intensity as a function of 2θ for electrospun PAN fibers with diameter of (a) 50 nm, (b) 70 nm, (c) 200 nm, (d) 600 nm, and (e) 1.1 μm. (Solution flow rate is 1 ml/h, the distance between the needle tip and the target is 10 cm, and the voltage is 22 kV.)

Table A.1. WAXD results of electrospun PAN fiber mats with different fiber diamters.

Fiber diameter (nm)	2 θ (°)	d spacing (Å)	Crystal size (Å)	Crystallinity (%)
50	16.7	5.3	27	53
70	16.7	5.3	26	45
200	16.9	5.2	29	57
600	16.6	5.3	27	49
1100	17.1	5.2	35	45

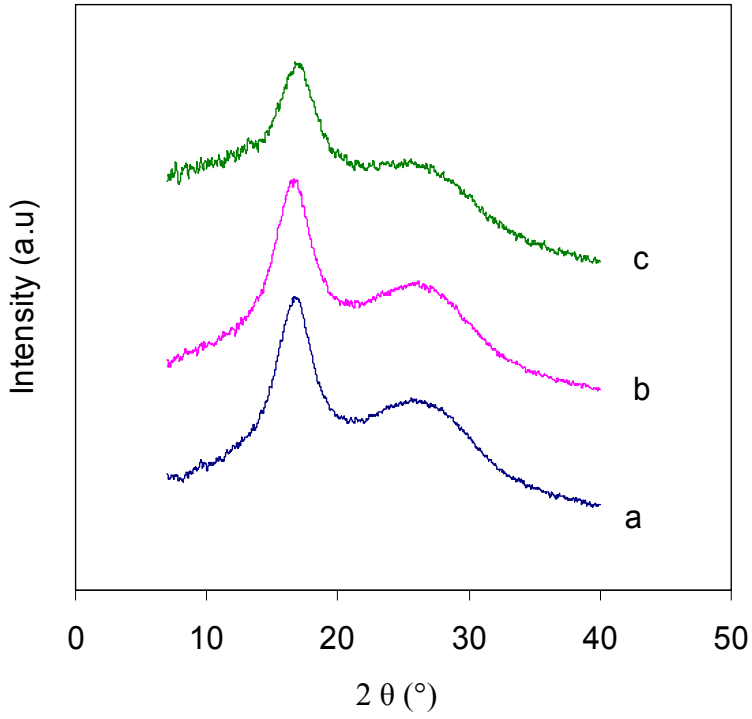

Figure A.2. Plots of integrated intensity as a function of 2θ for PAN fiber mat electrospun at voltage of (a) 13 kV, (b) 22 kV, and (c) 25 kV. (Concentration of PAN/DMF is 19 wt%, the solution flow rate is 1 ml/hr, the distance between the needle tip and the target is 10 cm.)

Table A.2. WAXD results of PAN fiber mats electrospun from different voltages.

Voltage (kV)	**2 θ (°)**	**d spacing (Å)**	**Crystal size (Å)**	**Crystallinity (%)**
13	16.7	5.3	28	43
22	16.6	5.3	27	49
25	17.0	5.2	28	40

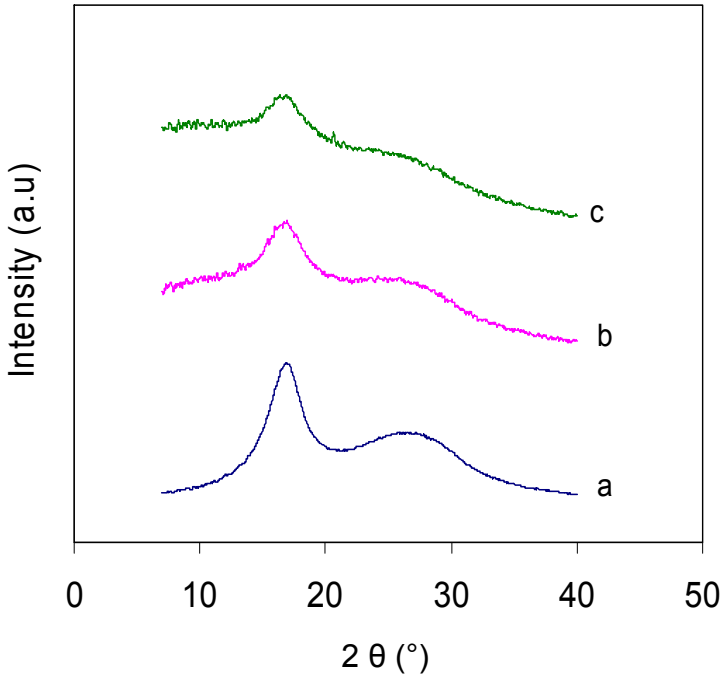

Figure A.3. Plots of integrated intensity as a function of 2θ for PAN fiber mats electrospun from (a) DMF, (b) DMSO, and (c) nitromethane/water (94/6). (6 wt% PAN solution, solution flow rate is 1 ml/h, the distance between the needle tip and the target is 10 cm, and the voltage is 22 kV.)

Table A.3. WAXD results of PAN fiber mats electrospun from different solvents.

Solvent	2 θ (°)	d spacing (Å)	Crystal size (Å)	Crystallinity (%)
DMF	16.7	5.3	27	53
DMSO	16.7	5.3	27	51
Nitromethane/water (94/6)	17.1	5.2	30	56

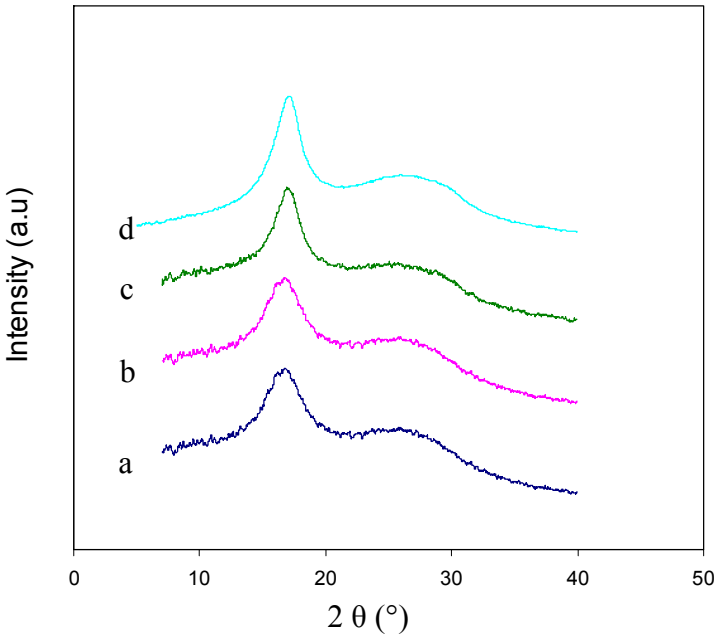

Figure A.4. Plots of integrated intensity as a function of 2θ for (a) electrospun PAN fibers with 70 nm diameter, (b) PAN fibers of 70 nm diameter annealed at 150 ºC for 60 minutes, (c) electrospun PAN fibers of 1.1 μm diameter, and (d) PAN fibers of 1.1 μm diameter annealed at 150 ºC for 60 minutes.

Table A.4. WAXD results of orgininal and annealed PAN fiber mats.

Sample	**2 θ (°)**	**d spacing (Å)**	**Crystal size (Å)**	**Crystallinity (%)**
Electrospun PAN fibers with 70 nm diameter	16.7	5.3	26	45
Annealed PAN fibers with 70 nm diameter	16.7	5.3	26	44
Electrospun PAN fibers with 1.1 μm diameter	17.1	5.2	35	45
Annealed PAN fibers with 1.1 μm diameter	16.8	5.2	34	46

APPENDIX B

ISOTHERMAL NITROGEN ADSORPTION AND DESORPTION PLOTS

The isothermal adsorption and desorption plots reveal the characteristics of porous materials. According to IUPAC definition, six types of isothermal plots are classified as shown in Figure B.1.[1] In Type I, micropores are present. Type II is the characteristic of macroporous or nonporous materials. Type III or V appears when adsorptive gas molecules have more affinity with each other than with materials. In Type IV, the hystersis loop is associated with capillary condensation taking place in mesoporous materials. Type VI represents stepwise multilayer adsorption on a uniform non-porous surface. Isothermal adsorption/desorption plots of various samples studied in this thesis are documented in Figures B.2 to B.7.

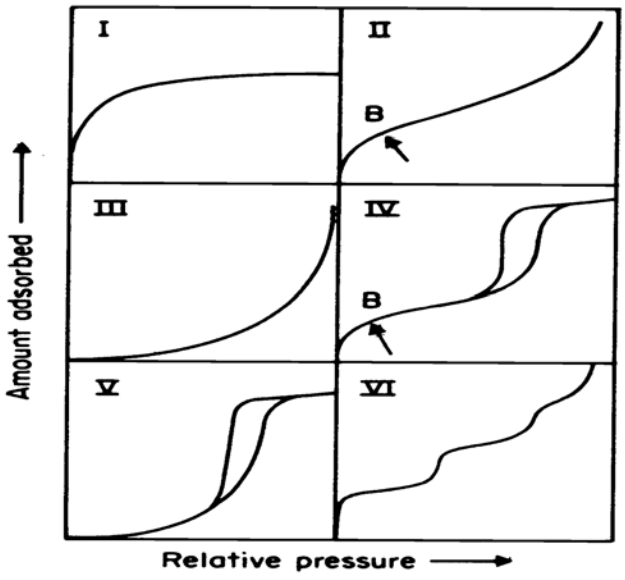

Figure B.1. Typical isothermal nitrogen adsorption/desorption plots observed in porous materials. (From ref. 1.)

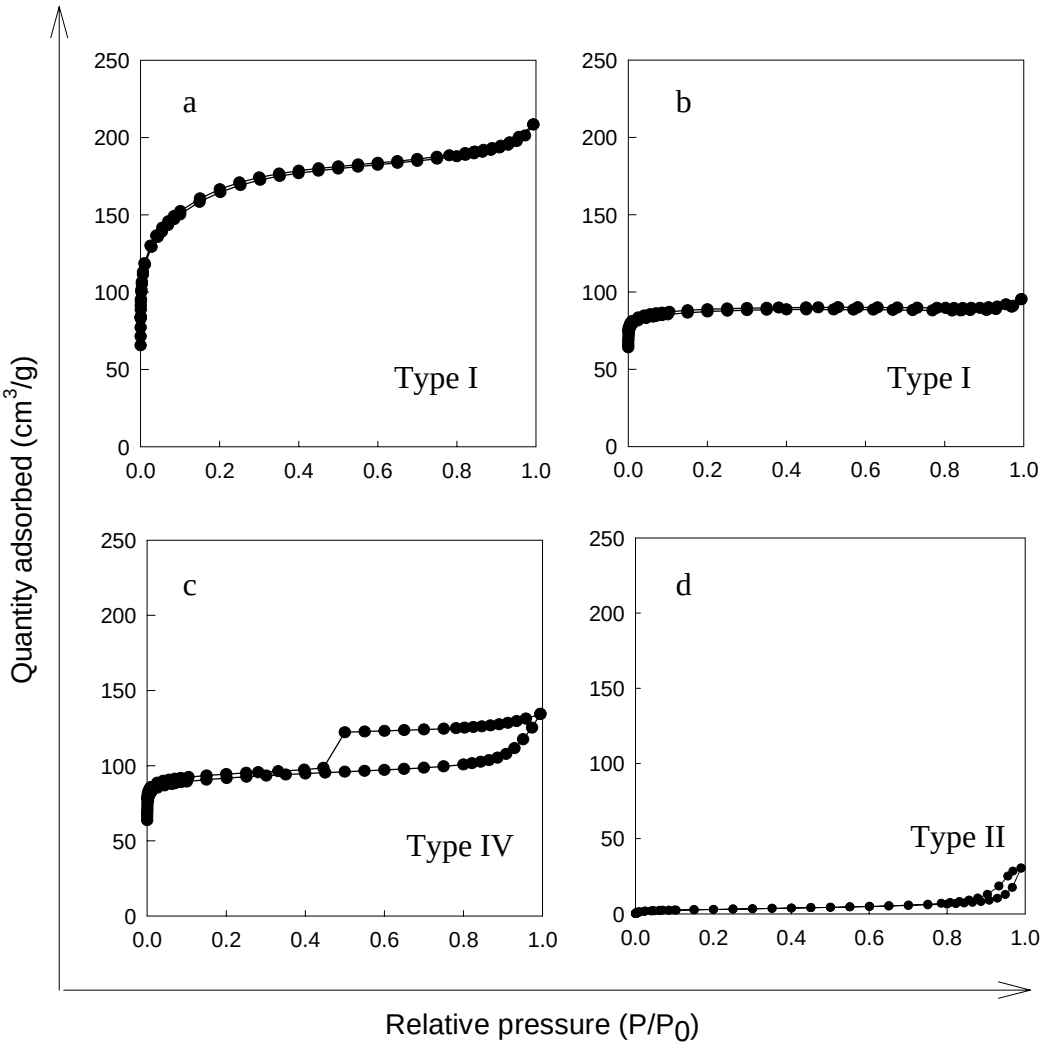

Figure B.2. Isothermal plots of carbonized PAN fibers with diameter of (a) 100 nm, (b) 200 nm, and (c) 400 nm, and (d) isothermal plot of 200 nm diameter pristine fiber mat without stabilization and carbonization.

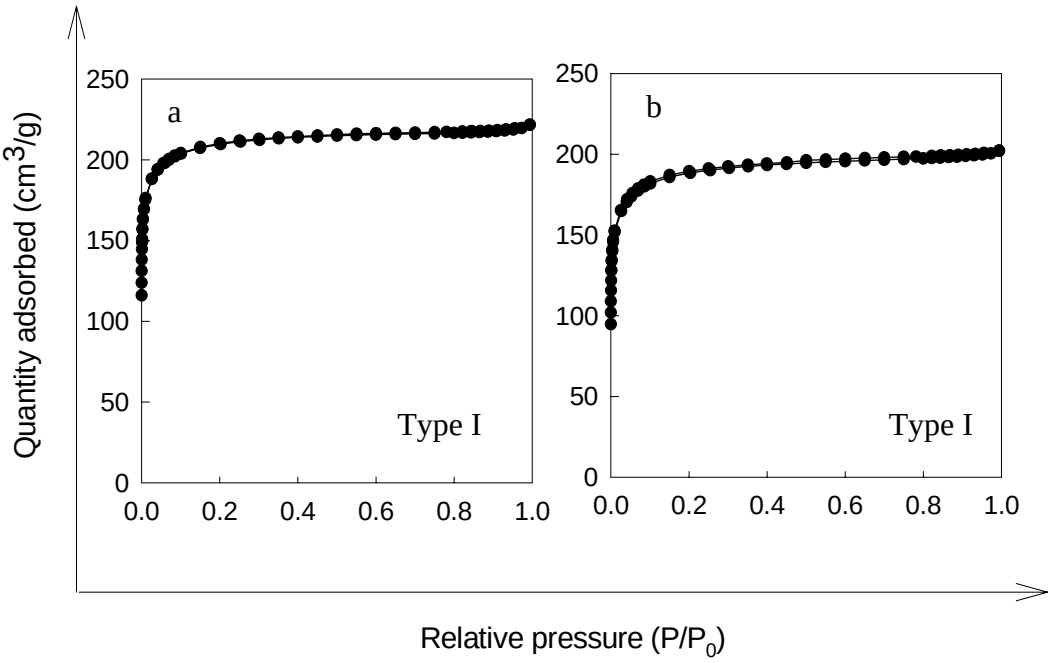

Figure B.3. Isothermal plots of (a) 60 nm PAN/$ZnCl_2$ fibers and (b) 600 nm porous PAN fibers.

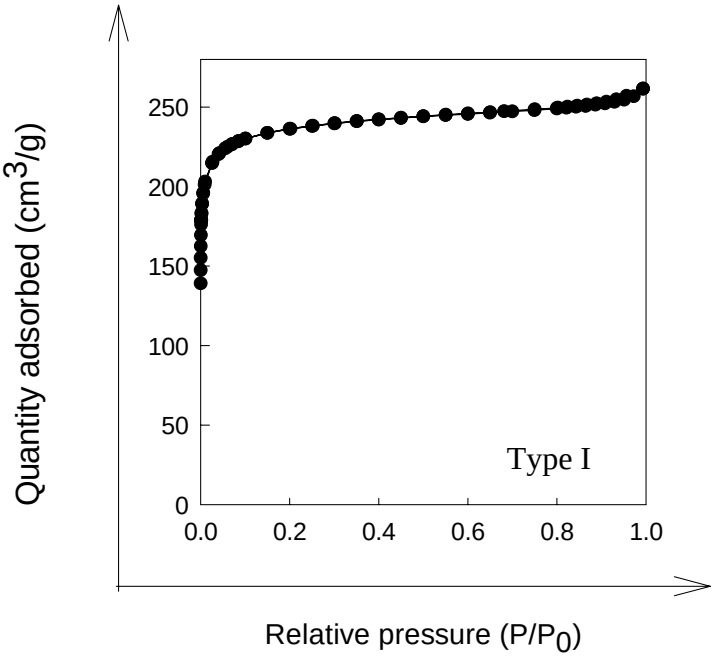

Figure B.4. Isothermal plot of activated PAN fiber mat.

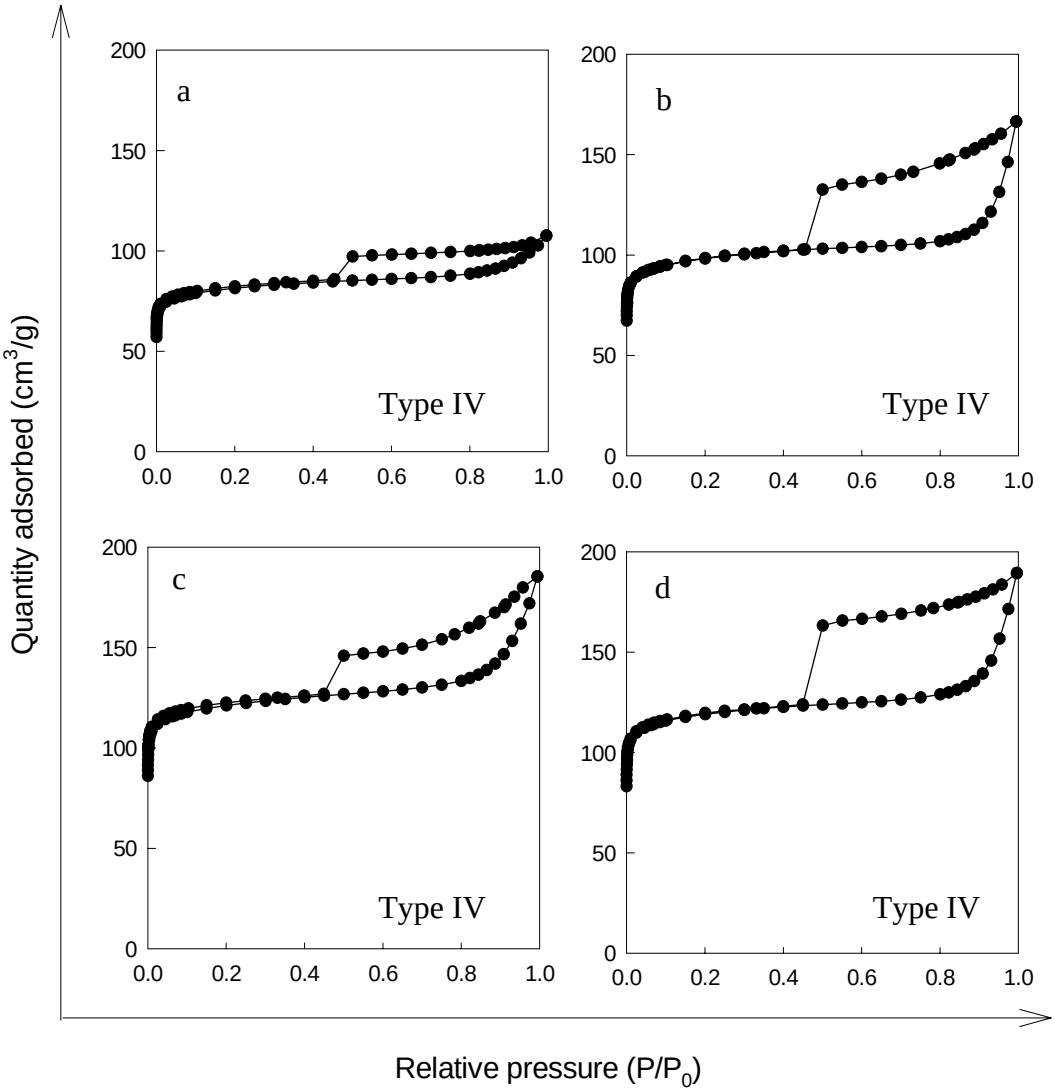

Figure B.5. Isothermal plots of (a) carbonized PAN/SAN (90/10), (b) carbonized PAN/SAN (80/20), (c) carbonized PAN/SAN (70/30), and (d) carbonized PAN/SAN (50/50).

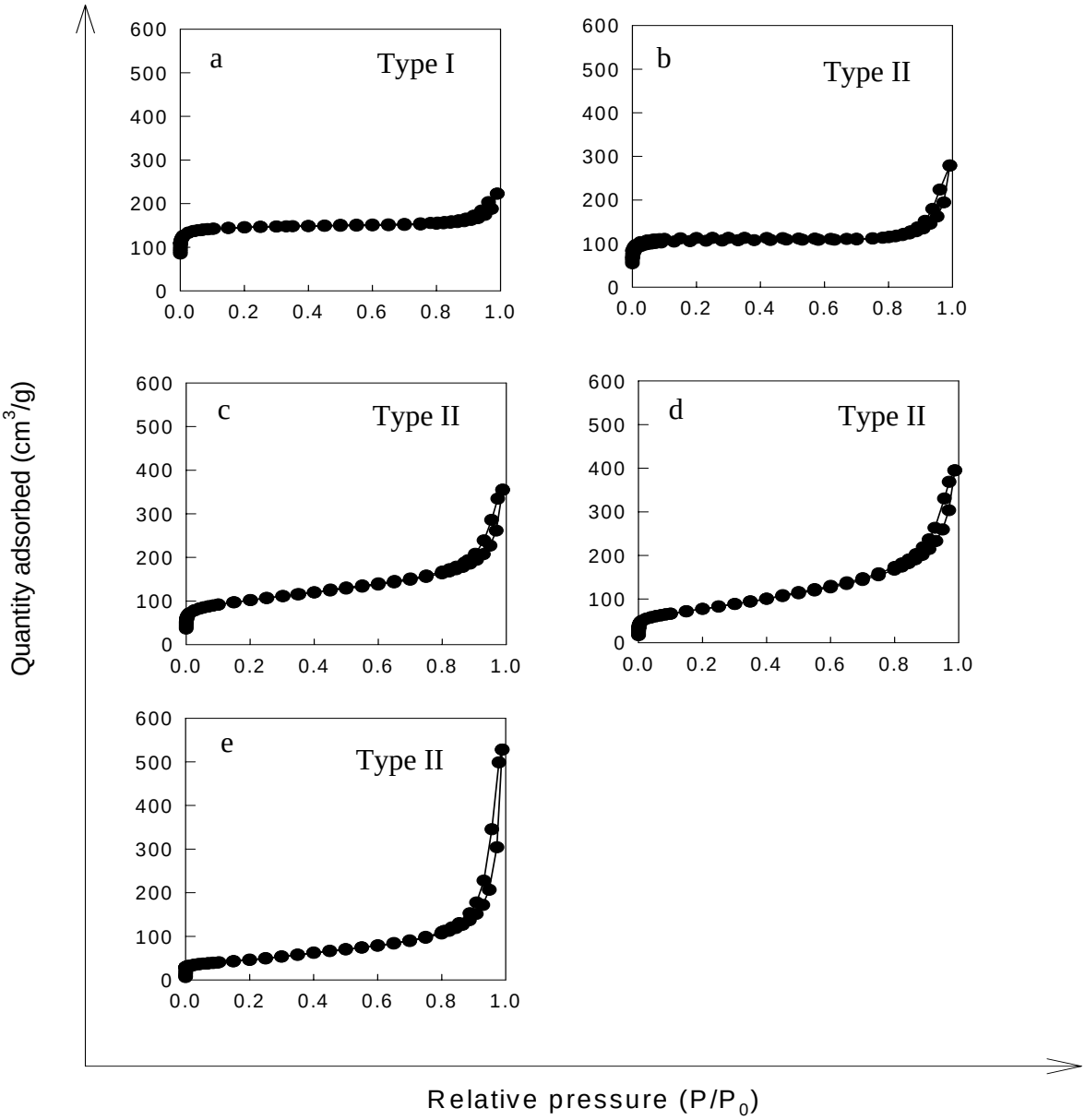

Figure B.6. Isothermal plots of (a) carbonized PAN/MWNT (95/5) fiber mat, (b) carbonized PAN/MWNT (90/10) fiber mat, (c) carbonized PAN/MWNT (80/20) fiber mat, (d) carbonized PAN/MWNT (70/30) fiber mat, and (e) MWNT powder.

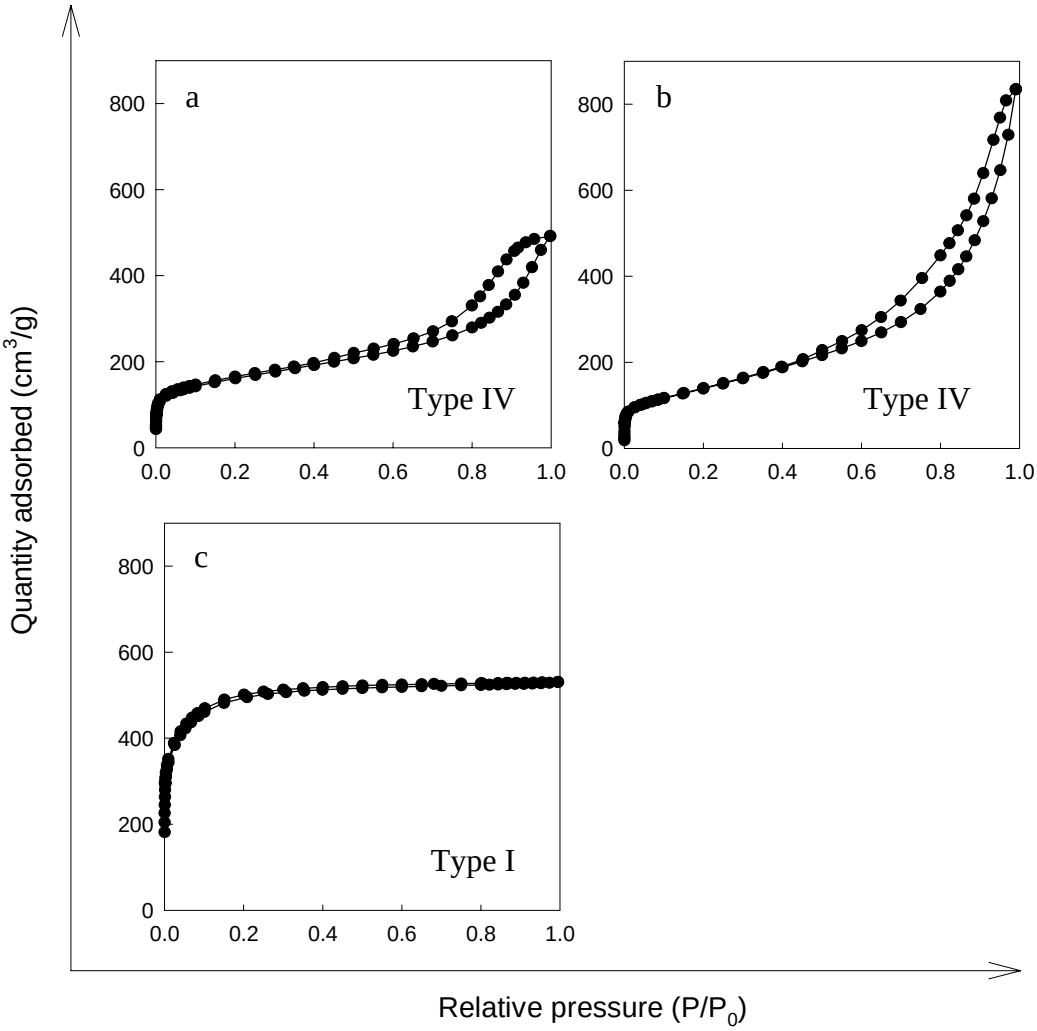

Figure B.7. Isothermal plots of (a) SWNT bucky paper, (b) DWNT bucky paper, and (c) activated carbon.

References

1. K. S. W. Sing, D. H. Everett, R. A. W. Haul, L. Moscou, R. A. Pierotti, J. Rouquérol, and T. Siemieniewska, Pure and Applied Chemistry, **1985**, 57, 603.

APPENDIX C

CONSTANT CURRENT CHARGE/DISCHARGE VOLTAGE-TIME PLOTS

The constant current charge/discharge method is commonly used for evaluating electrochemical capacitor performance. In this method, the current is kept constant, while the voltage is recorded as a function of time. When an electrochemical capacitor is charged, the voltage increases with time; when an electrochemical capacitor is discharged, the voltage decreases. Based on the voltage-time plots, the specific capacitance, power density, and

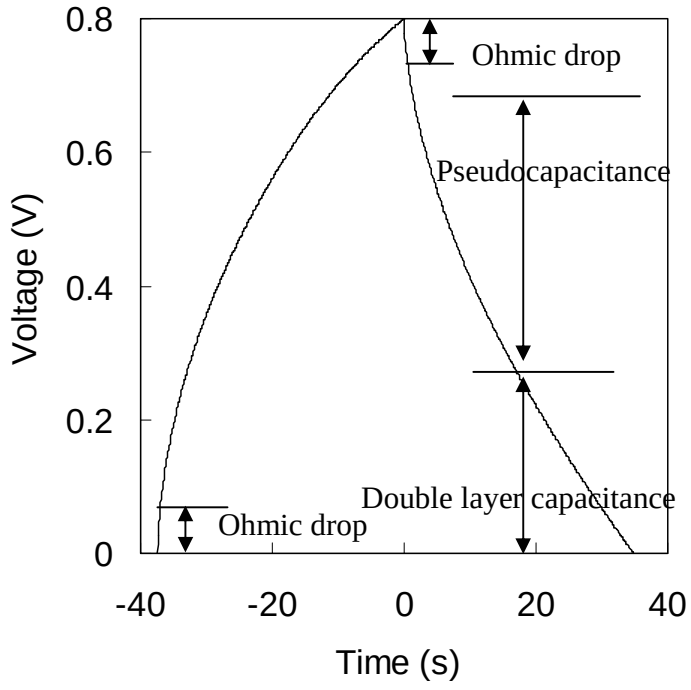

Figure C.1. A typical constant current charge/discharge plot of an electrochemical capacitor. (From ref. 3).

energy density can be evaluated.[1] For an ideal double layer capacitor, the voltage should exhibit a linear relationship with time; however, the plot would deviate from the straight line if pseudocapacitance is present or show an ohmic drop if the internal resistance is present.[2] The voltage-time plot in Figure C.1 shows three regions: an ohmic drop (a sudden drop of voltage), a double layer capacitor region where voltage linearly depends on time, and a pseudocapacitance region where voltage-time curve deviates from the straight line.[3] Voltage-time plots of various samples studied in this thesis are documented in Figures C.2 to C.8.

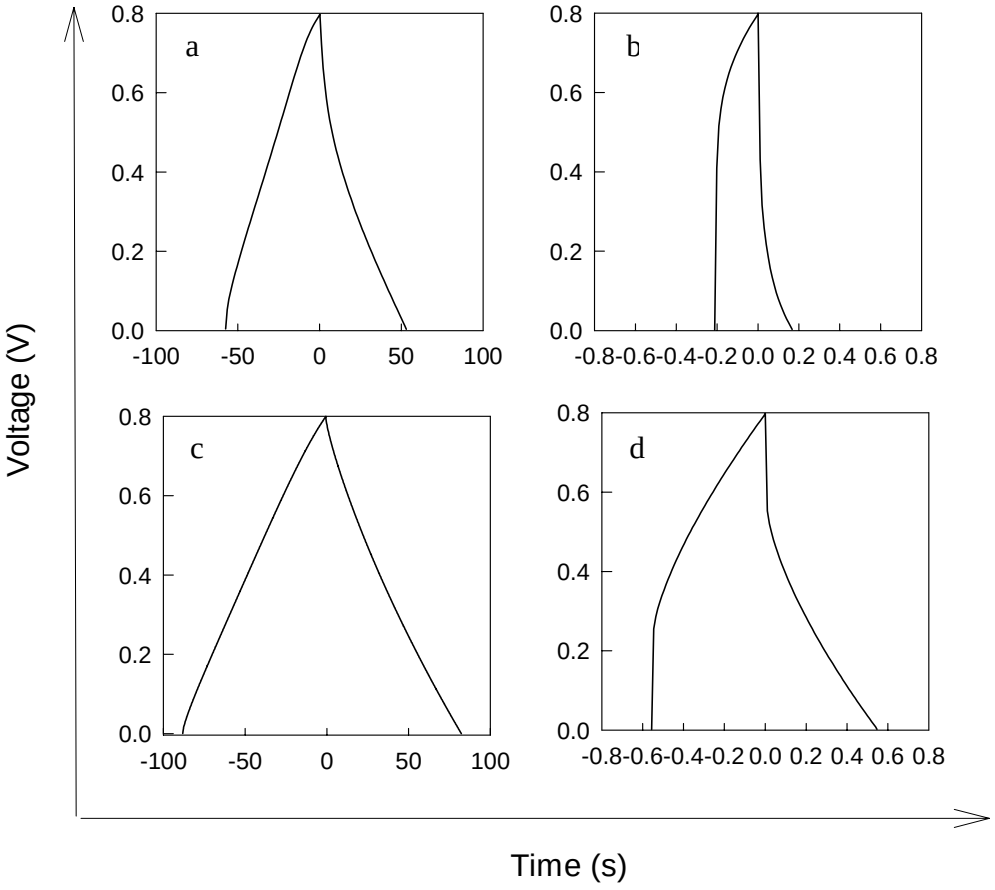

Figure C.2. Voltage-time plots of carbonized PAN fiber mats at two current densities for (a) 100 nm PAN fiber(0.6 A/g), (b) 100 nm PAN fiber(11.4 A/g), (c) 200 nm PAN fiber(1.2 A/g), (d) 200 nm PAN fiber(62.2 A/g), (e) 400 nm PAN fiber(1.7 A/g), and (f) 400 nm PAN fiber(69.8 A/g). (The numbers in the brackets indicate the current density.)

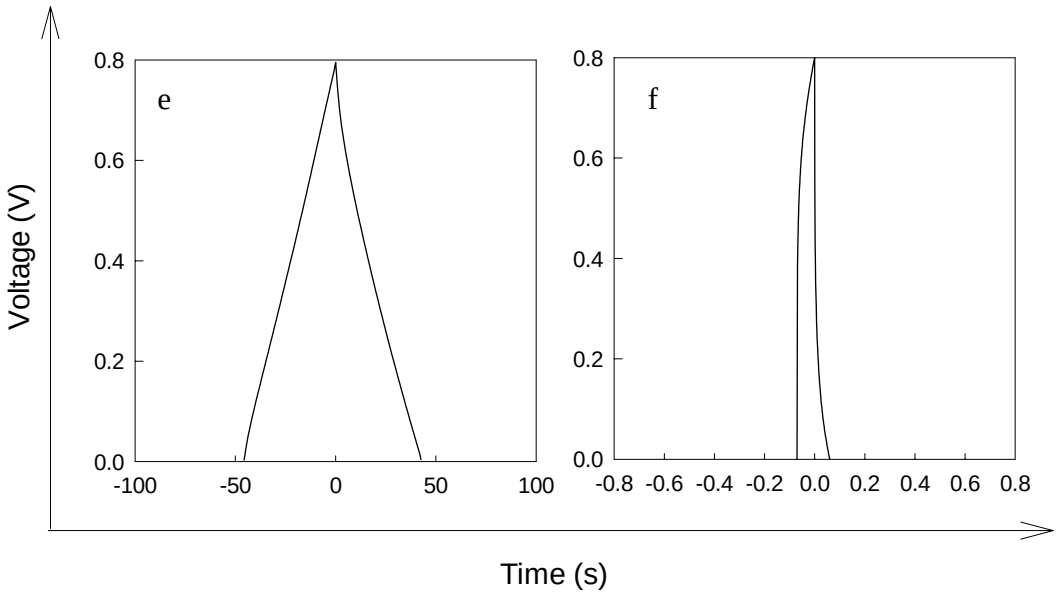

Figure C.2. Continued.

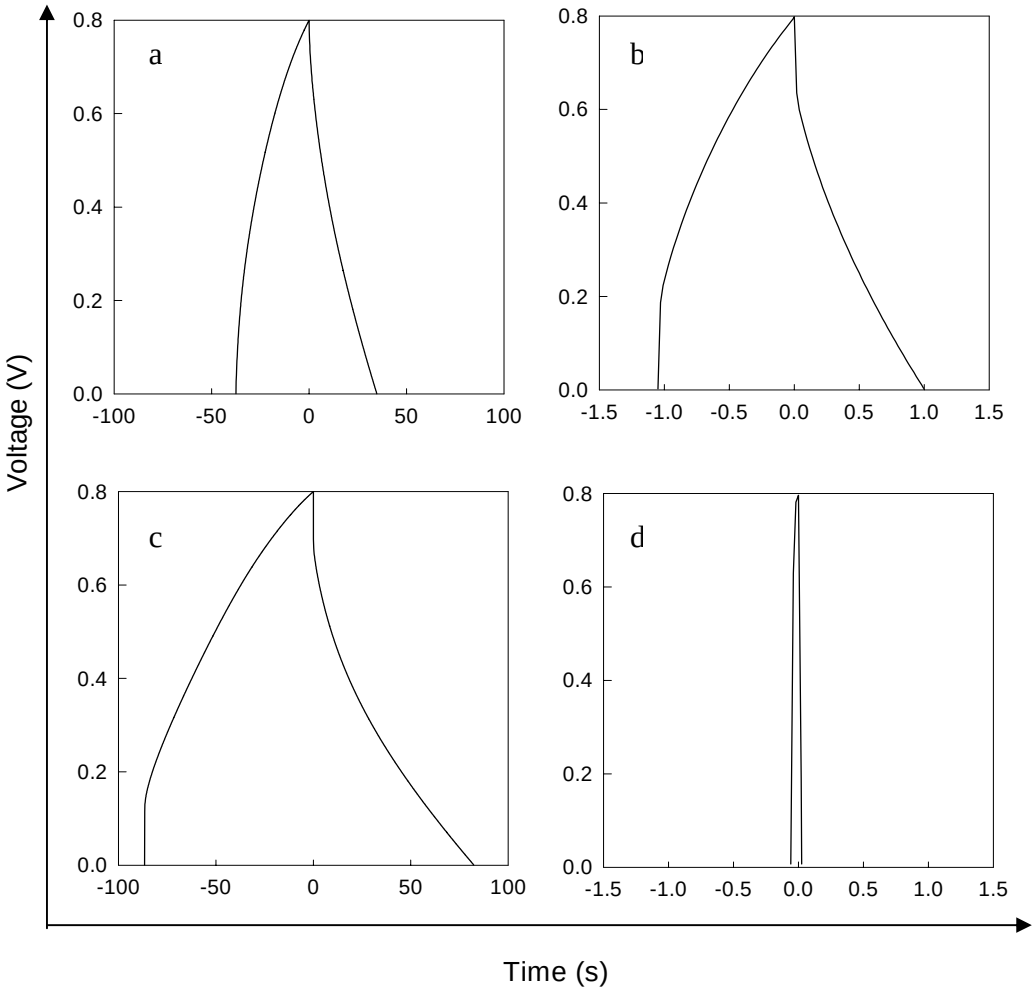

Figure C.3. Voltage-time plots at two current densities for (a) 60 nm solid PAN/$ZnCl_2$ nanofibers (1.9 A/g), (b) 60 nm solid PAN/$ZnCl_2$ nanofibers (19.4 A/g), (c) 600 nm porous PAN nanofibers (1.1 A/g), and (d) 600 nm porous PAN nanofibers (11.3 A/g).

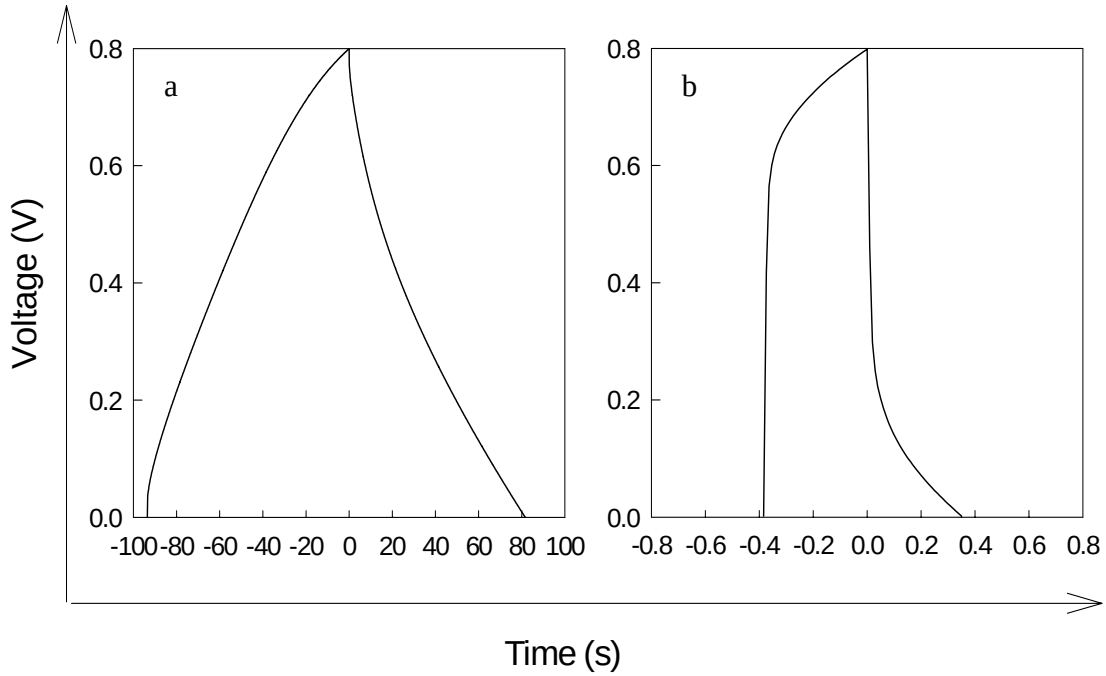

Figure C.4. Voltage-time plots of activated PAN fiber mat at two current densities of (a) 1.2 A/g and (d) 24.3 A/g.

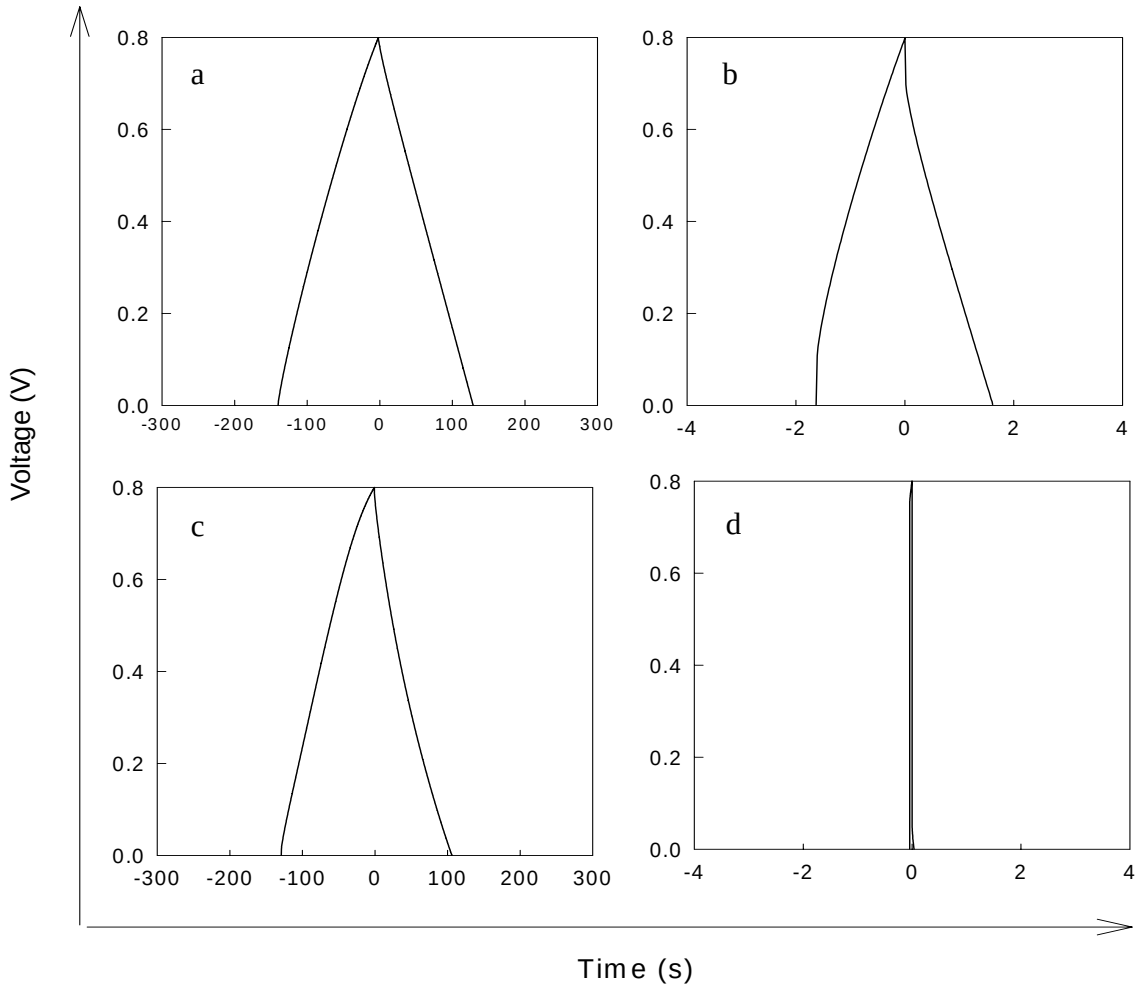

Figure C.5. Voltage-time plots at two current densities for (a) carbonized PAN/SAN(90/10)(1.0 A/g), (b) carbonized PAN/SAN(90/10)(50.2 A/g), (c) carbonized PAN/SAN (80/20)(0.9 A/g), (d) carbonized PAN/SAN(80/20)(49.2 A/g), (e) carbonized PAN/SAN (70/30)(0.5 A/g), (f) carbonized PAN/SAN (70/30)(26.9 A/g), (g) carbonized PAN/SAN (50/50)(2.3 A/g), and (h) carbonized PAN/SAN (50/50)(113.0 A/g) fiber mats.

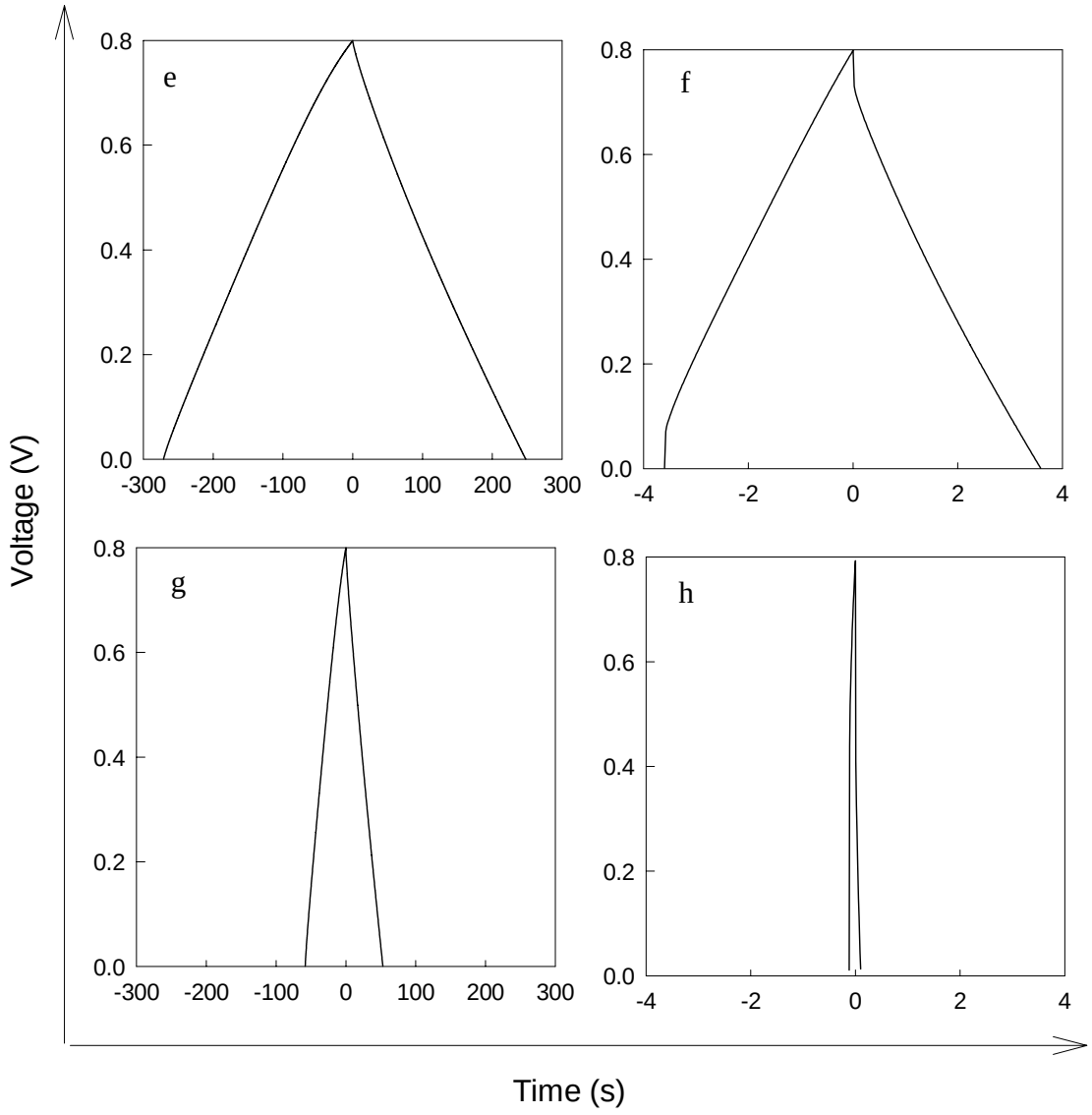

Figure C.5. Continued.

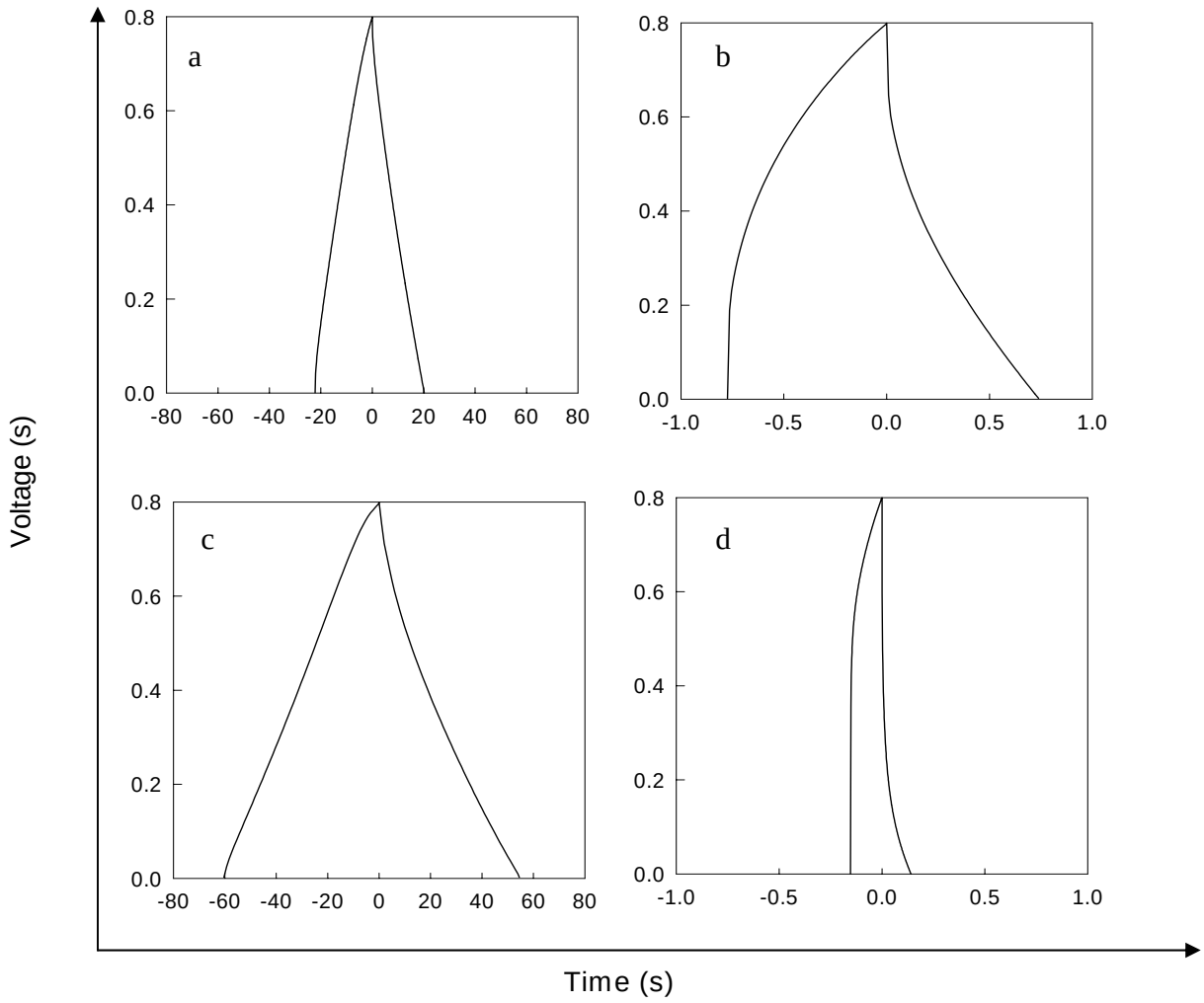

Figure C.6. Voltage-time plots at two current densities for (a) carbonized PAN/SAN/SWNT (80/20/1 wt%) (5.1 A/g), (b) carbonized PAN/SAN/SWNT (80/20/1 wt%) (50.6 A/g), (c) carbonized PAN/SAN/SWNT (80/20/3 wt%) fiber mat(2.3 A/g), and (d) carbonized PAN/SAN/SWNT(80/20/3 wt%) fiber mat(90.9 A/g).

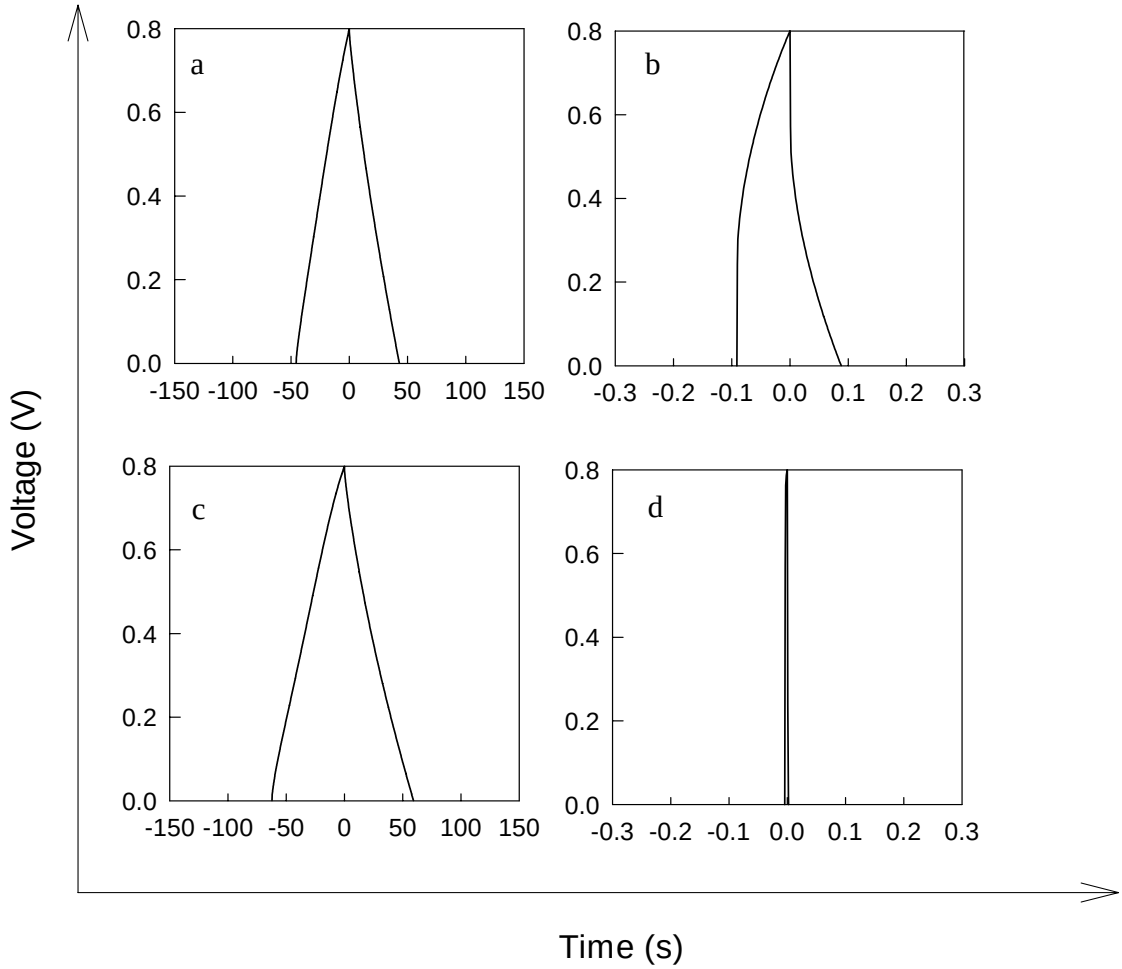

Figure C.7. Voltage-time plots at two current densities for (a) carbonized PAN/MWNT (95/5) (2.2 A/g), (b) carbonized PAN/MWNT (95/5) fiber mat(223.2 A/g), (c) carbonized PAN/MWNT(90/10) (1.2 A/g), (d) carbonized PAN/MWNT(90/10) (116.1 A/g), (e) carbonized PAN/MWNT(80/20) (0.5 A/g), (f) carbonized PAN/MWNT(80/20)(50.2 A/g), (g) carbonized PAN/MWNT (70/30)(1.2 A/g), and (h) carbonized PAN/MWNT (70/30)(118.1 A/g) fiber mats.

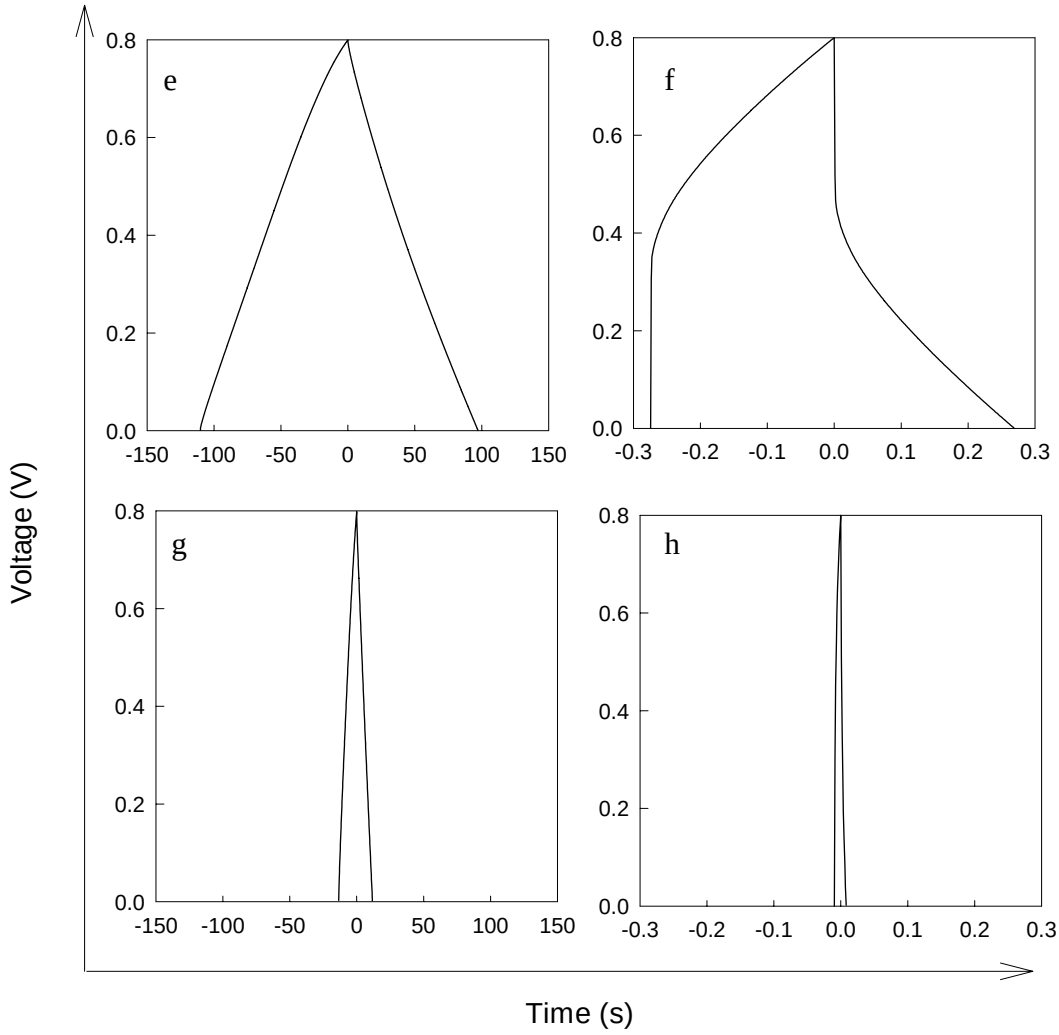

Figure C.7. Continued.

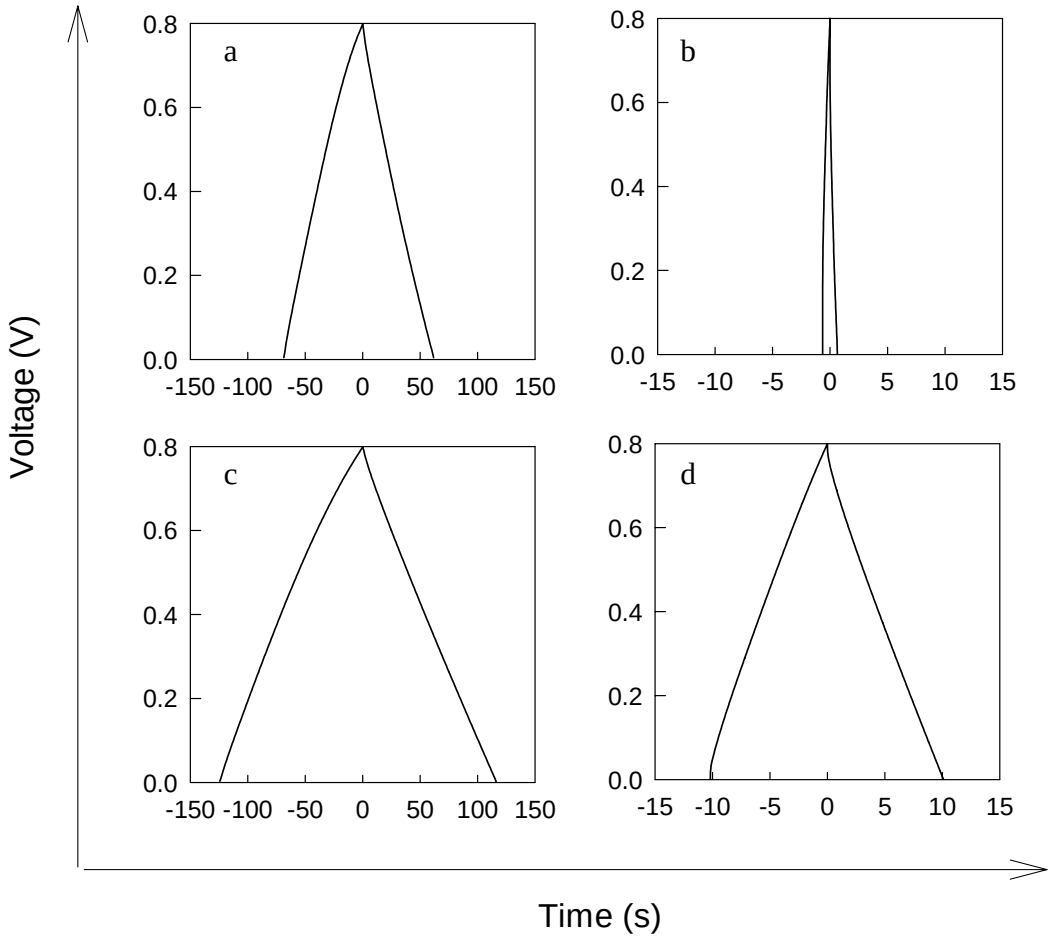

Figure C.8. Voltage-time plots at two current densities for (a) SWNT bucky paper (0.5 A/g), (b) SWNT bucky paper(20.9 A/g), (c) DWNT bucky paper(0.2 A/g), (d) DWNT bucky paper(2.2 A/g), (e) activated carbon(0.2 A/g), and (f) activated carbon(1.5 A/g).

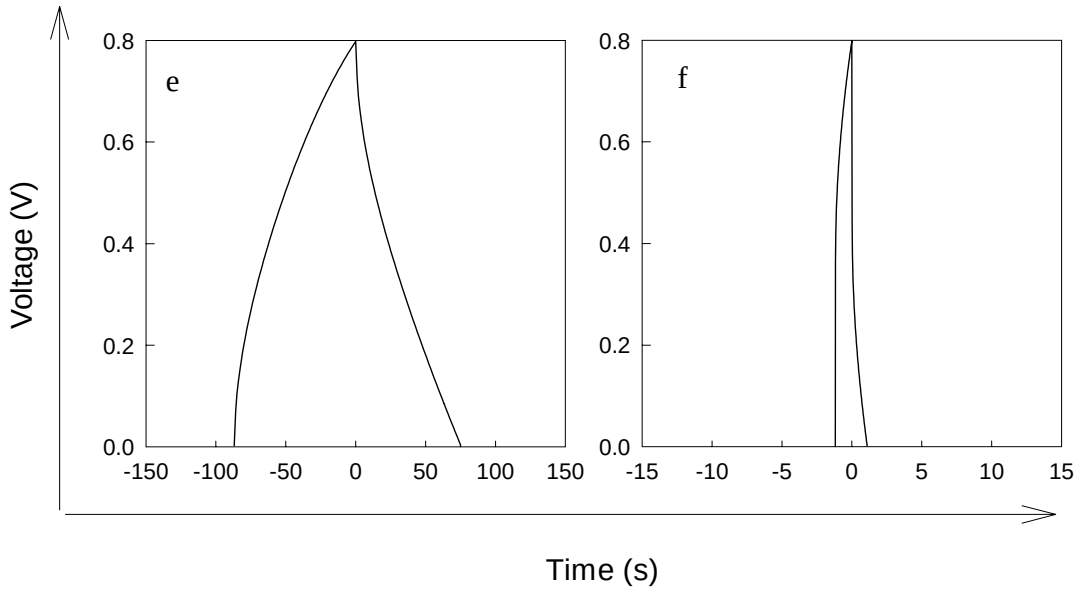

Figure C.8. Continued

References

1. B. E. Conway, Electrochemical Supercapacitors: Scientific Fundamentals and Technological Applications, Kluwer Academic/Plenum, **1999**, New York.

2. G. Lota, B. Grzyb, H. Machnikowska, J. Machnikowski, and E. Frackowiak, Chemical Physics Letters, **2005**, 404, 53.

3. M. S. Michael and S. R. S. Prabaharan, Journal of Power Sources, **2004**, 136, 250.